

https://dspace.org/

The Eigenmodes of Complex Media

Peters, Cade Ribeiro

2024
University of the Witwatersrand, Johannesburg
https://hdl.handle.net/10539/42113
Peters, Cade Ribeiro . (2024). The Eigenmodes of Complex Media [Master's dissertation, University of the Witwatersrand, Johannesburg]. WireDSpace.

Downloaded from a DSpace repository. https://dspace.org/

UNIVERSITY OF THE WITWATERSRAND

MASTERS DISSERTATION

The Eigenmodes of Complex Media

Author:
Cade Ribeiro Peters

Supervisors:
Prof. Andrew Forbes



WITS
UNIVERSITY

A thesis submitted in fulfillment of the requirements for the degree of Master of Science

in the

Structured Light Laboratory
School of Physics

April 10, 2024

Declaration of Authorship

I, Cade Ribeiro Peters, declare that this thesis titled, "The Eigenmodes of Complex Media" and the work presented in it are my own. I confirm that:

- This work was done wholly or mainly while in candidature for a research degree at this University.
- Where any part of this thesis has previously been submitted for a degree or any other qualification at this University or any other institution, this has been clearly stated.
- Where I have consulted the published work of others, this is always clearly attributed.
- Where I have quoted from the work of others, the source is always given. With the exception of such quotations, this thesis is entirely my own work.
- I have acknowledged all main sources of help.
- Where the thesis is based on work done by myself jointly with others, I have made clear exactly what was done by others and what I have contributed myself.

Signed:

Date:

"We began as wanderers, and we are wanderers still. "

- Carl Sagan

UNIVERSITY OF THE WITWATERSRAND

Abstract

Master of Science

The Eigenmodes of Complex Media

by Cade Ribeiro Peters

Structured light refers to the tailoring of light in all of its degrees of freedom. This includes amplitude, phase, wavelength and polarisation. Structuring light allows us to create complex optical fields with many interesting and useful properties. These fields have allowed us to ask deeper and more fundamental questions about Physics and have revealed new avenues for investigating aspects of the world around us. They have allowed us to significantly increase the speed at which we communicate and make information more accessible. Additionally, they allow for increased resolution and precision in imaging and measurements, both classical and quantum.

One of the primary limitations when using structured light are the effects of perturbations. Many complex media, such as the atmosphere, underwater or biological specimens have a non-uniform refractive index (varying dielectric constant). This distorts most structured light beams, limiting its performance and possible uses. This works seeks to investigate this problem and offer a solution. Much attention has been given to finding which forms of structured light perform best in certain systems or scenarios.

This work focuses on offering a potential solution to this problem. We begin with a discussion on common forms of structured light and models of light propagation. We then move onto methods for generating structured light experimentally. We then propose the concept of an eigenmode: modes that are perfectly invariant through such systems. They are structured light fields that are specially tailored, using our knowledge and understanding of the Physics of the system, to ensure that they propagate through the system and exit unchanged. We achieve this by modelling our system as a linear operator and then using this to find the eigenstates of this operator. We do this for two highly topical aberrations, providing approaches that can be generalised to almost any optical system. We end off this work with a discussion on important considerations when using eigenmodes for real world applications.

Acknowledgements

I would to thank my supervisor, Prof. Andrew Forbes, for taking me on as his student and giving me the opportunity to pursue this degree. His guidance, knowledge and enthusiasm have been invaluable not only to this project and but to my growth as a scientist and as a person. I am grateful for the opportunity to learn from him and the amazing team he has built at the Structured Light Lab. It has been the opportunity of a lifetime.

I would also like to thank my mentors: Dr. Isaac Nape, Dr. Wagner Tavares Buono, Dr. Chané Moodley, Dr. Bereneice Sephton and Dr. Keshaan Singh. The many hours they have each spent with me in and out of the lab have taught me more than I would have ever thought possible. I hope to carry on learning from them and live up to the example they have set.

Thank you to my friends, Pedro Ornelas and Leerin Perumal. We started our journey in Physics together back in 2018. It has been a long and hard road with many bumps and challenges but also many victories and celebrations. It has been a privilege to learn from you and work alongside you these past 6 years. I don't think I would be here today without your friendship.

Finally, I would like to thank my parents. Without their hard work and many sacrifices, I would not have been able to study what I love. Without their love, care, wisdom and example, I would not be the scientist or the person I am today. I can never repay all they have done for me but I will work every day to make them proud.

Contents

Declaration of Authorship iii

Abstract vii

Acknowledgements ix

1 Structured Light and Eigenmodes of Free Space 1
1.1 Structured Waves . . . 1
1.1.1 The Electromagnetic Wave Equation . . . 1
1.1.2 The Helmholtz Equation and Bessel-Gaussian Modes . 2
1.1.3 Solutions to the Paraxial Helmholtz Equation . . . 3
Hermite-Gaussian Modes . . . 4
Laguerre-Gaussian Modes . . . 5
1.2 Propagation of Light through Free Space . . . 7
1.2.1 Green's Functions . . . 8
1.2.2 Free Space Green's Function . . . 8
Green's Functions and the Helmholtz Equation . . . 8
Complex Integrals and Feynman's Trick . . . 10
1.2.3 Scalar Diffraction Theory . . . 13
Green's Theorem . . . 13
Helmholtz-Kirchhoff Integral Theorem . . . 14
Sommerfield Radiation Condition . . . 16
Huygens-Fresnel Diffraction . . . 17
1.2.4 Paraxial Light Propagation . . . 19
Fresnel Approximation . . . 20
Fraunhofer Approximation . . . 21
1.2.5 Angular Spectrum Propagation . . . 22

2 Experimental Techniques 27
2.1 Liquid Crystal in Silicon Structured Light Modulators . . . 27
2.1.1 Liquid crystals and Refractive Index . . . 27
2.1.2 Complex amplitude modulation with a Phase-Only Hologram . . . 28
2.2 Digital Micro-Mirror Devices . . . 31
2.2.1 Complex Amplitude with a Binary Hologram . . . 34

3 Eigenmodes of the Tilted Lens 37
3.1 Theory . . . 38
3.1.1 The Tilted Lens . . . 38
3.1.2 Conversion Plane . . . 40

Location of the Conversion Plane . . . 40
Transmission function . . . 42
Experimental Comparison . . . 45
3.1.3 Sorting Modes by their Eigenvalues . . . 47
3.1.4 Generalisation of Eigenvectors . . . 49
3.2 Experimental Setup . . . 50
3.2.1 Propagation . . . 51
3.3 Results . . . 54
3.4 Discussion and Conclusion . . . 58

4 Modelling Atmospheric Turbulence **61**
4.1 Kolmogorov Theory of Turbulence . . . 61
4.2 Statistics for Random Processes . . . 64
4.3 Quantifying Atmospheric Turbulence . . . 65
4.3.1 Refractive Index Fluctuations . . . 65
4.3.2 Turbulence Parameters . . . 67
4.4 Modelling the Phase Distortions . . . 69
4.5 Turbulence Phase Screens . . . 72
4.5.1 Fourier Transform Method . . . 73
Subharmonic Sampling . . . 74
4.5.2 Split Step Method . . . 75
4.5.3 Calibration of Experimental Phase Screens . . . 78

5 Eigenmodes of Atmospheric Turbulence **81**
5.1 Introduction . . . 81
5.2 The Eigenmodes of Turbulence . . . 83
5.2.1 Instantaneous eigenmodes . . . 83
5.2.2 Time Averaged Eigenmodes . . . 86
5.3 Numerical Simulation: Multiple Phase Screen Example . . . 87
5.3.1 Numerical Results . . . 88
5.4 Experimental Results . . . 91
5.4.1 Fresnel Scaling . . . 95
5.5 Discussion . . . 96
5.6 Conclusion . . . 97

6 Numerical Orthogonality Considerations **99**
6.1 Phase Aberrations in the OAM Basis . . . 101
6.2 Propagation in the OAM Basis . . . 103
6.3 Eigenmodes of Turbulence in the OAM Basis . . . 107
6.4 Conclusion . . . 108

List of Figures

1.1 Bessel-Gaussian Beams. 4
1.2 Hermite-Gaussian Beams 6
1.3 Laguerre-Gaussian Beams. 7
1.4 Complex Contour Integrals. 11
1.5 Feynman's Trick. 12
1.6 Surfaces for Green's Theorem. 14
1.7 Diffraction through an Aperture. 16
1.8 Geometry of the New Green's Function. 18
1.9 Geometry for the Diffraction of Paraxial Waves. 20
1.10 Angular Spectrum Propagation. 25

2.1 Liquid Crystal Phase Modulation 29
2.2 Addition of a Phase Grating on the SLM Hologram 32
2.3 Experimental Hermite-Gaussian Beams with an SLM 32
2.4 Experimental Laguerre-Gaussian Beams with an SLM 33
2.5 DMD Micromirrors 33
2.6 Experimental LG and HG Beams with a DMD 35

3.1 Astigmatic Mode Conversion 41
3.2 Location of the Conversion Plane. 44
3.3 Minimum Conversion Angle 45
3.4 Conversion Points 46
3.5 Eigenvalue Mapping 47
3.6 Equivalence Classes 48
3.7 Experimental Setup 51
3.8 Eigenmodes in Propagation 52
3.9 Robust Eigenmodes of the Tilted Lens 55
3.10 Structured Beams under Varying Astigmatism 57

4.1 Turbulent Energy Cascade 61
4.2 Subharmonic Sampling 74
4.3 Strehl Ratio Test 76
4.4 Least Squares Fitting 79
4.5 Phase Screen Calibration 80

5.1 Propagation through Turbulence 82
5.2 The Unit Cell 84
5.3 Eigenmodes of Turbulence 85
5.4 Invariance of Eigenmodes under Numerical Propagation through Turbulence 89

5.5 Crosstalk-Free Transmission 90
5.6 Eigenmodes of Turbulence through an Unperturbed, Uniform Medium 91
5.7 Eigenmodes of a Slant Path 92
5.8 Experimental Setup 93
5.9 Experimental Eigenmodes 94

6.1 Orthogonality of Pixel Basis Eigenmodes 100
6.2 Phase Aberration Operator 104
6.3 Eigenmodes of the Phase Aberration Operator 105
6.4 Propagation Operator 106
6.5 Eigenmodes of Propagation 107
6.6 Turbulence Operator 108
6.7 Turbulence Eigenmodes 109
6.8 Crosstalk of the OAM basis operator 109

List of Tables

3.1 Equivalence Class Superpositions 50

List of Publications

List of Peer-Reviewed Journal Articles

1. W.T. Buono, **C.R. Peters**, J. Tau, I. Nape and A. Forbes, 2022. Eigenmodes of aberrated systems: the tilted lens. *Journal of Optics*, Volume 24, Number 12, 125602.

2. A. Klug, **C.R. Peters** and A. Forbes, 2023. Robust structured light in atmospheric turbulence. *Advanced Photonics*, Volume 5, Issue 1, 016006.

3. **C.R. Peters**, M. Cox, A. Drozdov and A. Forbes, 2023. The invariance and distortion of vectorial light across a real-world free space link. *Applied Physics Letters*, Volume 123, Issue 2, 021103.

4. **C.R. Peters**, P. Ornelas, I. Nape and A. Forbes, 2023. Spatially resolving classical and quantum entanglement with structured photons *Physical Review A*, Volume 108, 053502.

List of International Conference Proceedings

1. A. Forbes, K. Singh, I. Nape and **C. Peters** . 2023. Communicating distortion-free through atmospheric turbulence. Optica Imaging Congress: Propagation Through and Characterization of Atmospheric and Oceanic Phenomena, Boston, USA.

2. **C. Peters**, A. Klug, A. Forbes. 2023. The eigenmodes of atmospheric turbulence. Photonics West: Complex Light and Optical Forces XVII, San Francisco, USA.

3. **C. Peters**, W.T. Buono, J. Tau, I. Nape, A. Forbes . 2023. The eigenmodes of the tilted lens. Photonics West: Complex Light and Optical Forces XVII, San Francisco, USA.

4. **C. Peters**, A. Klug, A. Forbes . 2022. Structuring Light for Robust Optical Communication Through Atmospheric Turbulence. International Conference on Light and Light Based Technologies 2022, Ankara, Turkey.

List of Local Conference Proceedings

1. **C. Peters**, P. Ornelas, I. Nape, A. Forbes. 2023. Uncovering the spatial distribution of entanglement using vectorial light (Oral Presentation). SAIP - Photonics Track, Richards Bay, South Africa.

2. **C. Peters**, M. Cox, A. Drozdov, A. Forbes. 2023. The invariance and distortion of vectorial light through real-world turbulence (Oral Presentation). SAIP - Applied Physics Track, Richards Bay, South Africa.

3. **C. Peters**, A. Klug, A. Forbes, . 2022. Tailoring Noise Invariant Light for Robust Optical Communication (Oral Presentation). SAIP - Applied Physics Track, Nelson Mandela Bay, South Africa.

4. **C. Peters**, W.T. Buono, J. Tau, I. Nape, A. Forbes, . 2022. A New Angle on the Tilted Lens (Oral Presentation). SAIP - Photonics Track, Nelson Mandela Bay, South Africa.

Dedicated to my parents.

Chapter 1

Structured Light and Eigenmodes of Free Space

1.1 Structured Waves

1.1.1 The Electromagnetic Wave Equation

This work is concerned with the behaviour of classical structured light fields. To see where the structure of these fields come from, we will begin our discussion with Maxwell's equations from which all of classical electromagnetism can be derived. These are [1]:

$$\nabla \cdot \mathbf{D} = \rho \,, \tag{1.1}$$
$$\nabla \cdot \mathbf{B} = 0 \,, \tag{1.2}$$
$$\nabla \times \mathbf{E} = -\frac{\partial \mathbf{B}}{\partial t} \,, \tag{1.3}$$
$$\nabla \times \mathbf{H} = \mathbf{J} + \frac{\partial \mathbf{D}}{\partial t} \,, \tag{1.4}$$

where $\mathbf{E}$ is the electric field, $\mathbf{B}$ is the magnetic field, ρ is the free charge density, $\mathbf{J}$ is the free current density, $\mathbf{D}$ is the electric displacement and $\mathbf{H}$ is the magnetising field which are defined as:

$$\mathbf{D} = \epsilon_0 \mathbf{E} + \mathbf{P} \,, \tag{1.5}$$
$$\mathbf{B} = \frac{1}{\mu_0} \mathbf{H} - \mathbf{M} \,, \tag{1.6}$$

where $\mathbf{P}$ is the polarisation, $\mathbf{M}$ is the magnetisation and ϵ_0 and μ_0 are the vacuum permittivity and permeability respectively. For classical light in free space, we can assume that there are no charges and currents. Maxwell's equations then simplify to:

$$\nabla \cdot \mathbf{E} = 0 \,, \tag{1.7}$$
$$\nabla \cdot \mathbf{B} = 0 \,, \tag{1.8}$$
$$\nabla \times \mathbf{E} = \frac{\partial \mathbf{B}}{\partial t} \,, \tag{1.9}$$
$$\nabla \times \mathbf{B} = \mu_0 \epsilon_0 \frac{\partial \mathbf{E}}{\partial t} \,. \tag{1.10}$$

If we take the curl on both sides of Equation 1.9 and invoke the vector identity $\nabla \times (\nabla \times \mathbf{A}) = \nabla(\nabla \cdot \mathbf{A}) - \nabla^2\mathbf{A}$, to obtain $\nabla \times (\nabla \times \mathbf{E}) = \nabla(\nabla \cdot \mathbf{E}) - \nabla^2\mathbf{E}$. If we now substitute Equations 1.7 and 1.9 on the RHS of the above expression we yield,

$$\nabla \times \frac{\partial \mathbf{B}}{\partial t} = \nabla^2 \mathbf{E}\,. \tag{1.11}$$

We may then substitute Equation 1.10 into the above and rewrite it as,

$$\nabla^2 \mathbf{E} - \frac{1}{c^2}\frac{\partial^2 \mathbf{E}}{\partial t^2} = 0\,, \tag{1.12}$$

where $c = 1/\sqrt{\epsilon_0 \mu_0}$ is the speed of light in a vacuum. Equation 1.12 is in the form of the wave equation and so observe that the electric field can be described as a propagating wave. A similar substitution procedure can be performed to show that the magnetic field $\mathbf{B}$ may also be represented as propagating wave. Such an equation describes the propagation of disturbances/waves through free space. Consequently, if one is able to find solutions to this equation, one would have found functions (also called modes) that are able to propagate without changing their functional form through free space. Such modes are known as eigenmodes of free space, coined as such because they would be eigenstates of the free space propagation operator. Unfortunately, Equation 1.12 is quite difficult to solve in its current form. We will make several assumptions in the rest of this section to simplify the wave equation and extract solutions that we can generate and study.

1.1.2 The Helmholtz Equation and Bessel-Gaussian Modes

To find our first set of solutions, we make the separation of variables ansatz $\mathbf{E}(\mathbf{r}, t) = \mathbf{U}(\mathbf{r})\,\mathbf{T}(t)$ where we assume our light field's spatial behaviour $U(r)$ can be described separately from its temporal behaviour $T(t)$. Applying this to the wave equation derived above, we obtain the Helmholtz equation for the spatial function:

$$\nabla^2 \mathbf{U}(\mathbf{r}) + k^2 \mathbf{U}(\mathbf{r}) = 0\,, \tag{1.13}$$

where k is a constant which can be shown to be the modulus of the wavevector. The wavevector is related to the wavelength via $k = 2\pi/\lambda$.

The first exact solution we will look at are plane waves, which have the form:

$$\mathbf{U}(\mathbf{r}) = A e^{i\mathbf{k}\cdot\mathbf{r}}\,, \tag{1.14}$$

where A is a constant parameter indicating the amplitude of the electric field. The factor $\mathbf{k} = k_x\hat{x} + k_y\hat{y} + k_z\hat{z}$ is the wave-vector indicating the direction of propagation. Such waves are defined by infinitely long planes of constant phase which are normal to the wave-vector $\mathbf{k}$. These waves are not physically realisable as they would require an infinite amount of energy to construct. However, they are useful mathematical tools for modelling wave propagation as any wave can be written as a superposition of plane waves. This will be discussed in detail later in this section when we deal with the propagation of light fields.

Another set of exact solutions to Helmholtz equation (Equation 1.13) are called Bessel modes and are described by Bessel functions of the first kind. Bessel modes are non-diffracting, meaning they do not change in propagation and are thus true eigenmodes of free space. However, they are not physically realisable as the relevant Bessel functions are unbounded and would require an infinite amount of energy to construct. Luckily, a Gaussian envelope can be added to the function to make it physically realisable and non-diffracting over specific finite regions by ensuring the mode has a finite energy. Such modes are known as Bessel-Gaussian (BG) modes, are defined in cylindrical (r, ϕ) coordinates and can be written as:

$$BG_l = \underbrace{J_{|l|}(k_r r)}_{\text{A}} \underbrace{e^{-\frac{r^2}{w_0^2}}}_{\text{B}} \underbrace{e^{ik_z z}}_{\text{C}} \underbrace{e^{il\phi}}_{\text{D}} . \tag{1.15}$$

Factor A represents the spatial profile as described by the Bessel function of the first kind $J_{|l|}$. The subscript $|l|$ indicates the order of the Bessel function. The term k_r is the radial component of the wave-vector and r is the magnitude of the radial coordinate. Factor B represents the Gaussian envelope with a waist given by w_0. Factor C represents the propagation phase which is accumulated in propagation and depends on the component of the wave-vector in the direction of propagation $k_z = \sqrt{k^2 - k_r^2}$. Factor D indicates the azimuthal phase variation. The wavenumber k is related to wavelength λ by $k = 2\pi/\lambda$. The modes are non-diffracting up to a distance $z_{max} = kw_0/k_r$. The index variable l can take on positive and negative integer values and corresponds to the topological charge of the mode. The topological charge arises due to the phase singularity in the centre of the mode and is a result of the a spiral phase profile for nonzero values of l. This in turn is related to the orbital angular momentum (OAM) of the mode in which each photon in the field will have an OAM of $l\hbar$. Figure 1.1 shows the intensity and phase profiles of various BG beams.

1.1.3 Solutions to the Paraxial Helmholtz Equation

To find fully realisable solutions of the wave equation and thus physical eigenmodes of free space that are truly propagation invariant, we make the paraxial approximation. Here we assume that the wave propagates primarily in one direction (which will be chosen as the z-direction for this work unless otherwise specified). This means we can describe the spatial component of our field as a complex envelope $\mathbf{A}(\mathbf{r})$ multiplied by some propagation phase factor:

$$\mathbf{U}(\mathbf{r}) = \mathbf{A}(\mathbf{r}) e^{ikz} . \tag{1.16}$$

We then assume that the complex envelope does not rapidly change in propagation (i.e., it is approximately constant when propagating a distance on the order of one wavelength). This results in the paraxial Helmholtz equation:

$$\nabla_\perp^2 \mathbf{A} e^{ikz} + 2ik\partial_z \mathbf{A} = 0 , \tag{1.17}$$

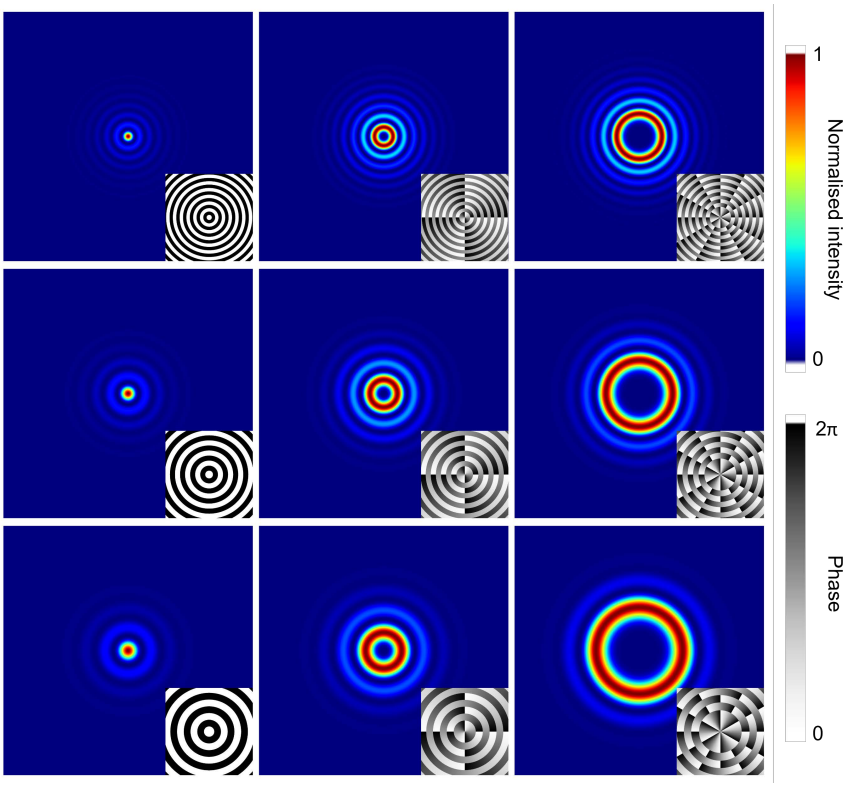


FIGURE 1.1: **Bessel-Gaussian Beams.** The intensity (main images) and phase (insets) profiles of various Bessel-Gaussian beams. All have a beam waist of $w_0 = 2$ mm. The rows show increasing topological charge $l = 0, 2, 6$, and the columns show an increase in the radial component of the wave vector $k_r = k/1000, k/1500, k/2000$ where k is the total wavenumber.

where $\nabla_\perp^2$ is the transverse Laplacian (i.e., the Laplacian only in the x-y plane) and ∂_z is the partial derivative in the z-direction.

The solutions to the paraxial Helmholtz equation are a class of light fields known as paraxial modes which diffract slowly and propagate primarily in a single direction. The most general solutions are known as vector modes and have inhomogeneous polarisation structures meaning the electric field may oscillate in different directions depending on the location in the transverse plane. This dissertation will focus on the scalar mode solutions which have an electric field that oscillates uniformly across the transverse plane, however many of the techniques and concepts demonstrated here may be generalised to vector modes.

Hermite-Gaussian Modes

In order to solve the paraxial Helmholtz equation, we will have to make some assumptions to simplify our field $U(x, y, z)$. If one assumes the field $U(x, y, z)$ has Cartesian symmetry, it is most convenient to make the following separation of variables ansatz $U(x, y, z) = X(x, z)Y(y, z)$, and so rewrite

the paraxial Helmholtz equation as:

$$\left(\frac{\partial^2}{\partial x^2}+\frac{\partial^2}{\partial y^2}+2ik\frac{\partial}{\partial z}\right)U=0\,. \tag{1.18}$$

The solutions to Equation 1.18 are known as Hermite-Gaussian (HG) modes and are given by:

$$HG_n^m=\underbrace{\sqrt{\frac{2^{1-n-m}}{w^2(z)\pi n!m!}}}_{\text{A}}\underbrace{H_n\left(\frac{\sqrt{2}x}{w(z)}\right)H_m\left(\frac{\sqrt{2}y}{w(z)}\right)}_{\text{B}}\underbrace{e^{-\frac{r^2}{w^2(z)}}}_{\text{C}}\underbrace{e^{ik\frac{r^2}{2R(z)}}}_{\text{D}}\underbrace{e^{i(m+n+1)\psi(z)}}_{\text{E}}\,. \tag{1.19}$$

Factor A is a normalisation factor for the mode with the beam waist/spot size goven by

$$w(z)=w_0\sqrt{1+\left(\frac{z}{z_R}\right)^2}\,, \tag{1.20}$$

representing the beam waist as a function of propagation distance and $w_0 = w(0)$. The Rayleigh range $z_R = \frac{1}{2}kw_0^2$ is the distance at which the beam area has exactly doubled. The variables n and m represent the horizontal and vertical indices respectively and uniquely specify each HG mode. They can be any non-negative integer and can be interpreted visually as the number of intensity fringes in the x and y directions respectively. The total mode order is given as $M = m + n + 1$. Factor B represents the spatial profile in the x and y directions define by Hermite polynomials H_j of order j and factor C describes the Gaussian envelope. Factor D describes how the radius of curvature of the wavefront $R(z) = z\left[1+\left(\frac{z_R}{z}\right)^2\right]$ changes in propagation. Factor E describes the effect of the Gouy phase shift factor $(m+n+1)\psi(z) = (m+n+1)\arctan(z/z_R)$ which additionally depends on the mode order M. Figure 1.2 shows the intensity and phase profiles of various HG beams.

Laguerre-Gaussian Modes

If one assumes the solution to the paraxial Helmholtz equations instead have cylindrical symmetry, one may also the use a different separation of variables ansatz, $U(r,\phi,z) = R(r,z)\Phi(\phi,z)$. In this case, we may rewrite the equation as:

$$\left(\frac{1}{r}\frac{\partial}{\partial r}+\frac{\partial^2}{\partial r^2}+\frac{1}{r^2}\frac{\partial^2}{\partial \phi^2}+2ik\frac{\partial}{\partial z}\right)U=0\,, \tag{1.21}$$

Solutions to Equation 1.21 are known as Laguerre-Gaussian (LG) modes and are given by:

$$LG_p^l=\underbrace{\sqrt{\frac{2p!}{w^2(z)\pi(p+|l|)!}}}_{\text{A}}\underbrace{\left(\frac{r\sqrt{2}}{w(z)}\right)^{|l|}}_{\text{B}}\underbrace{L_p^{|l|}\left(\frac{2r^2}{w^2(z)}\right)}_{\text{C}}\underbrace{e^{-\frac{r^2}{w^2(z)}}}_{D}\underbrace{e^{ik\frac{r^2}{2R(z)}}}_{\text{E}}\underbrace{e^{il\phi}}_{\text{F}}\underbrace{e^{i(2p+|l|+1)\xi(z)}}_{\text{G}}, \tag{1.22}$$

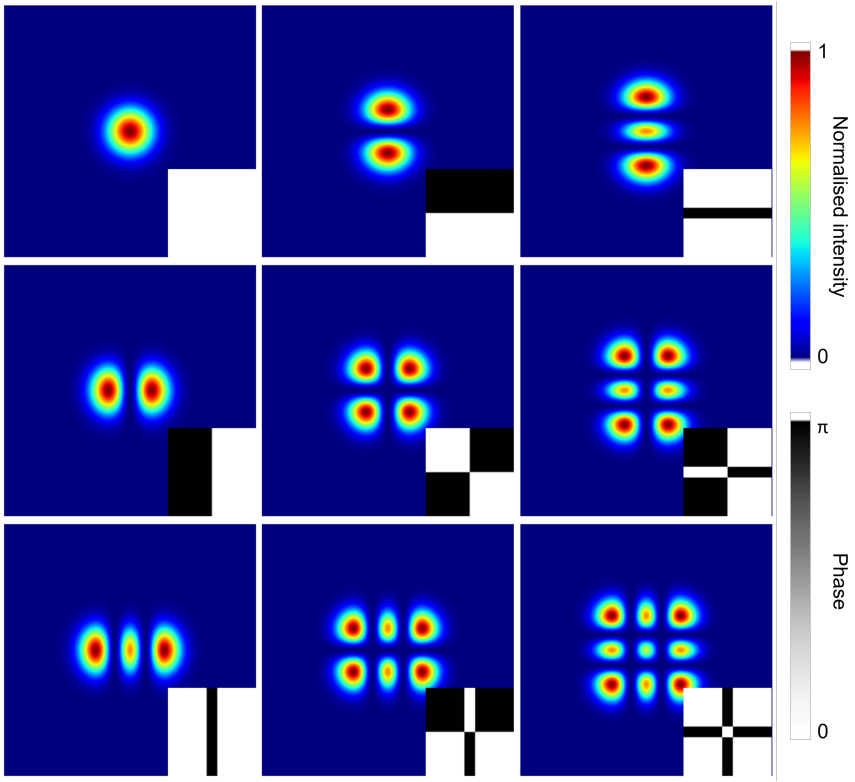


FIGURE 1.2: **Hermite-Gaussian Beams.** The intensity (main images) and phase (insets) profiles of various Hermite-Gaussian beams. All have a beam waist of $w_0 = 0.5$ mm. The rows show increasing vertical index $m = 0, 1, 2$, and the columns show an increase in the horizontal index $n = 0, 1, 2$.

Factor A represents the mode normalisation with all the variables representing the same as before. The variables p and l uniquely index each LG mode. The radial order is controlled by the p index which can have any non-negative integer value. For values of $l = 0$, the number of rings in the LG mode is equal to p. For non-zero values of l, the number of rings in the mode is equal to $p + 1$. Factors B and C control the radial behaviour of the mode along with the Gaussian envelope in Factor D. Here $L_p^{|l|}$ is the associated Laguerre polynomial, with its argument being $2r^2/w^2(z)$. Factor E represents how the radius of curvature of the wavefront changes in propagation. Factor F the spiral phase of LG beams. The topological charge is controlled by l which can take any integer value, positive or negative. As with the Bessel-Gaussian beams, this topological charge results from the spiral phase front of the mode and is related to the orbital angular momentum (OAM) of the mode. Each photon in the field will have an OAM of $l\hbar$. Factor G describes the effect of the Gouy phase $(2p + |l| + 1)\psi = (2p + |l| + 1) \arctan(z/z_R)$ which additionally depends on the mode order $M = (2p + |l| + 1)$. Figure 1.3 shows the intensity and phase profiles of various LG beams.

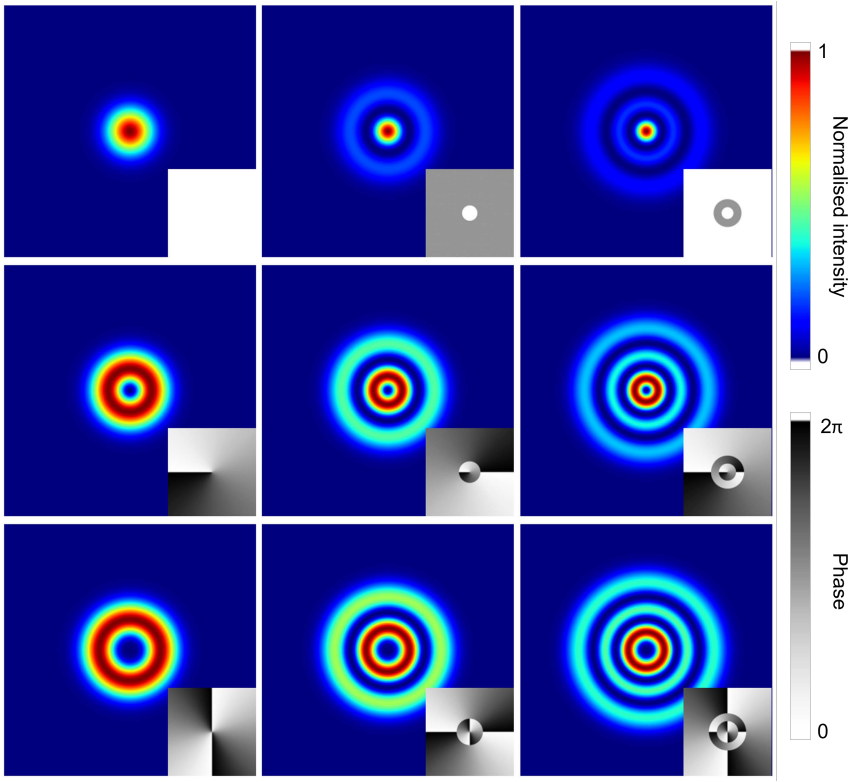


FIGURE 1.3: **Laguerre-Gaussian Beams.** The intensity (main images) and phase (insets) profiles of various Laguerre-Gaussian beams. All have a beam waist of $w_0 = 0.5$ mm. The rows show increasing radial index $p = 0, 1, 2$, and the columns show an increase in the topological charge $l = 0, 1, 2$.

1.2 Propagation of Light through Free Space

We have found shapes of light that satisfy the paraxial Helmholtz equation and we believe these to be eigenmodes of free space propagation due to the assumptions we have made. It remains for us to study the mathematical descriptions of wave propagation in order to verify the invariance of these modes and also see how we must adjust our approach when faced with more complex media and channels. Such mathematics also has many other applications outside of optics, including in the fields of quantum mechanics and quantum field theory where the study of wavefunctions and quantum fields reveal similar mathematical structures.

There are several methods used to model the propagation of light fields. We will examine two models which bare significant relevance in the following chapters. The first model, which will be discussed in this section, is Huygens-Fresnel diffraction which is a more fundamental approach to understanding the behaviour of waves in propagation. We begin by studying the insights that can be gained from the Helmholtz equation through the use of Green's functions. This will provide a basic type of wave which we can study and thus use to build up the more complicated theory of arbitrary diffraction. We then proceed to apply this Green's function approach to describe the propagation of arbitrary light fields and derive Huygens' principle.

We then end of with a discussion on the propagation of paraxial light fields, which form the vast majority of fields discussed in this work.

1.2.1 Green's Functions

As we have seen in the previous sections, the dynamics of optical fields are described by various partial differential equations. A very useful technique used in finding solutions for such equations involves the use of Green's functions. To see how this approach works, we may define the following ordinary differential equation (ODE) with a differential operator $\hat{L}$,

$$\hat{L}(t)f(t) = g(t), \quad \hat{L} = \sum_{j=0}^{n} a_j(t)\frac{\mathrm{d}^j}{\mathrm{d}t^j}\,. \tag{1.23}$$

We note here that any function may be describe as a weighted sum of Dirac delta functions. For example,

$$g(t) = \int g(u)\delta(t-u)\mathrm{d}u\,. \tag{1.24}$$

Using this fact, we chose solutions of our ODE that have the form

$$f(t) = \int G(u,t)g(u)\mathrm{d}u\,, \tag{1.25}$$

and rewrite our ODE as follows,

$$\begin{aligned} \hat{L}f(t) &= g(t)\,, \\ \Rightarrow \int \hat{L}G(u,t)g(u)\mathrm{d}u &= \int g(u)\delta(t-u)\mathrm{d}u\,, \\ \Rightarrow \hat{L}G(u,t) &= \delta(t-u)\,. \end{aligned} \tag{1.26}$$

The function $G(u,t)$ is known as the Green's function of the problem. If it can be found then solution to the ODE, $f(t)$ may then also be easily found via Equation 1.25. Such a method is highly beneficial because it turns an inhomogeneous differential equation into a homogeneous differential equation if the domain for u and t are appropriately chosen thus making the problem significantly easier to solve.

1.2.2 Free Space Green's Function

Green's Functions and the Helmholtz Equation

We return to the Helmholtz equation (Equation 1.13), which was derived by assuming that our field's spatial behaviour can be described separately from its temporal behaviour. We can add to it a driving term $f(\mathbf{r})$, which turns the Helmholtz equation into an inhomogeneous, partial differential equation:

$$\nabla^2 U(\mathbf{r}) + k^2 U(\mathbf{r}) = f(\mathbf{r})\,. \tag{1.27}$$

We can make use of the Green's function approach and look for solutions that have the form:

$$U(\mathbf{r}) = \int G(\mathbf{r}, \mathbf{r}') f(\mathbf{r}') \mathrm{d}^3 r' \,, \tag{1.28}$$

where $G(\mathbf{r}, \mathbf{r}')$ is the Green's function and must satisfy:

$$\left(\nabla^2 + k^2\right) G(\mathbf{r}, \mathbf{r}') = \delta(\mathbf{r} - \mathbf{r}') \,. \tag{1.29}$$

This may be immediately recognised as a point source equation, which will later help validate the final form of the Green's function we derive. Before we may begin to solve for $G(\mathbf{r}, \mathbf{r}')$, we must first state a vital boundary conditions for our problem. We know from experience that light field spread out as they propagate and thus must be defined over all of space. We also wish to find solutions that are physically realisable and so must be bounded. We must therefore impose the condition that as $r \to \infty$, $G(\mathbf{r}, \mathbf{r}') \to 0$. This way the entire integral in Equation1.28 will be bounded and physically realisable.

Our first step in solving for $G(\mathbf{r}, \mathbf{r}')$ is to take note of the symmetries present in our problem. We know that the Laplacian operator ∇^2 is invariant under translation as derivatives evaluate the change in quantities and not their absolute values at a point. We also note that the Dirac delta function is translation invariant as it depends on the difference between two point $\mathbf{r} - \mathbf{r}'$. Additionally, we see that our imposed boundary condition is also translation invariant as it is concerned with the functions behaviour at infinity, which should not change under any finite translation. Thus we may assert that the Green's, whatever its final form, should also be invariant under translation. This implies that we may stop writing it as a function of two variables $\mathbf{r}$ and $\mathbf{r}'$ and instead write it as function of the difference between the two coordinates $\mathbf{R} = \mathbf{r} - \mathbf{r}'$. Thus $G(\mathbf{r}, \mathbf{r}') = G(\mathbf{r} - \mathbf{r}')$ and so Equation 1.29 becomes

$$\left(\nabla^2 + k^2\right) G(\mathbf{R}) = \delta(\mathbf{R}) \,. \tag{1.30}$$

This may then be solved by taking advantage of Fourier transforms. The Fourier transforms of our Green's function $G(\mathbf{r})$ and the Dirac delta function $\delta(\mathbf{r})$ allow us to express them both as,

$$G(\mathbf{R}) = \frac{1}{(2\pi)^3} \int \tilde{G}(\mathbf{q}) e^{i\mathbf{q}\cdot\mathbf{R}} \mathrm{d}^3 q \,, \tag{1.31}$$

$$\delta(\mathbf{R}) = \frac{1}{(2\pi)^3} \int e^{i\mathbf{q}\cdot\mathbf{R}} \mathrm{d}^3 q \,. \tag{1.32}$$

We can then rewrite Equation 1.30 as follows,

$$\left(\nabla^2 + k^2\right) \frac{1}{(2\pi)^3} \int \tilde{G}(\mathbf{q}) e^{i\mathbf{q}\cdot\mathbf{R}} \mathrm{d}^3 q = \frac{1}{(2\pi)^3} \int e^{i\mathbf{q}\cdot\mathbf{R}} \mathrm{d}^3 q \,. \tag{1.33}$$

Recalling that the Laplacian acts only in $\mathbf{r}$ we may perform the differentiation on the right hand side and compare both sides to obtain,

$$\begin{aligned}(k^2 - q^2)\tilde{G}(\mathbf{q}) &= 1\,,\\ \Rightarrow \tilde{G}(\mathbf{q}) &= \frac{-1}{q^2 - k^2}\,.\end{aligned} \tag{1.34}$$

If we are now able to invert the Fourier transform on $\tilde{G}(\mathbf{q})$, we will have our solution. We begin by substituting this result in to Equation 1.31,

$$G(\mathbf{R}) = \frac{-1}{(2\pi)^3}\int \frac{1}{q^2 - k^2} e^{i\mathbf{q}\cdot\mathbf{R}} \mathrm{d}^3 q\,. \tag{1.35}$$

Our Green's function depends on $\mathbf{R}$, which is a radius and thus it is beneficial to compute the integral in spherical coordinates. If we chose the axes in real space $\mathbf{R}$ to align with the axes in Fourier space $\mathbf{q}$, we may perform the angular parts of the integral quite easily.

$$\begin{aligned}G(\mathbf{R}) &= \frac{-1}{(2\pi)^3}\int_0^{2\pi}\int_0^{\pi}\int_0^{\infty} \frac{1}{q^2 - k^2} e^{iqR\cos\theta}\mathrm{d}q q\mathrm{d}\theta q\sin\theta\mathrm{d}\phi\\ &= \frac{-2\pi}{(2\pi)^3}\int_0^{\infty}\frac{q^2}{q^2 - k^2}\int_0^{\pi} e^{iqR\cos\theta}\sin\theta\mathrm{d}\theta\mathrm{d}q\\ &= \frac{-1}{4\pi^2}\int_0^{\infty}\frac{2\sin Rq}{Rq}\frac{q^2}{q^2 - k^2}\mathrm{d}q\\ &= \frac{1}{2\pi^2 R}\int_0^{\infty}\sin Rq\frac{q}{q^2 - k^2}\mathrm{d}q\,.\end{aligned} \tag{1.36}$$

We have now reached a critical point as the above equation is infinite due the poles at $q = \pm k$ in the integrand. To circumvent this, we will expand the scope of our integration from the real line onto the complex plane.

Complex Integrals and Feynman's Trick

Our value for the Green's function is, for the time being infinite. This seemingly troubling result can be overcome by employing a limiting procedure commonly known as "Feynman's trick" which shifts the poles of the integrand and changes the integral from a line integral over the real numbers to a contour integral over the complex plane. Before we implement this, it is beneficial to express our Green's function in a complex form,

$$\begin{aligned}G(R) &= \frac{1}{2\pi^2 R}\int_0^{\infty}\sin Rq\frac{q}{q^2 - k^2}\mathrm{d}q\\ &= \frac{1}{4\pi^2 R}\int_{-\infty}^{\infty}\sin Rq\frac{q}{q^2 - k^2}\mathrm{d}q\\ &= \frac{1}{8\pi^2 Ri}\underbrace{\int_{-\infty}^{\infty}\frac{qe^{iqR}}{q^2 - k^2}\mathrm{d}q}_{\mathrm{A}} - \frac{1}{8\pi^2 Ri}\underbrace{\int_{-\infty}^{\infty}\frac{qe^{-iqR}}{q^2 - k^2}\mathrm{d}q}_{\mathrm{B}}\,.\end{aligned} \tag{1.37}$$

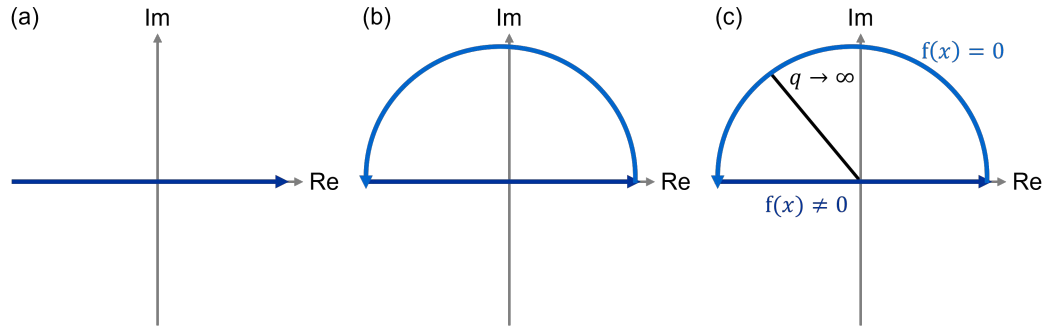


FIGURE 1.4: **Complex Contour Integrals.** (a) The direction of integral of A over the real line. (b) The proposed contour integral for solving integral A. (c) If the integrand is zero along the light blue portion of the contour integral then there will be no additional contributions to the integral from this part of the contour and thus is equivalent to the real line integral. For integral A this occurs as $q \to \infty$.

In the second line we have extended the limits of integration from $\{0, \infty\}$ to $\{-\infty, \infty\}$ and in the third line we have made use of the complex exponential identity $\sin(\theta) = [e^{i\theta} - e^{-i\theta}]/2i$. We first look at integral A. In order for the integral over the real line to be equal to a contour integral over the complex plane, the value of the integrand must go to zero when the contour lies off the real line. The behaviour of our integrand at infinity should be dominated by the exponential factor and thus we must determine where on the complex plane the exponential factor will go to zero. On the real line this is normally straight forward, but for our purposes, q is in general complex. Thus we separate q into its real and imaginary parts $q = q_r + iq_i$,

$$e^{iRq} = e^{iR(q_r+iq_i)} = e^{iRq_r+i^2Rq_i} = e^{iRq_r-Rq_i}\,. \tag{1.38}$$

Thus we see that the integrand goes to zeros for $R > 0$ and thus we must close the contour in the upper half of the complex plane. This concept is shown visually in Figure 1.4. Since the integrand is zero as $R \to 0$, there are no additional contributions to the integral if we close the contour at infinity in the upper half of the complex plane. It is therefore equivalent to the real line integral. A similar argument holds for integral B which, with the negative in the exponential, requires the contour to be closed in the bottom half of the complex plane instead. Thus we may write,

$$G(R) = \frac{1}{8\pi^2 Ri}\underbrace{\oint_{P_+}\frac{qe^{iqR}}{q^2-k^2}\mathrm{d}q}_{\mathrm{A}} - \frac{1}{8\pi^2 Ri}\underbrace{\oint_{P_-}\frac{qe^{-iqR}}{q^2-k^2}\mathrm{d}q}_{\mathrm{B}}\,. \tag{1.39}$$

Where P_+ indicates the contour in the upper half plane and P_- the contour in the bottom half plane.

We have established that the real line integral can be replaced with an appropriate contour integral. This is useful as it allows us to apply the Residue

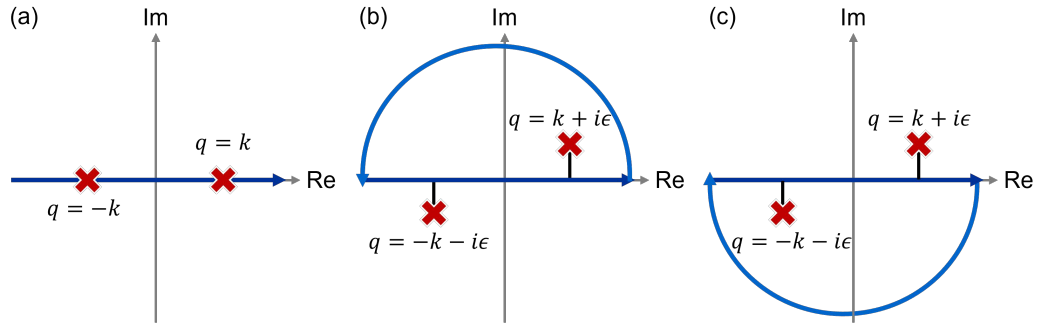


FIGURE 1.5: **Feynman's Trick.** (a) The poles present in the initial integral. (b) The contour integral for solving integral A in the top half of the plane will pick up the residue of pole at $q = k + i\epsilon$. (c) The contour integral for solving integral B in the bottom half of the plane will pick up the residue of pole at $q = -k - i\epsilon$.

Theorem from Complex Analysis. This theorem provides a relationship between the contour integral of a function over a closed path and the residues of the poles located inside that contour. Motivated by this, we will shift the poles of our integrands located at $q = \pm k$, off the real line and onto the complex plane by a distance ϵ so that the new poles are located at $q = \pm(k + i\epsilon)$. We can evaluate the contour integrals using the Residue Theorem along our newly defined contour paths $P_{\pm}$. To maintain the equivalence of this shifted configuration to the original configuration, we will take the limit as $\epsilon \to \infty$. The Green's function may now be written as,

$$G(R) = \frac{1}{8\pi^2 Ri} \lim_{\epsilon\to\infty} \underbrace{\oint_{P_+} \frac{qe^{iqR}}{q^2 - (k+i\epsilon)^2} \mathrm{d}q}_{\text{A}} - \frac{1}{8\pi^2 Ri} \lim_{\epsilon\to\infty} \underbrace{\oint_{P_-} \frac{qe^{-iqR}}{q^2 - (k+i\epsilon)^2} \mathrm{d}q}_{\text{B}} . \tag{1.40}$$

When we apply the Residue Theorem, as shown in Figure 1.5, integral A will pick up the residue from the pole at $q = k + i\epsilon$ in the upper-half plane and integral B will pick up the residue from the pole at $q = -k - i\epsilon$ in the

lower-half plane. The computation is as follows:

$$\begin{aligned}
G(R) &= \frac{1}{8\pi^2 Ri}\lim_{\epsilon\to\infty}\left[\oint_{P_+}\frac{qe^{iqR}}{q^2-(k+i\epsilon)^2}\mathrm{d}q-\oint_{P_-}\frac{qe^{-iqR}}{q^2-(k+i\epsilon)^2}\mathrm{d}q\right]\\
&= \frac{1}{8\pi^2 Ri}\lim_{\epsilon\to\infty}\left[\oint_{P_+}\frac{qe^{iqR}}{[q-(k+i\epsilon)][q+(k+i\epsilon)]}\mathrm{d}q\right.\\
&\quad\left.-\oint_{P_-}\frac{qe^{-iqR}}{[q-(k+i\epsilon)][q+(k+i\epsilon)]}\mathrm{d}q\right]\\
&= \frac{1}{8\pi^2 Ri}\lim_{\epsilon\to\infty}\left[2\pi i\frac{(k+i\epsilon)e^{i(k+i\epsilon)R}}{(k+i\epsilon)+(k+i\epsilon)}-(-2\pi i)\frac{(-k-i\epsilon)e^{-i(-k-i\epsilon)R}}{(-k-i\epsilon)+(-k-i\epsilon)}\right]\\
&= \frac{1}{4\pi R}\lim_{\epsilon\to\infty}\left[\frac{e^{i(k+i\epsilon)R}}{2}+\frac{e^{i(k+i\epsilon)R}}{2}\right]\\
&= \frac{1}{4\pi R}\lim_{\epsilon\to\infty}\left[e^{i(k+i\epsilon)R}\right]\\
&= \frac{1}{4\pi R}e^{ikR}. \qquad (1.41)
\end{aligned}$$

We have now determined that for the Helmholtz equation, the appropriate Green's function is a spherical wave with the form,

$$G(\mathbf{r}-\mathbf{r}') = \frac{1}{4\pi|\mathbf{r}-\mathbf{r}'|}e^{ik|\mathbf{r}-\mathbf{r}'|}. \qquad (1.42)$$

This Green's function may then be used to find solutions to the inhomogeneous Helmholtz Equation 1.27 by substituting the above Green's function 1.42 into Equation 1.28 as follows,

$$U(\mathbf{r}) = \int\frac{1}{4\pi|\mathbf{r}-\mathbf{r}'|}e^{ik|\mathbf{r}-\mathbf{r}'|}f(\mathbf{r}')\mathrm{d}^3r'. \qquad (1.43)$$

1.2.3 Scalar Diffraction Theory

The following section is adapted primarily from reference [2].

Green's Theorem

The fundamental mathematical principle underlying scalar diffraction is that of Green's Theorem. This theorem states:

Let U and G be complex functions that depend on position in 3D space. Let S be a closed surface enclosing a volume V. If U and G and their 1st and 2nd partial derivatives are single valued and continuous on S then,

$$\iiint_V(U\nabla^2G-G\nabla^2U)\mathrm{d}V = \oiint_S\left(U\frac{\partial G}{\partial\mathbf{n}}-G\frac{\partial U}{\partial\mathbf{n}}\right)\mathrm{d}S, \qquad (1.44)$$

where $\partial/\partial\mathbf{n}$ is the derivative in the direction normal to the surface S.

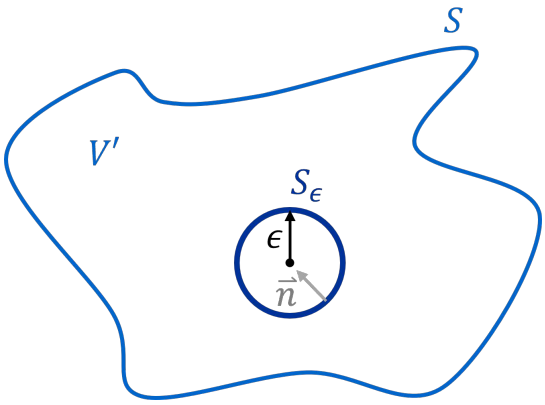


FIGURE 1.6: **Surfaces for Green's Theorem.** The construction of the surfaces S', S and S_ϵ for the evaluation of Green's Theorem in optical diffraction.

We will take U to be the complex spatial profile of our optical field in 3D. The function G is an auxiliary Green's function. As we showed in the previous section, the natural choice for Green's function in free space propagation is that of a spherical wave. We will define the source point of this spherical wave to be $\mathbf{r_0}$ and so our wave will have the form,

$$G(\mathbf{r}-\mathbf{r_0}) = \frac{e^{ik|\mathbf{r}-\mathbf{r_0}|}}{|\mathbf{r}-\mathbf{r_0}|} = \frac{e^{ikR}}{R} = G(R)\,. \tag{1.45}$$

We will define the surface S to surround the point $\mathbf{r_0}$. The conditions for the use of Green's theorem imply we cannot have a singularity inside of our volume V. Thus we must isolate the singularity at $\mathbf{r} = \mathbf{r_0}$. To achieve this, we will construct a spherical shell S_ϵ of radius ϵ centred on the point $\mathbf{r_0}$. We will then be able to apply Green's Theorem on the surface $S' = S + S_\epsilon$ and the volume V' it encloses without having to worry about the singularity. This construction is shown in Figure 1.6.

Helmholtz-Kirchhoff Integral Theorem

We know that both our Green's function G and the optical field U must satisfy the Helmholtz equation on S' and in V',

$$(\nabla^2 + k^2)U = 0 \;\Rightarrow \nabla^2 U = -k^2 U\,, \tag{1.46}$$
$$(\nabla^2 + k^2)G = 0 \;\Rightarrow \nabla^2 G = -k^2 G\,. \tag{1.47}$$

The delta function is zero as $\mathbf{r_0}$ lies outside of S'. We can substitute this result into the left hand side of Equation 1.44 to obtain,

$$\iiint_{V'} (U\nabla^2 G - G\nabla^2 U)\mathrm{d}V = \iiint_{V} (-Uk^2 G + Gk^2 U)\mathrm{d}V = 0\,. \tag{1.48}$$

This means we can break up the surface integral over S' into a sum of two integrals, one over S_ϵ and the other over S as follows,

$$\begin{aligned} 0 &= \iint_{S'} \left(U\frac{\partial G}{\partial \mathbf{n}} - G\frac{\partial U}{\partial \mathbf{n}} \right) \mathrm{d}S = \iint_{S} \left(U\frac{\partial G}{\partial \mathbf{n}} - G\frac{\partial U}{\partial \mathbf{n}} \right) \mathrm{d}S + \iint_{S_\epsilon} \left(U\frac{\partial G}{\partial \mathbf{n}} - G\frac{\partial U}{\partial \mathbf{n}} \right) \mathrm{d}S\,, \\ \Rightarrow \iint_{S} \left(U\frac{\partial G}{\partial \mathbf{n}} - G\frac{\partial U}{\partial \mathbf{n}} \right) \mathrm{d}S &= -\iint_{S_\epsilon} \left(U\frac{\partial G}{\partial \mathbf{n}} - G\frac{\partial U}{\partial \mathbf{n}} \right) .\mathrm{d}S \end{aligned} \tag{1.49}$$

The surface S can be any arbitrary surface and so would be difficult to perform a surface integral over. The integral over S_ϵ is defined as a sphere and is included to explicitly exclude the point $\mathbf{r_0}$. If we take the limit as $\epsilon \to 0$, we can easily compute the surface integral and not worry about any issues that may arise from constructing a strict surface and excluding points that may be necessary.

The derivative of the Green's function with respect to $\mathbf{n}$ is in general given by:

$$\frac{\partial G(R)}{\partial \mathbf{n}} = \frac{e^{ikR}}{R}\cos(\mathbf{n},\mathbf{r})\left(ik - \frac{1}{R}\right)\,, \tag{1.50}$$

where $\cos(\mathbf{n},\mathbf{r})$ is the cosine of the angle between the vectors $\mathbf{n}$ and $\mathbf{r}$. The normal vector of the surface S_ϵ will always point opposite to the vector $\mathbf{r}$ and so for the surface $\cos(\mathbf{n},\mathbf{r}) = -1$. Thus we have,

$$\left.\frac{\partial G(R)}{\partial \mathbf{n}}\right|_{S_\epsilon} = \frac{e^{ik\epsilon}}{\epsilon}\left(\frac{1}{\epsilon} - ik\right)\,. \tag{1.51}$$

The surface element of a sphere is given by $\mathrm{d}S = \mathrm{d}\rho\rho^2\mathrm{d}\Omega$, where $\mathrm{d}\rho$ is the radial measure and $\mathrm{d}\Omega$ is the solid angle measure. Thus, the surface integral is evaluated as follows,

$$\begin{aligned} &\lim_{\epsilon\to 0} \iint_{S_\epsilon} \left(U\frac{\partial G}{\partial \mathbf{n}} - G\frac{\partial U}{\partial \mathbf{n}} \right) \mathrm{d}S \\ &= \lim_{\epsilon\to 0} 4\pi\epsilon^2 \left[U\frac{e^{ik\epsilon}}{\epsilon}\left(\frac{1}{\epsilon} - ik\right) - \frac{e^{ik\epsilon}}{\epsilon}\frac{\partial U}{\partial \mathbf{n}} \right] \\ &= \lim_{\epsilon\to 0} 4\pi U e^{ik\epsilon} - \lim_{\epsilon\to 0} 4\pi\epsilon U e^{ik\epsilon} ik - \lim_{\epsilon\to 0} 4\pi\epsilon e^{ik\epsilon}\frac{\partial U}{\partial \mathbf{n}} \\ &= 4\pi U(\mathbf{r_0})\,. \end{aligned} \tag{1.52}$$

Substituting Equation 1.52 into 1.49 and rearranging gives us our first expression for our optical field,

$$U(\mathbf{r_0}) = \frac{1}{4\pi}\iint_S \left(G\frac{\partial U}{\partial \mathbf{n}} - U\frac{\partial G}{\partial \mathbf{n}} \right) \mathrm{d}S\,. \tag{1.53}$$

This final equation is known as the Helmholtz-Kirchhoff Integral Theorem. While this is a good first step, we will need to make some further assumption and observations in order to obtain a calculable field.

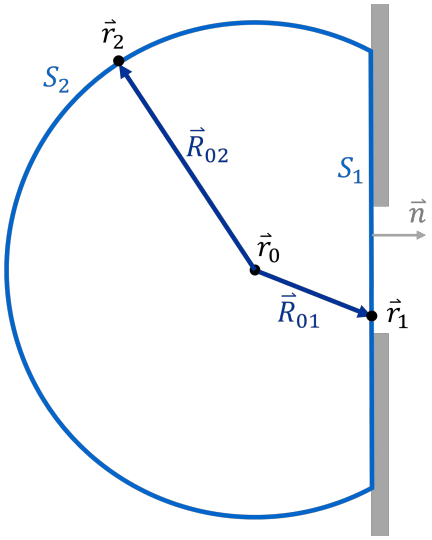


FIGURE 1.7: **Diffraction through an Aperture.** The construction of the surfaces $S = S_1 + S_2$ for the evaluation of diffraction through an aperture.

Sommerfield Radiation Condition

We will now have to be more specific in the type of system we which to examine. It is informative to study the diffraction of a field through an aperture. To apply the Helmholtz-Kirchhoff Integral Theorem, we must make a choice of surface S. We will choose S to be the sum of a spherical cap facing in the opposite direction of the aperture and finite plane co-planar with the barrier and aperture. The construction is shown Figure 1.7. We therefore have,

$$\begin{aligned} U(\mathbf{r_0}) &= \frac{1}{4\pi}\iint_S \left(G\frac{\partial U}{\partial \mathbf{n}} - U\frac{\partial G}{\partial \mathbf{n}}\right) \mathrm{d}S \\ &= \frac{1}{4\pi}\iint_{S_1} \left(G\frac{\partial U}{\partial \mathbf{n}} - U\frac{\partial G}{\partial \mathbf{n}}\right) \mathrm{d}S \\ &\quad + \frac{1}{4\pi}\iint_{S_2} \left(U\frac{\partial G}{\partial \mathbf{n}} - G\frac{\partial U}{\partial \mathbf{n}}\right) \mathrm{d}S\,. \end{aligned} \tag{1.54}$$

We will first evaluate the integral over S_2. The derivative of the Green's function can be obtained from Equation 1.50 and knowing that R_{02} and $\mathbf{n}$ point in the same direction,

$$\frac{\partial G(R)}{\partial \mathbf{n}} = \frac{e^{ikR_{02}}}{R_{02}}\left(ik - \frac{1}{R_{02}}\right)\,. \tag{1.55}$$

Since most optical wavelengths are very small in scale, the wavenumber k is very large. Thus for larger values of R_{02}, we may approximate $ik >> 1/R_{02}$ and have,

$$\frac{\partial G(R)}{\partial \mathbf{n}} = \frac{e^{ikR_{02}}}{R_{02}}\left(ik - \frac{1}{R_{02}}\right) \approx \frac{e^{ikR_{02}}}{R_{02}} ik = ikG\,. \tag{1.56}$$

Using this and noting that the surface element on S_2 is given by $\mathrm{d}S = R_{02}^2 \mathrm{d}\Omega$, we may approximate our surface integral over S_2 as,

$$\begin{aligned} \iint_{S_2} \left(G\frac{\partial U}{\partial \mathbf{n}} - U\frac{\partial G}{\partial \mathbf{n}} \right) \mathrm{d}S &\approx \int_{\Omega_2} \left(G\frac{\partial U}{\partial \mathbf{n}} - UikG \right) R_{02}^2 \mathrm{d}\Omega \\ &= \int_{\Omega_2} GR_{02} \left(\frac{\partial U}{\partial \mathbf{n}} - ikU \right) R_{02} \mathrm{d}\Omega \,, \end{aligned} \tag{1.57}$$

where Ω_2 is the solid angle subtended by S_2 and the point $\mathbf{r_0}$ The term $GR_{02} = e^{ikR_{02}}$ and thus is bounded and will vanish as $R_{02} \to \infty$. The entire surface integral will then only vanish if the following holds,

$$\lim_{R_{02}\to\infty} \left(\frac{\partial U}{\partial \mathbf{n}} - ikU \right) R_{02} = 0 \,. \tag{1.58}$$

This is known as the Sommerfield Radiation Condition and is useful to impose as it means we need not worry about evaluating the integral over S_2 and it will not contribute to the overall integral. We may then focus solely on the integral over S_1 which focuses on the lights interaction with the barrier and aperture. The physical interpretation of the Sommerfield Radiation Condition is that our field falls off at least as fast as outgoing spherical waves and ensures the field is not dominated by incoming waves, which would blow up at infinity.

Huygens-Fresnel Diffraction

By imposing the Sommerfield Radiation Condition, we may simply evaluate our surface integral over S_1,

$$U(\mathbf{r_0}) = \frac{1}{4\pi} \iint_{S_1} \left(G\frac{\partial U}{\partial \mathbf{n}} - U\frac{\partial G}{\partial \mathbf{n}} \right) \mathrm{d}S \,. \tag{1.59}$$

Such an integral is still challenging to evaluate and can be simplified further. We may adjust our choice of Green's function so that it is zero along all of S_1. In this way, we may get rid of the first term in the integrand. Since we do not want to re-check all of our already established assumptions and conditions, we can chose our new Green's function to be a superposition of two spherical waves. We know all of conditions hold for a single spherical wave, and because all of the equations and conditions we have dealt with so far are linear, they should be equally valid when applied to a sum of spherical waves. For this sum to be zero along S_1, the source of the second spherical wave should be at a point that mirrors $\mathbf{r_0}$ across the barrier/aperture. This point shall be labelled $\mathbf{r_0}'$. The geometry of this configuration is shown in Figure 1.8 This wave should also be 180° out of phase with the initial spherical wave so that they both destructively interfere at S_1 leading to a null field along the surface

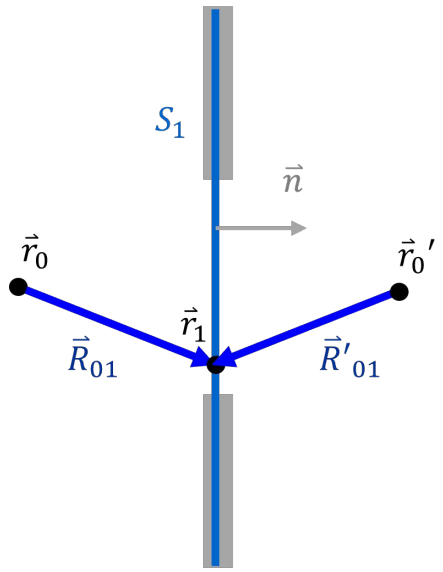


FIGURE 1.8: **Geometry of the New Green's Function.** The geometry of the points of interest for defining the new Green's function.

of integration. The form of this new Green's function $G_{new}(\mathbf{r_1})$ is then,

$$G_{new}(\mathbf{r}) = \frac{e^{ik|\mathbf{r}-\mathbf{r_0}|}}{|\mathbf{r}-\mathbf{r_0}|} - \frac{e^{ik|\mathbf{r}-\mathbf{r_0}'|}}{|\mathbf{r}-\mathbf{r_0}'|}\,. \tag{1.60}$$

Because $G_{new}(\mathbf{r_1}) = 0$, this choice allows to simplify Equation 1.59 to,

$$U(\mathbf{r_0}) = \frac{1}{4\pi}\iint_{S_1}\left(G\frac{\partial U}{\partial \mathbf{n}} - U\frac{\partial G}{\partial \mathbf{n}}\right)\mathrm{d}S = \frac{-1}{4\pi}\iint_{S_1} U\frac{\partial G}{\partial \mathbf{n}}\mathrm{d}S\,. \tag{1.61}$$

To make our plane of integration more physical, We shall now apply what are known as the Kirchhoff Boundary Conditions:

- Along the aperture (a subsurface Σ of the surface S_1), the field behaves as if the barrier is not present at all. While this is not completely true, it is a reasonable assumption for apertures that are several orders of magnitude larger than the wavelength.
- Along the region of S_1 that coincide with the barrier, we have $U = 0$. This is imposed because we know the light cannot propagate through the barrier.

We may then change the surface if integration to be,

$$U(\mathbf{r_0}) = \frac{-1}{4\pi}\iint_{\Sigma} U\frac{\partial G}{\partial \mathbf{n}}\mathrm{d}S\,. \tag{1.62}$$

Recalling that the derivative of a single spherical wave is given by Equation 1.50, we can easily find the derivative of our new Green's function,

$$\frac{\partial G_{new}}{\partial \mathbf{n}} = \frac{e^{ikR_{01}}}{R_{01}} \cos(\mathbf{n}, \mathbf{R_{01}}) \left(ik - \frac{1}{R_{01}} \right) - \frac{e^{ikR'_{01}}}{R'_{01}} \cos(\mathbf{n}, \mathbf{R_{01}}') \left(ik - \frac{1}{R'_{01}} \right) . \tag{1.63}$$

For any point along S_1, we know $R_{01} = R'_{01}$ and $\cos(\mathbf{n}, \mathbf{R_{01}}) = -\cos(\mathbf{n}, \mathbf{R_{01}}')$ due to the mirrored symmetry of the system. Thus we may simplify the expression for the derivative to,

$$\begin{aligned} \frac{\partial G_{new}}{\partial \mathbf{n}} &= \frac{2e^{ikR_{01}}}{R_{01}} R_{01} \cos(\mathbf{n}, \mathbf{R_{01}}) \left(ik - \frac{1}{R_{01}} \right) \\ &\approx 2ik \frac{e^{ikR_{01}}}{R_{01}} \cos(\mathbf{n}, \mathbf{R_{01}}) , \end{aligned} \tag{1.64}$$

by also assuming that the distance propagated to the aperture is much larger than the wavelength, i.e., $R_{01} >> \lambda$. Substituting this into Equation 1.62 gives,

$$\begin{aligned} U(\mathbf{r_0}) &= \frac{-1}{4\pi} \iint_\Sigma U(\mathbf{r_1}) 2ik \frac{e^{ikR_{01}}}{R_{01}} \cos(\mathbf{n}, \mathbf{R_{01}}) dS \\ &= \frac{-2ik}{4\pi} \iint_\Sigma U(\mathbf{r_1}) \frac{e^{ikR_{01}}}{R_{01}} \cos(\mathbf{n}, \mathbf{R_{01}}) dS \\ &= \frac{1}{i\lambda} \iint_\Sigma U(\mathbf{r_1}) \frac{e^{ikR_{01}}}{R_{01}} \cos(\mathbf{n}, \mathbf{R_{01}}) dS . \end{aligned} \tag{1.65}$$

This result is known as the Huygens-Fresnel diffraction integral. Physically, it states that the optical field at some point $\mathbf{r_0}$ is a weighted sum of spherical waves all originating at points along a surface Σ some distance away from the point. These weightings are directly related to the field at this surface $U(\mathbf{r_1})$. The amplitude of these spherical waves is inversely proportional to the wavelength of the field and these waves are 90° out of phase with the field at the surface Σ.

1.2.4 Paraxial Light Propagation

This work will focus primarily on the propagation of paraxial structured light fields. We will use the conventions that all modes will be propagating in the $+z$ direction. The z-component of these fields is also assumed to be very small and thus negligible. For an arbitrary field and the geometry as shown in Figure 1.9, the Huygens-Fresnel diffraction integral can be written as,

$$U(\mathbf{r}) = \frac{1}{i\lambda} \iint U(\mathbf{r}') \frac{e^{ik|\mathbf{r}-\mathbf{r}'|}}{|\mathbf{r}-\mathbf{r}'|} \cos\theta d^2 r' , \tag{1.66}$$

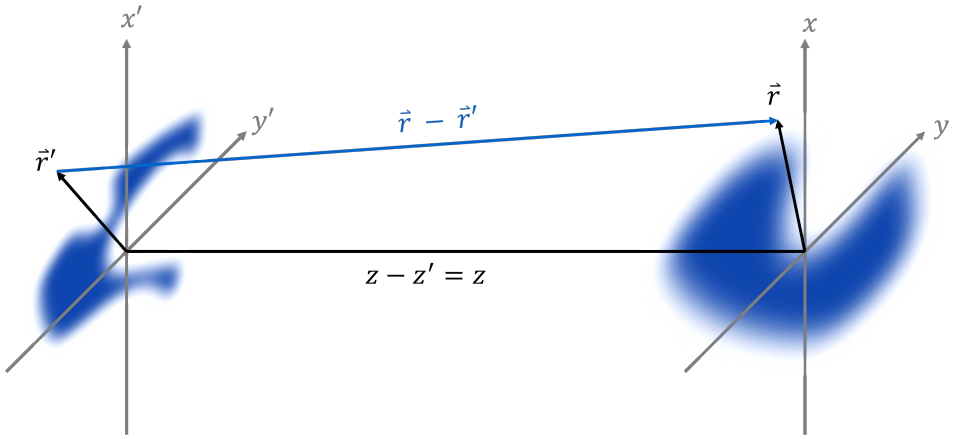


FIGURE 1.9: **Geometry for the Diffraction of Paraxial Waves.** The construction of the surfaces S', S and S_ϵ for the evaluation of Green's Theorem in optical diffraction.

where $\mathbf{r}'$ are the spatial coordinates in the initial plane, $\mathbf{r}$ are the spatial coordinates in the final plane and $\cos\theta = z/|\mathbf{r}-\mathbf{r}'|$ where z is the distance between the final and initial plane. If we assume that we are propagating distances significantly larger than the typical length scale of our fields, we can then assume that $z \approx |\mathbf{r}-\mathbf{r}'|$ and $\cos\theta = z/|\mathbf{r}-\mathbf{r}'| \approx 1$. This simplifies the integral to,

$$U(\mathbf{r}) = \frac{1}{i\lambda}\iint U(\mathbf{r}')\frac{e^{ik|\mathbf{r}-\mathbf{r}'|}}{z}(1)\mathrm{d}^2r' = \frac{1}{i\lambda z}\iint U(\mathbf{r}')e^{ik|\mathbf{r}-\mathbf{r}'|}\mathrm{d}^2r'\,, \tag{1.67}$$

This approximation cannot be applied to the argument of the exponential factor as the presence of the wavenumber k implies that even a small difference between z and $|\mathbf{r}-\mathbf{r}'|$ that of the same order of magnitude as the wavelength λ, which can be very small, will result in non-negligible changes in the exponential factor. To deal with this, we will implement the Fresnel approximation.

Fresnel Approximation

The Fresnel approximation requires the use of the binomial approximation which, for some value $x \ll 1$, we have that,

$$(1+x)^\alpha \approx 1 + \alpha x\,. \tag{1.68}$$

If we analyse the length factor in the argument of the exponential and assume that again we have propagation distances that are larger than the length scale

of our field $z \gg |r - r'| \Rightarrow 1 \gg |r - r'|/z$, we have,

$$\begin{aligned}
|\mathbf{r} - \mathbf{r}'| &= \sqrt{(x - x')^2 + (y - y')^2 + z^2} \\
&= \left[z^2 + (x - x')^2 + (y - y')^2\right]^{\frac{1}{2}} \\
&= z\left[1 + \left(\frac{x - x}{z}\right) + \left(\frac{y - y}{z}\right)\right]^{\frac{1}{2}} \\
&\approx z\left[1 + \frac{1}{2}\left(\frac{x - x}{z}\right) + \frac{1}{2}\left(\frac{y - y}{z}\right)\right] \\
&= z + \frac{1}{2z}\left[(x - x')^2 + (y - y')^2\right] \\
&= z + \frac{|\mathbf{r} - \mathbf{r}'|}{2z}\,. \qquad (1.69)
\end{aligned}$$

This approximation replaces the spherical surfaces of the spherical waves with parabolic surfaces which are approximately equal at large propagation distances. Our integral becomes,

$$\begin{aligned}
U(\mathbf{r}) &= \frac{1}{i\lambda z}\iint U(\mathbf{r}')e^{ik\left[z + \frac{|\mathbf{r}-\mathbf{r}'|}{2z}\right]}\mathrm{d}^2 r' \\
&= \frac{e^{ikz}}{i\lambda z}\iint U(\mathbf{r}')e^{\frac{ik}{2z}|\mathbf{r}-\mathbf{r}'|}\mathrm{d}^2 r'\,. \qquad (1.70)
\end{aligned}$$

The result of these approximations allow us to accurately describe the paraxial propagation of light after any distance z. An important term in this expression that will become prominent later on in this work is known as the paraxial free space Green's function,

$$g(\mathbf{r}, \mathbf{r}'; z) = \frac{1}{i\lambda z}e^{\frac{ik}{2z}|\mathbf{r}-\mathbf{r}'|}\,. \qquad (1.71)$$

It is named as such because it plays a similar role in the paraxial diffraction integral as spherical waves do in the Huygens-Fresnel diffraction integral. The spherical Green's function implies that a wave at any point in the output plane can be described as a weighted sum of spherical waves weighted by the spatial profile of the wave at the input plane. In the paraxial case, we no longer describe the output wave as a superposition of spherical waves, but instead as a superposition of plane waves.

Fraunhofer Approximation

The final approximation will allows us to easily obtain the distribution of the optical field in the far-field (i.e., when the final plane is a large distance away from the initial plane.). We will make what is known as the Fraunhofer approximation which will help further simplify the exponential factor. This approximation is physically realised by observing that in general, when optical fields propagate, they tend to increase in size. Thus over very large

propagation distances the length scale of the initial field will be much small than the length scale of the final field in the far-field. We can thus assume that $|\mathbf{r}| > |\mathbf{r}'| \Rightarrow |\mathbf{r}|^2 >\!\!> |\mathbf{r}'|^2$. This allows us to approximate the factor $|\mathbf{r} - \mathbf{r}'|$ as,

$$|\mathbf{r} - \mathbf{r}'| = |\mathbf{r}|^2 - 2\mathbf{r}\cdot\mathbf{r}' + |\mathbf{r}'|^2 \approx |\mathbf{r}|^2 - 2\mathbf{r}\cdot\mathbf{r}' \,. \tag{1.72}$$

Thus, the diffraction integral can be written as follows,

$$\begin{aligned} U(\mathbf{r}) &\approx \frac{e^{ikz}}{i\lambda z} \iint U(\mathbf{r}') e^{\frac{ik}{2z}(|\mathbf{r}|^2 - 2\mathbf{r}\cdot\mathbf{r}')} \mathrm{d}^2 r' \\ &= \frac{e^{ikz}}{i\lambda z} e^{\frac{ik}{2z}|\mathbf{r}|} \iint U(\mathbf{r}') e^{\frac{-ik}{z}(\mathbf{r}\cdot\mathbf{r}')} \mathrm{d}^2 r' \,. \end{aligned} \tag{1.73}$$

We may then write the Fraunhofer diffraction integral as,

$$U(\mathbf{r}) = \frac{e^{ikz}}{i\lambda z} e^{\frac{ik}{2z}(x^2+y^2))} \iint U(\mathbf{r}') e^{\frac{-ik}{z}(xx'+yy')} \mathrm{d}^2 r' \,. \tag{1.74}$$

An interesting property of this equation reveals itself when noticing that the integral is a Fourier transform,

$$\tilde{U}(u,v) = \mathcal{F}(U(x',y')) = \iint (U(x',y') e^{\frac{-ik}{z}(xx'+yy')} \mathrm{d}x' \mathrm{d}y' \,, \tag{1.75}$$

where $u = kx'/z$ and $v = ky'/z$. Thus the far-field distribution of an optical field is simply the Fourier transform of the initial field multiplied by some phase factors. The far-field intensity is then simply the Fourier transform of the initial field.

$$U(\mathbf{r}) = \frac{e^{ikz}}{i\lambda z} e^{\frac{ik}{2z}(x^2+y^2))} \mathcal{F}(U(x',y')) \,. \tag{1.76}$$

1.2.5 Angular Spectrum Propagation

Fourier transforms have numerous applications in numerous fields. Their widespread use and versatility has resulted in numerous algorithms optimising the numerical calculation of Fourier transforms through the discrete Fourier transform. This makes them an efficient and versatile computational tool and provide a much faster route for simulating various phenomena. The field of optics can take advantage of these improved and streamlined methods for simulating the propagation of complex, spatially varying optical fields. To do this, we will need to make two assumptions:

1. The optical field is travelling along a propagation axis which we will label z.

2. The spatial profile of the field is known in some plane $z = 0$. We shall call the field in this plane $U(x, y, z = 0)$.

To begin, assume we have some arbitrary, spatially varying optical field $U(x, y, z)$. We may take the 2-dimensional Fourier transform of this field as

follows:

$$A(u,v;z) = \iint_{-\infty}^{\infty} U(x,y,z)e^{i2\pi(ux+vy)}\mathrm{d}x\mathrm{d}y\,. \tag{1.77}$$

This may then be inverted to recover $U(x,y,z)$ as follows,

$$U(x,y,z) = \iint_{-\infty}^{\infty} A(u,v;z)e^{-i2\pi(ux+vy)}\mathrm{d}u\mathrm{d}v\,. \tag{1.78}$$

We see that in the argument of the exponential we have both spatial coordinates and frequency/Fourier coordinates. This structure is very similar to that of a plane wave. The spatial profile of a plane wave can be written as,

$$U_{plane}(x,y,z) = e^{i\mathbf{k}\cdot\mathbf{r}} = e^{i(k_x x+k_y y+k_z z)} = e^{i\frac{2\pi}{\lambda}(\alpha x+\beta y+\gamma z))}\,, \tag{1.79}$$

with $|k| = 2\pi/\lambda$ where λ is the wavelength and $\alpha^2+\beta^2+\gamma^2 = 1$. We may isolate the z-component as follows,

$$e^{i\frac{2\pi}{\lambda}(\alpha x+\beta y+\gamma z)} = e^{i\frac{2\pi}{\lambda}(\alpha x+\beta y)}e^{i\frac{2\pi}{\lambda}\gamma}\,. \tag{1.80}$$

Comparing this to the exponential in Equations 1.77 and 1.78, we can see that $\alpha = u\lambda$ and $\beta = v\lambda$. Clearly then, by taking the Fourier transform of our field, we are decomposing the field into a weighted infinite sum of plane waves of varying spatial frequencies. The weighting coefficients for each of these plane waves are given by the function $A(u,v;z)$ and is therefore called the *angular spectrum* of the field $U(x,y,z)$.

If one knows the profile of $U(x,y,0)$, then it is simple to calculate $A(k_x,k_y;0)$ via Equation 1.77 which gives us the angular spectrum (plane wave decomposition) of the field. This is useful as the propagation dynamics of plane waves are much easier to study than those of an arbitrary field. Thus, if we are able to relate $A(u,v;0)$ to $A(u,v;z)$, we may use Equation 1.78 to calculate $U(x,y,z)$. To to do this, we must go back to the Helmholtz Equation 1.13. The field $U(x,y,z)$ must describe a propagating wave and thus must satisfy Equation 1.13. This implies that $A(k_x,k_y;z)$ should also satisfy Equation 1.13 as follows,

$$\nabla^2 A(u,v;z) + k^2 A(u,v;z) = 0\,. \tag{1.81}$$

It follows from this that $A(k_x,k_y;z)$ must also satisfy the 1-dimensional Helmholtz equation in each of the 3 Cartesian directions. Since our field is propagating in the z-direction, we are particularly interested in how it changes in the z-direction and sp will focus on the z-component,

$$\frac{\partial^2}{\partial z^2}A(u,v;z) + k_z^2 A(u,v;z) = \frac{\partial^2}{\partial z^2}A(u,v;z) + \frac{2\pi}{\lambda}(1-\alpha^2-\beta^2)A(u,v;z) = 0\,. \tag{1.82}$$

This is just the 1-dimensional Helmholtz equation, its solution is a 1-dimensional plane wave given by,

$$A(u,v;z) = A(u,v;0)e^{i\frac{2\pi}{\lambda}z\sqrt{1-\alpha^2-\beta^2}} = A(u,v;0)e^{i\frac{2\pi}{\lambda}z\sqrt{1-u^2\lambda^2-v^2\lambda^2}}\,, \tag{1.83}$$

This tells us that in propagation, plane waves simply gain a phase factor proportional to the distance of propagation z and the spatial frequencies. We may then substitute Equation 1.83 into 1.78 to obtain an profile of our field in the new plane $U(x,y,z)$,

$$U(x,y,z) = \iint_{-\infty}^{\infty} A(u,v;0) e^{i\frac{2\pi}{\lambda}z\sqrt{1-u^2\lambda^2-v^2\lambda^2}} e^{-i(ux+vy)} \mathrm{d}u\mathrm{d}v\,. \tag{1.84}$$

Thus, given an initial field in a particular plane $z = 0$, $U(x,y,0)$, we may succinctly relate it to the field at some later plane z as follows:

$$U(x,y,z) = \mathcal{F}^{-1}\{\mathcal{F}[U(x,y,0)] e^{i\frac{2\pi}{\lambda}z\sqrt{1-u^2\lambda^2-v^2\lambda^2}}\}\,, \tag{1.85}$$

where $\mathcal{F}(\cdot)$ represents the Fourier transform operator. Since this method is significantly more computationally efficient than others, it is used through the remainder of this work to simulate the propagation of light fields. Numerical simulations of several structured light beams using the angular spectrum propagation method are given in Figure 1.10. Here we see that as the beams propagate, they maintain the same shape and simply expand/diverge. This is in accordance with their analytical forms. This demonstrates numerically that they are indeed eigenmodes of free space vacuum propagation. The divergence of the beams is important to note in situations where one is propagating large distances. A detector/receiver must be appropriately sized to detect the entire spatial profile as the beam will have expanded after propagation. If this is not done, this will lead to a loss of light. The phase profiles of these beams do change its profile, but this is in accordance with their analytical definitions in Equation 1.19 for the HG modes and Equation 1.22. Thus, the spiral phases of the LG beams and the chequerboard phase patterns of the HG beams remain unchanged in propagation, only with some added curvature.

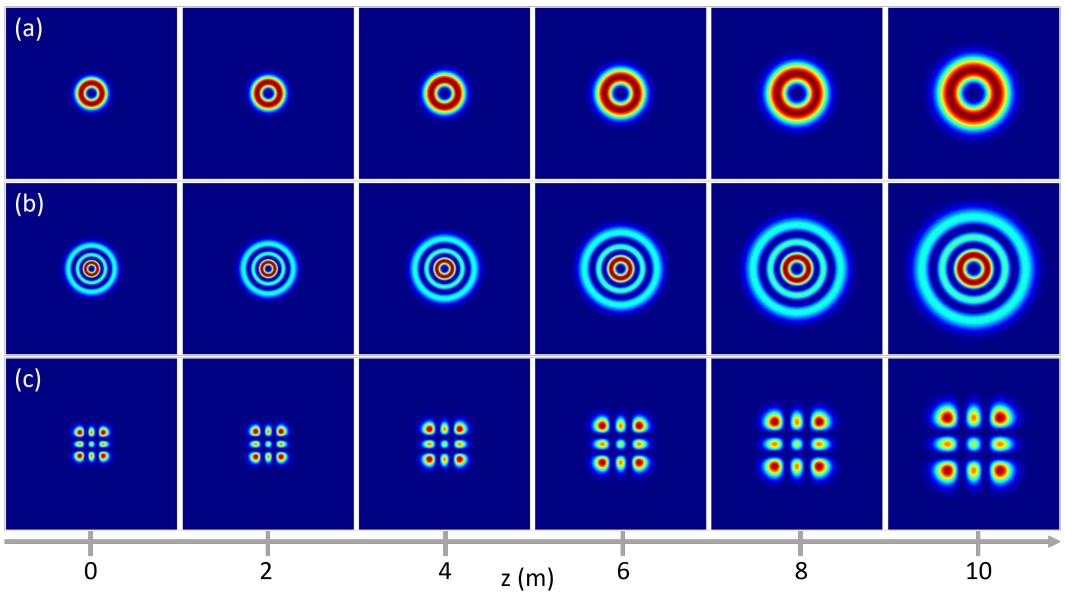


FIGURE 1.10: **Angular Spectrum Propagation.** Simulations showing the use of the angular spectrum method to model the propagation of various structured light modes (a) LG_0^2, (b) LG_2^2 and (c) HG_2^2 over a distance of 10 metres. The initial beam waist for all these modes is $w_0 = 1$ mm.

Chapter 2

Experimental Techniques

Throughout the rest of this work, several experimental techniques are implemented to generate structured light fields and impart spatially varying aberrations to directly simulate complex channels. This section will give a brief overview of several techniques employed in creating experimental setups capable of producing structured modes and replicating complex channels. We will give an overview of the devices used for beam shaping, known as SLMs and DMDs, which are versatile digital devices controlling and tailoring the amplitude and phase of incident light fields.

2.1 Liquid Crystal in Silicon Structured Light Modulators

2.1.1 Liquid crystals and Refractive Index

Liquid crystals have long been studied for their optical properties, offering precise control over various aspect of optical waves and exhibiting useful birefingent properties. For the purpose of spatially structured light, they have been employed in devices known as liquid crystal on silicon spatial light modulators (LCoSSLMs or simply SLMs). Such devices consist of a screen divided up into numerous, microscopic square pixels (in this work the typical pixel size in about 8 μm $\times$ 8 μm). Each pixel contains asymmetric, oval shaped liquid crystals sandwiched between transparent silicon wafers.

The phase of an electromagnetic wave changes according to [1]

$$\mathrm{d}\phi = \frac{2\pi}{\lambda}(n\mathrm{d}z + z\mathrm{d}n)\,, \tag{2.1}$$

where $\mathrm{d}\phi$ represents an infinitesimal change in the phase at a particular point in space, λ is the wavelength, n is the refractive index of the material and z is the propagation distance. Thus, the transverse phase of a beam can be changed by making the refractive index a spatially varying function. While this can be done by also changing the thickness of the medium at different points (i.e. making $textdz$ a spatially varying function), this is not the working principle of the SLMs used in this work and so will not be discussed here. Liquid crystals are birefringent and have differing refractive indices depending on the direction through which light propagates through the crystal. This

difference is quantified by assigning two axes: the ordinary axis with refractive index n_o and an extraordinary axis with refractive index n_e. The liquid crystal's birefringence is quantified by the difference in the two quantities $\Delta n = n_e - n_o$. The birefringence itself manifests due to asymmetries in the crystal's lattice structure which result in differing interactions depending on the light's incident polarisation.

The pixels of an SLM each contain electrodes. By applying a voltage across the pixel, one is able to independently rotate the liquid crystals contained in each pixel. This change in orientation alters the refractive index of the crystals' extraordinary axis according to [3]

$$\frac{1}{n_e} = \frac{\cos^2\theta}{n_{e0}^2} + \frac{\sin^2\theta}{n_o^2}, \tag{2.2}$$

where θ is the angle of rotation and n_{e0} is the refractive index of the extraordinary axis at an angle $\theta = 0°$. The changing voltage thus changes the refractive index experienced by the incident light field and modulates it according to Equations 2.1 and 2.2. The desired voltage is communicated to the SLM through the use of an 8-bit grey-scale image, where the grey-level is directly related to the applied voltage. While several SLMs are able to advance the phase to high multiples of π radians. The SLMs used in this work are only able to advance the phase in the interval $[0, 2\pi]$. A diagram showing the structure of the pixels in the SLM screen is given in Figure 2.1. SLMs used in this work have 8-bit depth meaning there are 256 grey levels. There exist SLMs with higher and lower bit depths where a higher bit depth allows one to more finely control the phase retardation applied to the beam at each pixel. However, in all of these cases one is able to impart a spatially varying transverse phase profile $\phi(x, y)$ onto an incident beam by making the refractive index vary in space $n = n(x, y)$ through the use of independently controlled liquid crystals on the SLM screen.

2.1.2 Complex amplitude modulation with a Phase-Only Hologram

Several methods for SLM hologram generation are given in Ref [4] and the primary method used in this work will be outlined in this section. In this work we wish to shape paraxial light beams in the transverse plane and so our hologram will be treated a single phase elements with a uniform (and very thin) thickness and a phase profile that varies only in the transverse plane. We also make two assumptions about the incident field. The first is that it is composed of monochromatic light. This is a reasonable assumption given that in this work, the fields being shaped are generated by a laser of wavelength 63 nm and a spectral width of between 1-2 nm. The second is that the incident field is uniformly polarised and aligned with the birefringent axes of the liquid crystals. Thus, the birefringence of the crystals is used only as a means to vary the phase spatially in the transverse plane and the effects on other polarisations can be ignored. In order to shape light into a

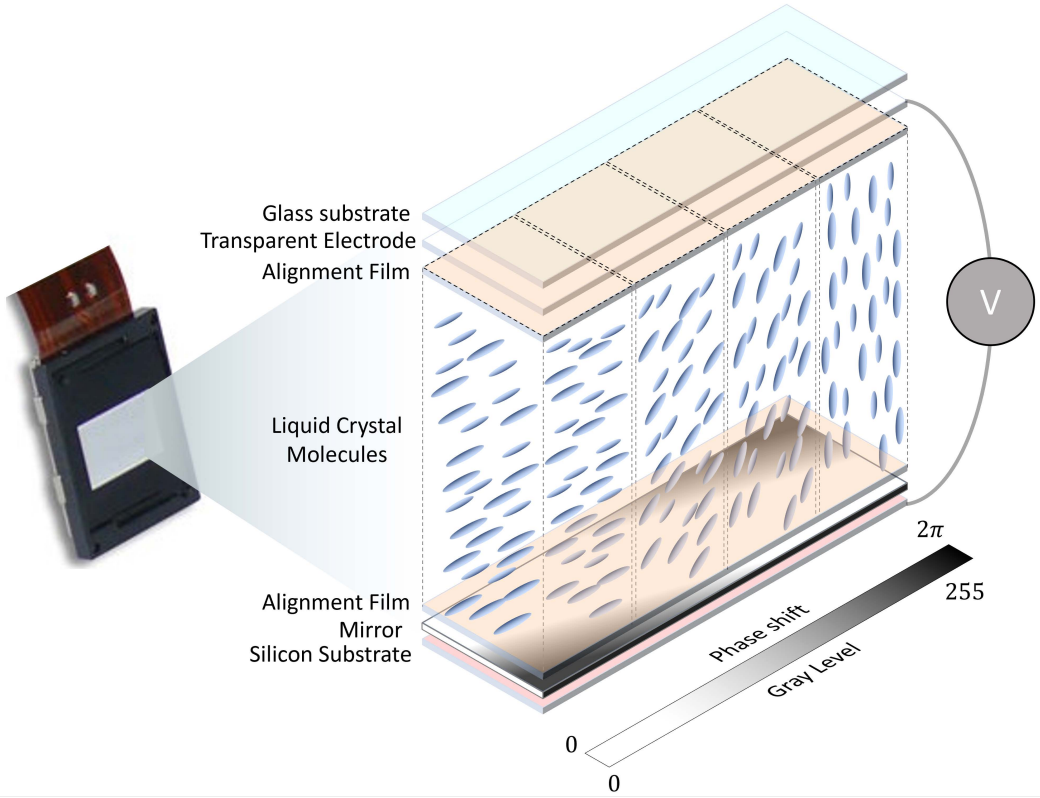


FIGURE 2.1: **Liquid Crystal Phase Modulation.** The pixels of the SLM each contain birefringent liquid crystals. When a voltage is applied to the pixel, the liquid crystals are rotated. This change in orientation combined with the birefringence allows us to control the phase imparted onto an incident beam allowing for the spatial structuring of light.

desired field $U(x,y)$, one must apply a transmission function $T(x,y)$ onto some incident field $V(x,y)$.

$$U(x,y) = T(x,y)V(x,y)\,. \tag{2.3}$$

For simplicity we assume the incident field to be a plane wave $V = e^{i(\mathbf{k}\cdot\mathbf{r}-\omega t)}$. This is reasonably achievable using common expansion and collimation techniques. This allows us to focus solely on the profile of the output field $U(x,y)$. We want our complex amplitude modulation scheme to return a field with a chosen amplitude and phase profile

$$U(x,y) = A(x,y)e^{i\phi(x,y)}\,. \tag{2.4}$$

However, this is not trivial as the SLM is a refractive optical element and may only impart a phase factor onto the incident field. This phase must be function of the the desired amplitude and phase profile of our output field and so the transmission function must be of the form

$$T(x,y) = e^{iH(A,\phi)}\,, \tag{2.5}$$

where H is our hologram phase. We may expand $T(x,y)$ as a Fourier series

$$T(x,y) = \sum_{m=-\infty}^{\infty} c_m e^{im\phi}\,, \tag{2.6}$$

with

$$c_m = \frac{1}{2\pi}\int_{-\pi}^{\pi} e^{iH(A,\phi)}e^{-im\phi}\mathrm{d}\phi = \frac{1}{2\pi}\int_{-\pi}^{\pi} e^{iH(A,\phi)-im\phi}\mathrm{d}\phi\,. \tag{2.7}$$

We are able to control the order in which our desired field occurs by fixing one of the coefficients. We choose this to be the first order by setting $c_1 = \gamma A$ for some real, positive number γ. Expanding equation 2.7 using Euler's formula thus gives:

$$c_1 = \gamma A = \frac{1}{2\pi}\int_{-\pi}^{\pi}\cos(H(A,\phi)-n\phi)\mathrm{d}\phi + \frac{i}{2\pi}\int_{-\pi}^{\pi}\sin(H(A,\phi)-n\phi)\mathrm{d}\phi\,. \tag{2.8}$$

Since we insist that γ must be a real, positive number, the following two conditions must be met:

$$\int_{-\pi}^{\pi}\cos(H(A,\phi)-\phi)\mathrm{d}\phi = 2\pi\gamma A\,, \tag{2.9}$$

$$\int_{-\pi}^{\pi}\sin(H(A,\phi)-\phi)\mathrm{d}\phi = 0\,. \tag{2.10}$$

One such function that satisfies all the above conditions has the form:

$$H(A,\phi) = f(A)\sin(\phi)\,, \tag{2.11}$$

for some unknown function $f(A)$. This can be substituted back into equation 2.5 to obtain the following:

$$T(x,y) = e^{if(A)\sin(\phi)}\,. \tag{2.12}$$

We now have a more detailed expression but still do not know the exact form of the function $f(A)$. To find the form of this function, we may expand the transmission function again, but this time using the Jacobi-Anger identity. This identity allows us to express our transmission function as an infinite sum of Bessel functions of the first kind,

$$T(x,y) = \sum_{m=-\infty}^{\infty} J_m(f(A))e^{im\phi}\,. \tag{2.13}$$

This expression can be related back to the Fourier series expansion in equation 2.6 to show that the expansion coefficients are equal to the Bessel functions

$$c_m = J_m(f(A))\,, \tag{2.14}$$

and since we want our field to appear in the first order, we have:

$$\begin{aligned} c_1 &= J_1(f(A)), \\ \Rightarrow \gamma A &= J_1(f(A)), \\ \Rightarrow f(A) &= J_1^{-1}(\gamma A), \end{aligned} \tag{2.15}$$

where J_1^{-1} is the reciprocal of the first order Bessel function. Since γ can be any positive, real number, we will set it equal to 1 for convinience. The transmission function for the SLM is then:

$$H(A,\phi) = J_1^{-1}(A(x,y))\sin(\phi(x,y)). \tag{2.16}$$

An unfortunate practical limitation is that SLMs are not perfectly efficient and significant amount of light will not be modulated by the liquid crystals. Thus, the output beam will still not have the desired amplitude profile. This can be overcome by adding in a grating term to the hologram. This results in the modulated light also being diffracted into the first order, leaving most of the unmodulated light in the zeroth order. This concept is illustrated in Figure 2.2. Mathematically, this is expressed by assigning spatial frequencies G_x and G_y to the grating in the horizontal and vertical directions, respectively. The final hologram function will then have the form:

$$H(A,\phi) = J_1^{-1}(nA(x,y))\sin[\phi(x,y) + 2\pi(G_x x + G_y y)]. \tag{2.17}$$

The effect of the grating is shown through simulated images in Figure 2.2. Here, the hologram is illuminated not with a plane wave, but with a Gaussian beam with a beam waist twice the size of beam in the encoded hologram. This is done to more easily see the effects of the unmodulated light. The intensity profile of various experimentally generated HG beams and their holograms are shown in Figure 2.3, and experimentally generated LG beams and their holograms are shown in Figure 2.4.

2.2 Digital Micro-Mirror Devices

An alternative device to a liquid crystal SLM is a digital micro-mirror device (DMD). Such devices consist of an array of mirrors (typically on the scale of 3-4 μm) which may face in either an "on" or "off" or "parked" state. The "parked state occurs when no hologram is programmed on the DMD. The "on" and "off" states occur when a hologram is programmed and reflect light towards or away from the desired direction. Such a device is thus a diffractive optical element and requires a binary hologram, in contrast to the SLM's refractive properties and multi-levelled phase holograms. A diagram showing the structure and behaviour of the DMD's micro-mirrors is given in Figure 2.6. The angle of $\pm 12^\circ$ are fixed as part of the manufacturing of the DMD and have been chosen by the manufacturer to balance image contrast and quality with the thin films principles that allow for multiple bends on the hinge without significant wear and tear [5].

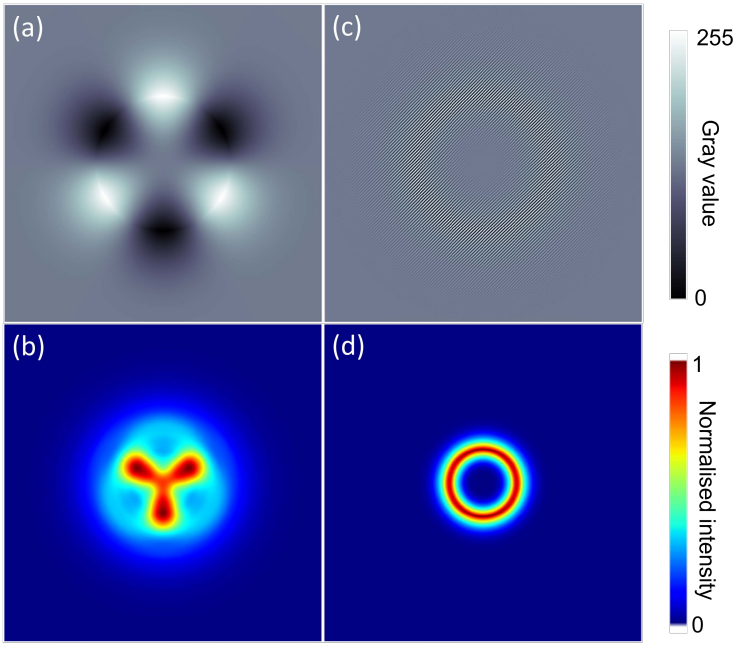


FIGURE 2.2: **Addition of a Phase Grating on the SLM Hologram.** The encoded SLM holograms (top row) and simulated intensity profiles (bottom row) of an LG_3^0 mode generated a)-b) with and c)-d) without the addition of a grating on the SLM hologram with a Gaussian beam incident on the SLM screen. The absence of a grating causes the unmodulated light to be mixed with the desired field, thus creating an undesirable beam profile. The addition of a grating separates out this unmodulated light leaving only the desired field.

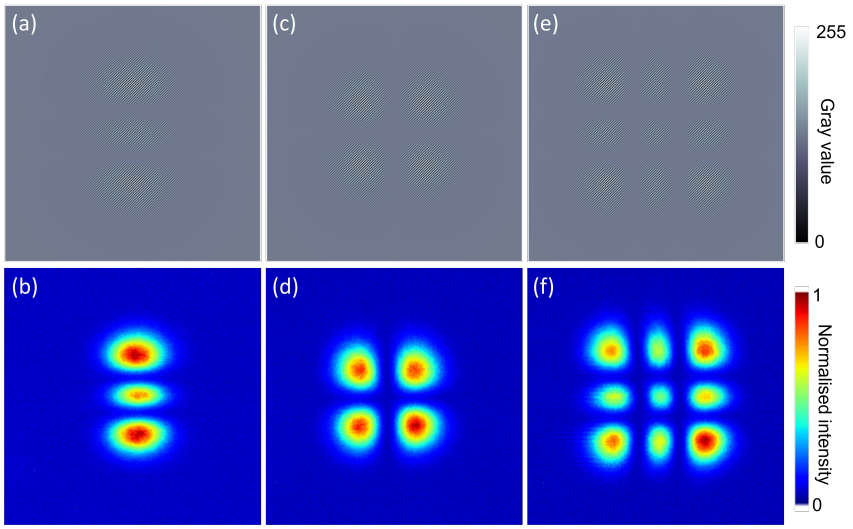


FIGURE 2.3: **Experimental Hermite-Gaussian Beams with an SLM.** The encoded SLM phase holograms (top row) and experimentally generated (bottom row) intensity profiles of various HG_n^m modes. The modes shown are a)-b) HG_0^2, c)-d) HG_1^1 and e)-f) HG_2^2.

DMDs have an efficiency of around 6% once a hologram is displayed, making them far more lossy than SLMs. However, they are significantly

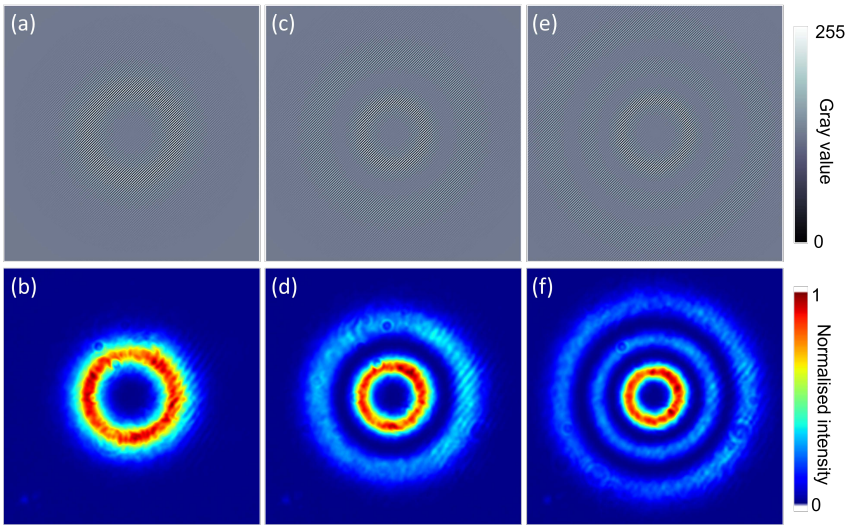


FIGURE 2.4: **Experimental Laguerre-Gaussian Beams with an SLM.** The encoded SLM phase holograms (top row) and experimentally generated (bottom row) intensity profiles of various LG_p^l modes. The modes shown are a)-b) LG_0^2, c)-d) LG_1^2 and e)-f) LG_2^3.

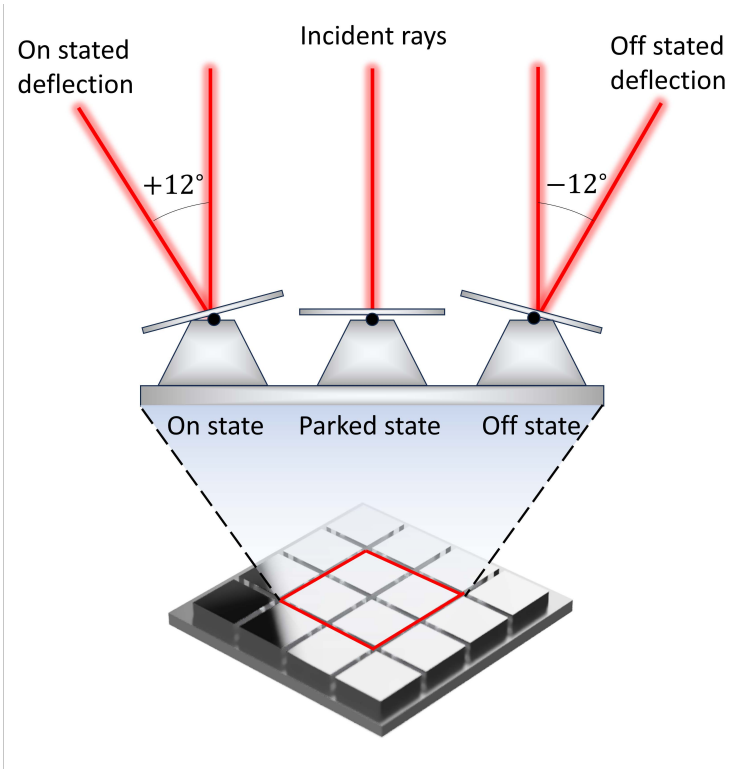


FIGURE 2.5: **DMD Micromirrors.** The mirrors of a DMD can be in three states: "on", "off" or parked. When not in use, the mirrors are in the parked state. When in the "on" or "off" state, the mirrors will deflect the incident beam by an angle of$\pm 12^\circ$ relative to the incident rays. The value of 12° is fixed and cannot be altered by the user of the device. It is standard in the manufacturing of the model of the DMD used.

cheaper and do not rely on birefringence to shape light, making them insensitive to polarisation and well suited for manipulating vectorial light fields.

2.2.1 Complex Amplitude with a Binary Hologram

As with the SLM, we shall assume an incident plane wave and aim to create a field with the chosen amplitude and phase profile,

$$U(x,y) = A(x,y)e^{i\phi(x,y)}\,. \tag{2.18}$$

For simplicity, we will express the transmission function of the DMD in 1-dimension as follows:

$$T(x) = \sum_{n=-\infty}^{\infty} \text{rect}\left(\frac{x-(n+p)x_0}{wx_0}\right)\,. \tag{2.19}$$

Here, the mirrors position, width and period are set by the parameters p, w and x_0 respectively and $\text{rect}(x)$ is that rectangle function defined as

$$\text{rect}(x) = \begin{cases} 1, & \text{for} |x| \leq \frac{1}{2} \\ 0, & \text{otherwise} \end{cases}\,. \tag{2.20}$$

As before, we expand the above as a Fourier series to obtain

$$T(x) = \sum_{n=-\infty}^{\infty} c_n e^{i2\pi n\frac{x}{x_0}}\,, \tag{2.21}$$

with

$$c_n = \int_{x_a}^{x_b} \text{rect}\left(\frac{x-px_0}{wx_0}\right) e^{-i2\pi\frac{x}{x_0}}\,\mathrm{d}x\,. \tag{2.22}$$

The limits of the integration are determined by the extent of the rectangle, where $n = 0$, and are thus given by

$$x_a = px_0 - \frac{1}{2}wx_0\,, \tag{2.23}$$

$$x_b = px_0 + \frac{1}{2}wx_0\,. \tag{2.24}$$

The expansion coefficients then become

$$c_n(p,w) = \int_{x_a}^{x_b} e^{-i2\pi n\frac{x}{x_0}} = \frac{1}{\pi n}e^{i2\pi np}\sin(\pi nw)\,. \tag{2.25}$$

We will choose our functions going forward so that our desired field $U(x,y)$ appears in the first order, thus demanding

$$c_1 = \frac{1}{\pi}e^{i2\pi p}\sin(\pi w) = Ae^{i\phi}\,. \tag{2.26}$$

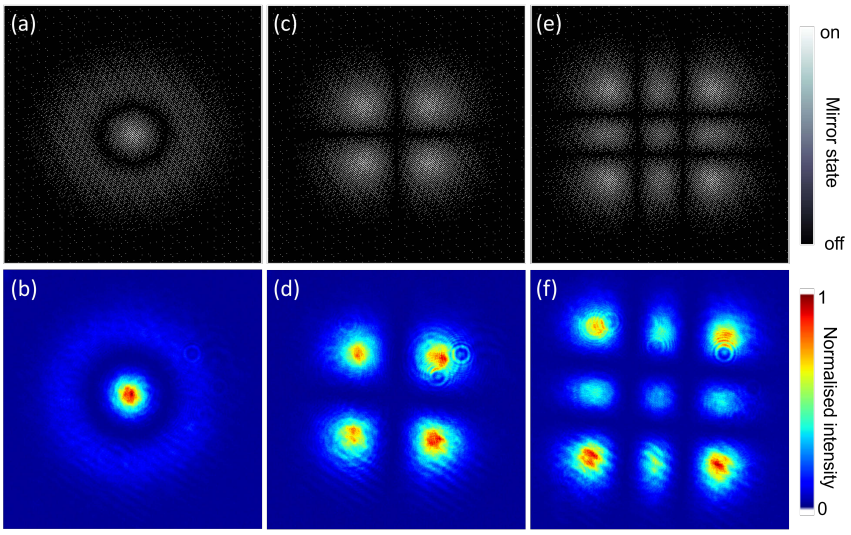


FIGURE 2.6: **Experimental LG and HG Beams with a DMD.** The encoded binary DMD amplitude holograms (top row) and experimentally generated intensity profiles (bottom row) of various spatial modes. The modes shown are a)-b) LG_1^0, c)-d) HG_1^1 and e)-f) HG_2^2. The beam profile might appear more pronounced in the encoded hologram as compared to the captured experimental intensities. This can be easily explained by observing that the hologram function does not depend on the square of the field while the intensity does, thus exaggerating certain features of the beam profile.

From this expression we can clearly distinguish the amplitude and phase terms to be

$$w(x,y) = \frac{1}{\pi}\arcsin[A(x.y)]p(x,y) = \frac{1}{\pi}\phi(x,y)\,. \tag{2.27}$$

Where we have extended our expressions into 2-dimensions. Substituting these expressions back into equation 2.19 returns:

$$\frac{1}{2} + \frac{1}{2}\text{sign}(\cos(\pi p(x,y)) - \cos(\pi w(x,y))\,. \tag{2.28}$$

As with the SLM we will also add in a diffraction grating in order to separate out the first order. The final expression for the DMD hologram is then

$$\frac{1}{2} + \frac{1}{2}\text{sign}(\cos\big(2\pi(G_x x + G_y y)\pi p(x,y)\big) - \cos(\pi w(x,y))\,. \tag{2.29}$$

It is important to note that DMDs have two diffraction processes occurring simultaneously due to the presence of two set of gratings. One is due to the programmed grating in the hologram and the other is due to the space between the micro-mirrors themselves, as they do not perfectly fill the space that they occupy. Images of experimentally generated HG and LG beams produced using a DMD, as well as the holograms used to generate them are given in Figure 2.6.

Chapter 3

Eigenmodes of the Tilted Lens

This chapter is based on the paper:

Wagner Tavares Buono, **Cade Ribeiro Peters**, Jacqueline Tau, Isaac Nape and Andrew Forbes, "Eigenmodes of aberrated systems: the tilted lens," (2022) Journal of Optics, Vol.24, 125602.

C. Peters derived the expressions for locating the conversion plane, performed several of the experiments, assisted with the data analysis and contributed to writing the manuscript.

We have now established the existence of transverse spatial modes of light which are solutions to the paraxial Helmholtz wave equation. They are able to propagate unchanged through a perfectly uniform medium with a constant refractive index and so are known as eigenmodes of free space. Besides this unique property of propagation invariance, the Laguerre Gaussian (LG) and Hermite Gaussian (HG) modes each form a complete set of linear and orthogonal spatial modes. This endows them with the same properties as a vector space if given the appropriate representation[6]. Similar representations in optics are given by polarisation such as the Poincaré sphere and Jones matrix formalism. However, the spatial mode representation can exist in even higher dimensions[7]. Such a property makes the modal description of optical field a versatile and advantageous tool for simplifying the description of many optical phenomena such a light propagation [8], forming convenient bases for measurements [9], manipulating laser beam size [10, 11] and tailoring spatial intensity profiles in propagation [12]. Because the HG and LG modes both form complete bases, it is possible to decompose an HG mode into the LG basis and vice versa. This allows for a convenient way to describe the phenomenon of mode conversion, which can be seen by either looking at the relationship between the respective polynomials that describe these modes [13] or by adopting a matrix formalism [14].

Structured light has proved to be an invaluable tool in both the classical[15] and quantum [16] regimes. However, one of the primary limitations in both regimes is the sensitivity of structured light beams to aberrations and distortions in the medium or system. Such a problem has led to the search for invariant modes of light in specific systems, the so-called eigenmodes of the system. Much progress has been made to this end with several cases showing

the ability to perform imaging with eigenmodes [17–19] and achieve super-resolution [20], while others have shown useful implementation in micro-cavities [21]. Despite these tremendously significant advancements, very little attention has been given to the implementation of popular mode families such the HG and LG modes [22].

This chapter will focus on an approach that takes advantage of the linear nature of optical systems to construct a matrix in the transverse spatial mode basis up to an arbitrary order. Once such a matrix is found, the eigenstates of this matrix can easily be determined using a number of well-known techniques. They can then be applied to the spatial mode basis to determine the invariant modes (eigenmodes) of the system. To demonstrate the effectiveness of this approach, we make use of a simple optical system: a tilted lens. Such a system was chosen due to its topical nature having found applications in mode sorting and its ability to detect the orbital angular momentum of light [23]. We see immediately from the operator obtained in this example that the invariant modes are the HG modes. We expand this set by using an often overlooked property of eigenvectors and eigenstates and then test these findings experimentally, showing the robustness of the HG modes and their superpositions. It is important to note that, even though we use a tilted lens as an example, the approach can be applied to any type of optical system provided sufficient knowledge of the aberration or perturbations is obtained.

3.1 Theory

3.1.1 The Tilted Lens

Purposefully astigmatic systems such as the tilted lens have seen a lot of research effort due them being a simple and effective OAM detector[24]. This is achieved through the mode conversion of LG modes into HG modes. The use of the tilted lens as a more compact version of earlier approaches which used a combination of cylindrical lenses to achieve the same mode-conversion effect [13, 25]. In general, these systems are called astigmatic mode converters and they provide and intriguing interface between both ray and wave optics [26, 27]. In the remainder of this section we will interchangeably refer to the tilted lens as an astigmatic mode converter. Works that have studied the propagation of LG modes through astigmatic systems include [28–31]. Ref [31] in particular noted that the vortices present in LG beams split to create intensity profiles similar to those of Ince Gaussian beams. Several properties of the mode conversion phenomenon between HG and LG modes have been observed and studied. These include the conservation of OAM [23] and the effects of geometric phase. This has led to further work using this technique for applications as an OAM and radial mode detector [32–35], and in vectorial light transformations respectively[36, 37]. The mode conversion can also be induced holographically [38] and has been combined with machine learning models [39] to further help identify the various superpositions of complex structured light fields.

In the literature, it is common to describe astigmatic mode converters in the HG basis [14, 24, 39], and so this basis will also be used in our investigation. We will denote a vector in our space as $|\Psi\rangle$, which is an arbitrary superposition of Hermite Gaussian modes between the zero and an arbitrary maximum mode order N_{max}, and is mathematically described by,

$$|\Psi\rangle = \sum_{j=0}^{N_{max}} \sum_{n=0}^{j} c_{j-n}^{n} \left| HG_{j-n}^{n} \right\rangle , \tag{3.1}$$

this can be projected into the position basis as follows,

$$\begin{aligned} \langle x, y | HG_{m}^{n} \rangle &= HG_{m}^{n}(x, y) \\ &= H_m(\tilde{x}) H_n(\tilde{y}) e^{ikz} e^{i\phi_{m,n}} e^{\frac{ik(x^2+y^2)}{2R(z)}} G(\tilde{x}, \tilde{y}), \end{aligned} \tag{3.2}$$

where $\tilde{x} = x/w(z), \tilde{y} = y/w(z)$, the Gouy phase is $\phi_{m,n} = (m+n+1)\arctan(z/z_R)$, $w(z) = w_0\sqrt{1+(z/z_R)^2}$ is the beam diameter for a beam waist w_0, $z_R = \pi w_0^2/\lambda$ is the Rayleigh length, $G(\tilde{x}, \tilde{y})$ is the Gaussian envelope, $H_m(x)$ is a Hermite polynomial of order m, and $R(z) = z\left[1+(z_R/z)^2\right]$ is the radius of curvature of the wavefront. The properties of the HG modes allow us to construct a basis which forms a complete vector space and thus it may used to describe the structure of any complex light field in the transverse plane. The modal decomposition given in Equation 3.1 gives the particular superposition of HG modes required, with the relevant normalised coefficients c_l^k to construct any arbitrary light field $|\Psi\rangle$. Knowledge of these coefficients allows for one to describe the propagation dynamics of the optical field using the modal propagation approach [8], which in turn allows us to easily describe the effect of the tilted lens on the incident beam.

Since we are using a matrix formalism to describe the action in our modal basis, and because the action of the astigmatic mode converter is linear, we may model the action of the tilted lens as a matrix operator $\mathcal{M}$ which will act on any vector in our modal space $|\Psi\rangle$ as follows,

$$\left|\Psi'\right\rangle = \mathcal{M} \left|\Psi\right\rangle . \tag{3.3}$$

If we have $|\Psi'\rangle = \lambda |\Psi\rangle$ where λ is some complex number, then $|\Psi'\rangle$ is known as an eigenstate or eigenvector of the operator $\mathcal{M}$. Due to the many similarities between the field of optics and the study of quantum mechanics, Dirac notation is commonly used [7], and will be used in this section to more compactly represent the operator approach we wish to implement. The benefits of using this operator notation is that it allows us to represent the action of multiple effects such as phase perturbations in the medium or system, diffraction caused by free space propagation, and scattering and absorption effects as a single mathematical operator. Typically, these would require their own transmission functions or integral transforms to be modelled accurately, but with the use of the modal basis and the operator approach, we can simplify all these effects into a single operator.

Using Ref [12], we may write the operator of the tilted lens in the HG modal basis as

$$\mathcal{M}_t = \sum_{o}^{N_{max}} \sum_{n=0}^{o} e^{\frac{i(o-2n)\pi}{4}} \left|HG^n_{o-n}\right\rangle \left\langle HG^n_{o-n}\right| . \tag{3.4}$$

The full action of this operator is as follows: a beam is propagated a distance f (where f is the focal length of the lens when it is not tilted), the application of the astigmatic phase by the tilted lens (which rotated by some small angle about the z axis), and then the subsequent propagation of the beam to the conversion plane denoted by a distance d. More details on the exact location and properties of the conversion plane are given in later sections. Another benefit of describing the operator $\mathcal{M}_t$ in the HG basis is that it makes it immediately clear that the HG modes themselves are eigenmodes of this operator. An interesting observation is that even though there are an infinite number of possible HG modes, the eigenvalues of these eigenstates are given by a complex exponential function. Since the indices of the HG modes are all discrete, positive integers, this results in only a finite number of possible eigenvalues for any given HG mode. This begs the question: can we glean some underlying structure or intuition about these eigenmodes by grouping the modes according to their eigenvalue? We must then make use of a seemingly underutilised property of eigenvectors: eigenvectors of the same operator with the same eigenvalue may be added together to form another eigenvector.

Our main takeaways so far are summarised in Figure 3.1. The tilted lens acts as an astigmatic mode converter and thus causes an LG beam to undergo mode conversion into an HG beam rotated by 45 degrees (top row). HG beams orientated along the tilted axis are eigenmodes of the tilted lens and thus will pass though unchanged (top centre row). A random superposition of HG modes, each with different eigenvalues under the operator $\mathcal{M}_t$, is not an eigenmode of the tilted lens, and will change at the output of the system (bottom centre row). A superposition of HG modes, each with the same eigenvalue is an eigenmode of the tilted lens and thus will exit the system with the same intensity profile as when it entered.

3.1.2 Conversion Plane

Location of the Conversion Plane

The location of the conversion plane must be determined to accurately capture the action of the operator in an experimental setting. In order to determine the exact plane in propagation where the conversion happens, we first need to define the criteria for conversion and how we are modelling the tilted lens as an optical element. We begin our analysis by closely following reference [13]. In the reference, the Gouy phase difference is the driving mechanism behind the conversion. The authors argue that an astigmatic beam can be separated in its $x(y)$ modal components, having different Gouy phases. The conversion would happen when the Gouy phase difference due to propagation is equal to $\pi/2$.

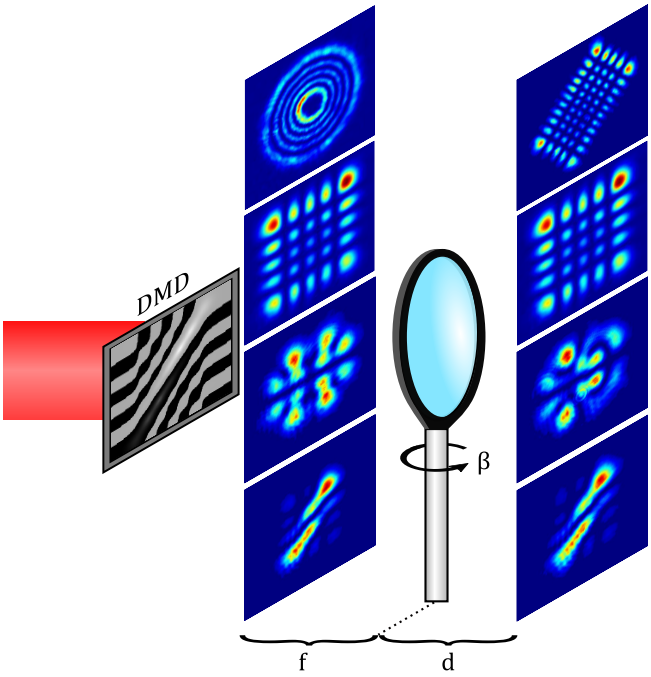


FIGURE 3.1: **Astigmatic Mode Conversion.** When a Laguerre-Gaussian passes through a tilted lens, it gets converted to an HG mode at a distance d from the lens (first row). This HG mode is aligned along the diagonal direction. When an HG modes passes through a tilted lens, it remains unchanged (second row). An arbitrary superposition of HG modes will in general not remain invariant when passing through the astigmatic system (third row). However, if we use several HG modes with the same eigenvalue to create a superposition of HG modes, this superposition will remain invariant (fourth row). This figure was adapted from reference [40] with consent from the authors.

We start then by the Gouy phase separation of the type

$$\phi_{m,n}(z) = (m+n+1)\psi(z) = \left(m+\frac{1}{2}\right)\psi_x(z) + \left(n+\frac{1}{2}\right)\psi_y(z), \tag{3.5}$$

where $\psi_{x(y)} = \arctan\left(\frac{z-z_{0x(y)}}{z_{Rx(y)}}\right)$ and $z_{0x(y)}$ is the distance between the lens and the waist plane of the beam in the $x(y)$ direction. Due to the astigmatic nature of the lens system, these values are not necessarily the equal nor are they necessarily equal to waist plane when the lens is untitled z_0 as the distortion of the lens moves the location of the waist plane differently in both the x and y directions. For a distance $z_{0x(y)}$ from the waist plane to the position where the lens is placed, we get a phase difference $\Delta\psi_{x(y)}$ as in

$$\Delta\psi_{x(y)}(D) = \arctan\left(\frac{D-z_{0x(y)}}{z_{Rx(y)}}\right) - \arctan\left(\frac{z_0-z_{0x(y)}}{z_{Rx(y)}}\right), \tag{3.6}$$

where D is some distance away from the lens. We then make use of the relation

$$\arctan(a) \pm \arctan(b) = \arctan\left(\frac{a \pm b}{1 \mp ab}\right), \tag{3.7}$$

and get

$$\Delta\psi_{x(y)}(D) = \arctan\left(\frac{Dz_{Rx(y)} - z_{Rx(y)}z_{0x(y)}}{z_{Rx(y)}^2 + Dz_0 - Dz_{0x(y)} - z_0 z_{Rx(y)} + z_{0x(y)}^2}\right). \tag{3.8}$$

While Equation 3.8 is the accumulated phase due to propagation for each Cartesian coordinate x/y, they can accumulate different phases by having different $z_{Rx(y)}$. This can be caused by a cylindrical lens, a rotated lens or a general astigmatism. Therefore, by accumulating different phases, the phase difference at any given plane is given by:

$$\theta = \Delta\psi_x - \Delta\psi_y\,. \tag{3.9}$$

We may subtract these two terms as is as we are finding the resulting relative intramodal phase in the beam due to two separate effects in two orthogonal directions. One effects it's the distortion in the y direction and the other is the distortion in the x direction. This has been clarified in the text.

Notably, this relative phase does not depend on the mode order. By combining Equations 3.8 and 3.9 and making use of relation Equation 3.7 we then see that

$$\theta = \arctan\left(\frac{q_y Dz_{Rx} - q_x Dz_{Ry}}{q_x q_y + D^2 z_{Rx} z_{Ry}}\right), \tag{3.10}$$

where

$$q_{x(y)} = z_{Rx(y)}^2 - Dz_{0x(y)} + z_{0x(y)}^2\,, \tag{3.11}$$

$$z_{0x(y)} = \frac{f_{x(y)}^2(z_0 - f_{x(y)})}{(z_0 - f_{x(y)})^2 + z_R^2} + f_{x(y)}\,, \tag{3.12}$$

$$z_{Rx(y)} = \frac{z_R f_{x(y)}^2}{(z_0 - f_{x(y)})^2 + z_R^2}\,. \tag{3.13}$$

Since we are looking for solutions of the type $\theta = \pi/2$, we want the argument of arctan to tend to infinity. This would be simply achieved by solving for the denominator to be zero in Equation 3.10. By defining the quantities f_x and f_y as the focal length of the astigmatic lens in the x and y directions respectively, we can then solve this equation.

Transmission function

We model the tilted lens as a regular transmission function of a thin lens $T = e^{-i\pi\left(\frac{x^2}{\lambda f_x} + \frac{y^2}{\lambda f_y}\right)}$, which has a different focal length for x and y. They take the form of $f_y = f$ and $f_x = f\cos^2\beta$, where β is the angle of rotation of the

lens around the z-axis. The relative phase becomes:

$$\theta(D,\beta) = \tan^{-1}\left(\frac{\theta_a}{\theta_b+\theta_c}\right), \tag{3.14}$$

$$\theta_a = D^2 f z_R \sin^2(\beta), \tag{3.15}$$

$$\theta_b = D\left(D\left(-fz_0+z_0^2+z_R^2\right)-f\left(z_0^2+z_R^2\right)\right), \tag{3.16}$$

$$\theta_c = f\cos^2(\beta)\left((D+z_0)(D(f-z_0)+fz_0)+z_R^2(f-D)\right). \tag{3.17}$$

We can then calculate the conversion distances d by setting $\theta(d,\beta) = \pi/2$. An $\arctan(x)$ function, tends to $\pi/2$ when its argument goes to infinity. Since the numerator is a simple well behaved function, we look for solutions where $\theta_b + \theta_c \to 0$. Solving this system, with the help of Mathematica, gives the solution for the conversion plane

$$d = \frac{d_a \pm d_b}{d_c}, \tag{3.18a}$$

where

$$d_a = f z_t^2\left(\cos^2(\beta)\left(z_t^2-2fz_0\right)+z_t^2\right), \tag{3.18b}$$

$$d_b = -\eta\left(f^2\cos^4(\beta)\left((f-z_0)^2+z_R^2\right)-2fz_0\cos^2(\beta)\left(f^2-2fz_0+z_t^2\right)\right.$$
$$\left.+z_t^2\left((f-z_0)^2+z_R^2\right)\right) \tag{3.18c}$$

$$d_c = 2z_t^2\left(f\cos^2(\beta)(f-z_0)-fz_0+z_t^2\right). \tag{3.18d}$$

We define z_0 being the distance between the waist plane of the beam and the lens, $z_t^2 = z_0^2 + z_R^2$ and

$$\eta = \sqrt{\frac{f^2 z_t^4\left(\cos^4(\beta)\left(z_R(z_R-2f)+z_0^2\right)\left(z_R(2f+z_R)+z_0^2\right)-2z_t^4\cos^2(\beta)+z_t^4\right)}{\left((f-z_0)^2+z_R^2\right)^2\left(f^2\cos^4(\beta)-2fz_0\cos^2(\beta)+z_t^2\right)^2}}. \tag{3.19}$$

While d has square roots in its formulation, given by η, the terms inside it can lead to negative values resulting in imaginary quantities. We interpret this as the conversion not happening in any plane for that given combination of tilting angle, beam waist and z_0. Therefore, by restraining η to real values we obtain a condition for the conversion to happen, being:

$$|\beta| > \arccos\left(\frac{\sqrt{z_0^2+z_R^2}}{\sqrt{2fz_R+z_0^2+z_R^2}}\right). \tag{3.20}$$

This expression was again obtained with the help of Mathematica. Before it was used though, two step were taken to simplify the computation. First, because we wish to restrict η to real values, we restrict the argument of the square root in Equation 3.19 to be positive. This then also has the convenient

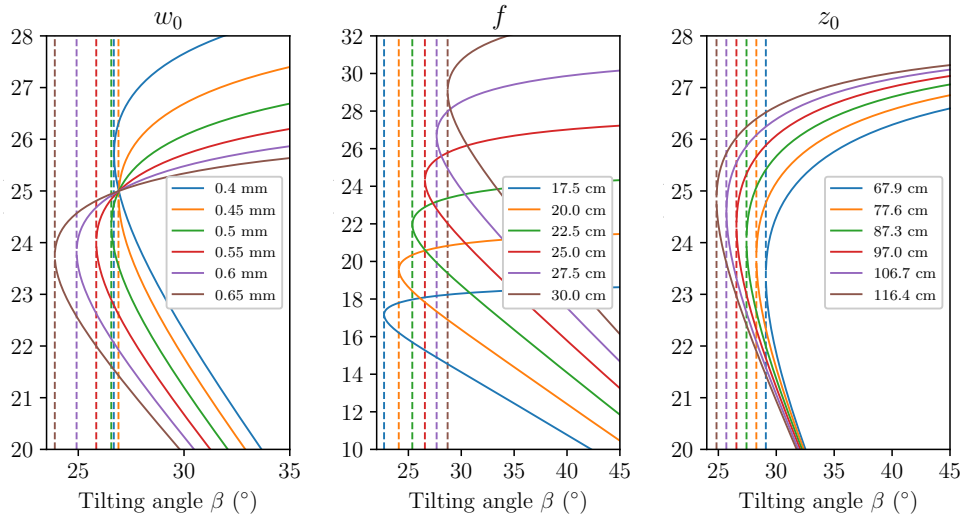


FIGURE 3.2: **Location of the Conversion Plane.**Conversion plane distance from tilted lens as a functions of various beams parameters. Unless specified, the parameters used were $z_0 = 97$ cm, $f = 25$ cm and $w_0 = 0.5$ mm. The units of the vertical axis are centimetres (cm) for all thee plots.

result of restricting the numerator only to be positive. This was the inputted into Mathematica to obtain Equation 3.20. In Figure 3.2 we show how the conversion plane changes for various parameters. The change with beam waist seems to be the most dramatic, having a big influence not only on the minimum angle but on how fast the conversion plane deviates from the focal length as the lens is tilted. For example, the minimum tilting angle changes on the order of degrees while the beam waist has only change on the order of a millimetres. The same effect on the tilting angle by changing the focal length or z_0 requires changing either on the order of centimetres. The focal length can have a squeezing/stretching effect on the distance. The beam waist also has a similar effect where the curvature of plot changes drastically as the beam waist itself changes. The focal length also has a big influence on the distance associated with the minimum conversion angle, where it appears to be always close to the focal length of the lens. In other words, the slope of the plot changes significantly with small changes in focal length.
The initial distance z_0 appears to have a linear relation with the minimum tilting angle. This linear relation however, is due to the small variation of this parameter relative to the Rayleigh length. In Figure 3.3 we show the minimum angle from Equation **??** as a function of beam waist and distance z_0. In this case, the same $f = 25$ cm value was used but z_0 was set from 0 to about the Rayleigh length $z_r = 1.2$ m. From this graphic we see that, for $z_0 = 0$, the minimum angle only decreases with the waist parameter. With our general model we were able to see that this is not true as z_0 increases. For small beam waists however, we see relatively rapid change in the minimum tilting angle as we vary z_0. The function is asymmetric due to the asymmetry of the arctan function over the positive real line. The Guoy phase in the x and y directions evolve differently as discussed previously in this chapter.

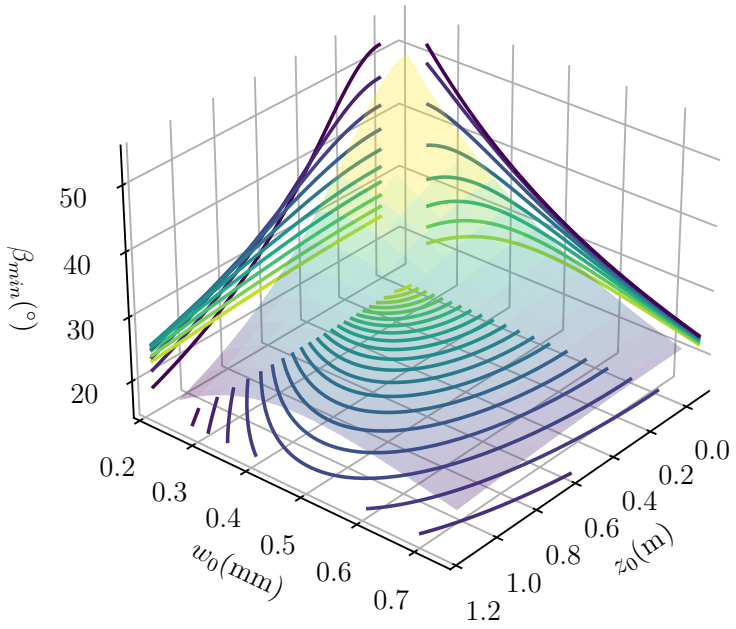


FIGURE 3.3: **Minimum Conversion Angle.**Minimum conversion angle as a function of w_0 and z_0 for $f = 25$ cm.

Because the arctan function grows rapidly close to the origin and then trails off asymptotically to π, the build up to a phase difference of $\pi/2$ for mode conversion is very fast over the propagation distance but the return to phase difference of zero only occurs again in the far field.

Experimental Comparison

To confirm the validity of our approach, we compared the theory predictions with experimental observations. The predicted and measured distances can be seen on the left in Figure 3.4. Blue dashed lines mark the two conversion distances for each angle and experimentally measured points are marked by black squares. The error bars were calculated by subtracting the maximum and minimum distances where the conversion happens (Δz) and dividing by two, whereas the central points are marked by the best mode quality. The dashed black line marks the minimum angle for conversion, calculated to be 26.55°. The distance for this minimum angle was calculated to be 24.34 cm.

The input mode used was a Laguerre-Gaussian beam with $p = 2$ and $l = -2$, being converted into a Hermite-Gaussian oriented at $-45°$ having $n = 2$ and $m = 4$. On the right-hand side of Figure 3.4, we show an example of how the errorbars were obtained. The average of the obtained distances was used as the length of the errorbar.

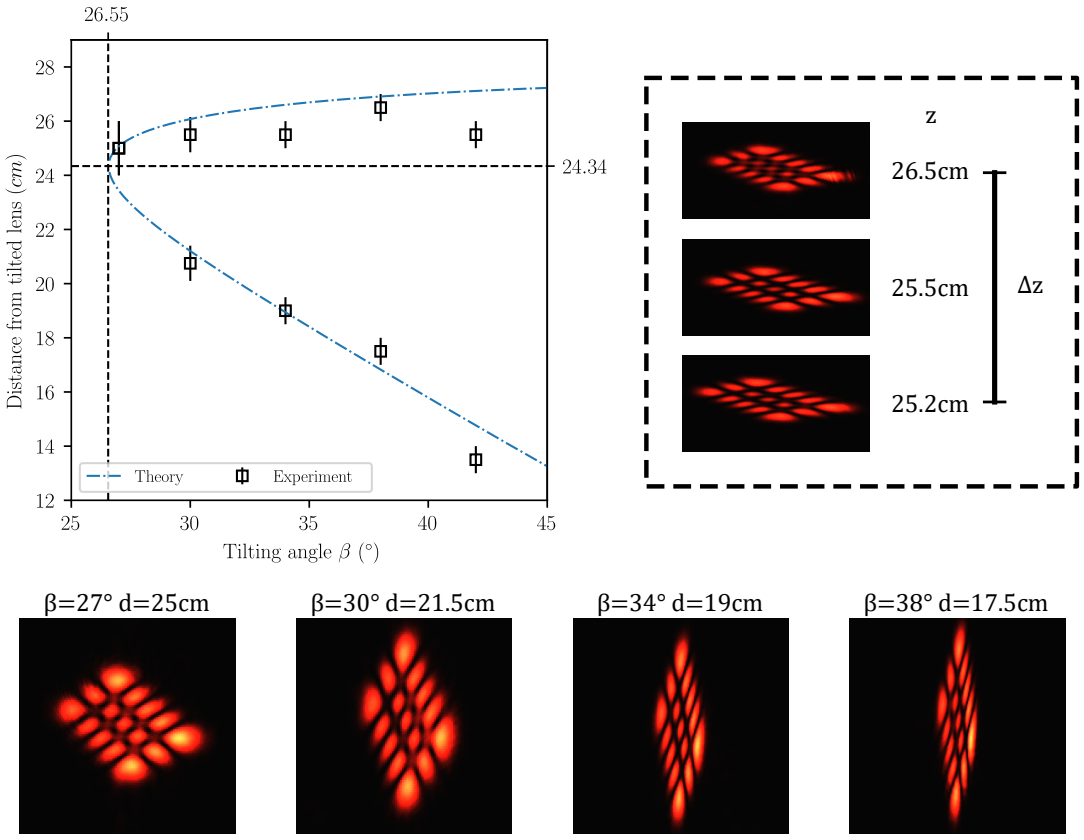


FIGURE 3.4: **Conversion Points.** Dashed blue lines represent theoretical predictions while squares with errorbars represent experimental points. The parameters used were $w_0 = 0.5$ mm, $z_0 = 91$ cm and $f = 25$ cm.

The experimental data obtained agrees well with the theoretical predictions. We observe that the best conversion obtained was always close to the minimum conversion angle. When the tilting angle is increased, a stretching effect can be observed in both conversion planes, but in different directions. An example of this is the bottom row of Figure 3.4. A Hermite-Gaussian pattern can clearly be seen, but as the angle increases it gets stretched in the y direction. This is due to the difference of diameter in each Cartesian component of the field. The tolerance for finding the conversion plane decreases as the angle increases, as we see a bigger variation of the mode with propagation distance.

3.1.3 Sorting Modes by their Eigenvalues

From Equation 3.4, we see that the eigenvalue for any given HG mode can be determined from its indices. Both indices for the HG function must be non-negative integers and since they are plugged into an exponential function whose argument is always divided by a factor 4, resulting in 8 possible eigenvalues. To make this sorting easier, we define $m - n = j \in \{0, 7\}$ such that the $j - th$ eigenvalue is given by $\lambda_j = e^{\frac{ij\pi}{4}}$.

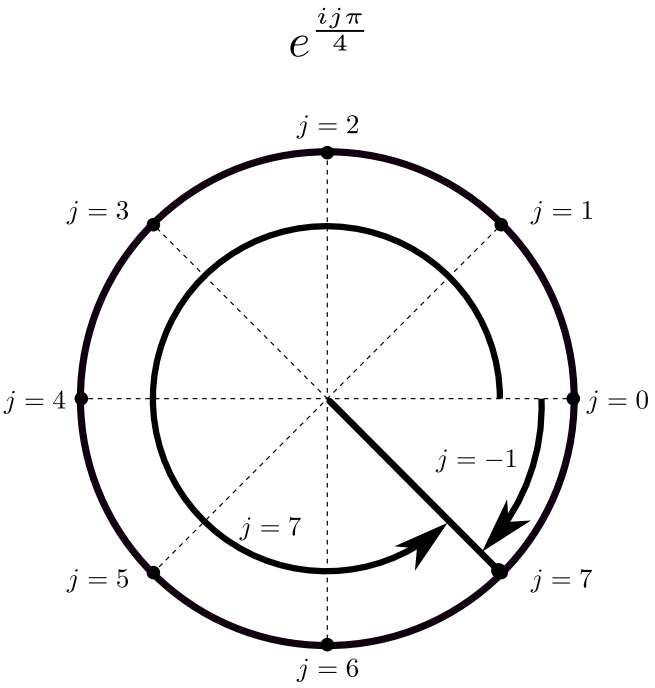


FIGURE 3.5: **Eigenvalue Mapping.** Eigenvalues with indices outside the range $j \in [0, 1, 2, 3, 4, 5, 6, 7]$ can be mapped to ones inside this range using the periodic nature of the exponential function. This figure was adapted from reference [40] with consent from the authors.

Since n and m need not be ordered, it is possible for j to take on positive or negative value. It is also possible for the value of j to lie outside the range of $j \in \{0, 7\}$. Both of these issues are taken care of by the periodic nature

of a complex exponential function with an integer index variable. We may use simple modular arithmetic to map any eigenvalues outside of this range back to one inside this range. We may use the modulo 8 convention which gives $j = 8\alpha + j'$, where j' is the eigenvalue outside of our defined range and α is some integer. For example, the value for $j' = -2$ would return the same value as $j = 6$ and if $j = 14$, we could map this to same eigenvalue for $j = 6$. We may use this to then define equivalence classes for our eigenmodes based on their eigenvalue:

$$[j] = \{\forall\, m, n \in \mathbb{W} \mid (m - n) \equiv j \,(\text{mod } 8)\} \tag{3.21}$$

with the equivalence modulo 8 being denoted by $a \equiv b(\text{mod } 8)$ [41] and $\mathbb{W}$ is the set of non-negative integers including zero (also called whole numbers [42]). When analysing the grouping created by this equivalent class, we make some interesting observations:

- The indices of the HG modes in each of the classes are not symmetric (i.e. $n \neq m$) except for $[0]$.
- For most classes, if one switches the indices of an HG mode, the new mode is in a different equivalence class. The only time the new mode is in the same equivalence class is for the modes in $[0]$ and $[4]$.
- If one looks at the classes $[j]$ and $[-j]$, one would see the same intensity patterns except rotated by 90° on the about the z axis. This creates a direct relationship between the class $[3]$ and the class $[5]$ for example.

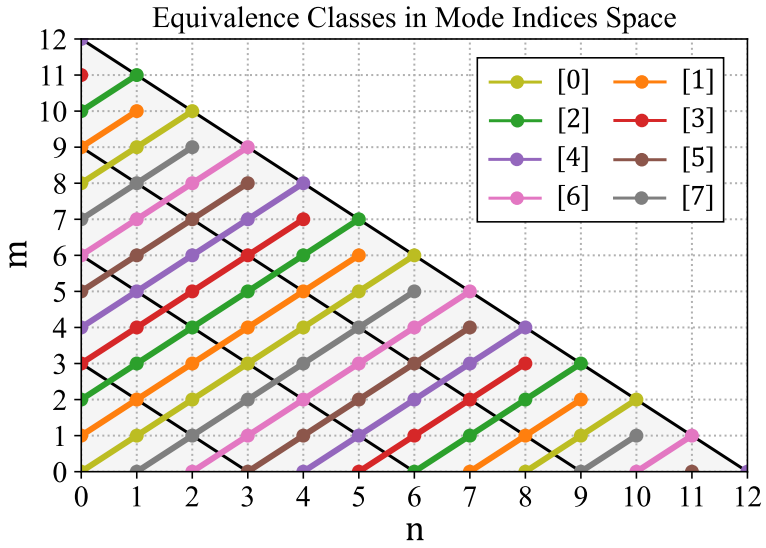


FIGURE 3.6: **Equivalence Classes.** We use different coloured diagonal lines to show the grouping of HG modes with their indices according to their equivalence class $[j]$ from equation 3.21. Black antidiagonal lines enclose regions with maximum mode order $N_{max} = 3, 6, 9, 12$. This figure was adapted from reference [40] with consent from the authors.

To visually show the relationship between the eigenvalues, we use Figure 3.6. The HG mode indices n and m are used as the x and y axes respectively,

such that each point on the grid represents a particular HG mode. The maximum mode order N_{max} is then set and shown as a black antidiagonal line. All the modes we wish to consider are shown in the grey shaded region underneath this black line. Each colour then represents an equivalence class $[j]$, and the use of coloured lines are included to connected HG modes with the same eigenvalue.

3.1.4 Generalisation of Eigenvectors

As discussed previously, we can superimpose two or more eigenvectors with the same eigenvalue to form another eigenvector. These will be referred to as auxiliary eigenvectors and we can write them as,

$$\begin{aligned} |\Psi\rangle_j = &\sum_{n=0}^{\lfloor \frac{N_{max}-j}{2} \rfloor} \sum_{\alpha=0}^{\lfloor \frac{N_{max}-j-2n}{8} \rfloor} c_{8\alpha+j+n}^{n} \left| HG_{8\alpha+j+n}^{n} \right\rangle \\ &+ \sum_{n=0}^{\lfloor \frac{N_{max}+j}{2} \rfloor} \sum_{\alpha=1}^{\lfloor \frac{N_{max}+j-2n}{8} \rfloor} c_{n}^{8\alpha+n-j} \left| HG_{n}^{8\alpha+n-j} \right\rangle \end{aligned} \tag{3.22}$$

Here $|\Psi\rangle_j$ represents the auxiliary eigenvector formed by a linear combination of regular eigenvectors of the same eigenvalue λ_j. The maximum mode order is given by N. The notation $\lfloor \circ \rfloor$ indicates the floor function ensuring that the indices of the summation are always integers. The summation can in theory be infinite, but we stop at some maximum mode order as properties such as beam size are limited by the aperture of a real-world optical system. It also allows us to have an idea of the beam size and the behaviour of the mode in propagation [10, 11]. This is most easily seen by looking at the mode with the highest and lowest mode orders in the superposition. Since the Gouy phase depends on the mode order $\phi_{m,n}(z) = (n+m+1)\psi(z)$, the mode with the highest mode order will control how rapidly the intensity distribution varies with z. Conversely, the mode with the lowest mode order will take the longest to reach the asymptotic limit of the Gouy phase and thus control how quickly the intensity distribution converges to its far-field pattern.

Given a single equivalence class $[j]$, if more than one mode is included, there is an infinite number of possible superpositions to be considered, since all c_m^n coefficients are continuous complex variables. Of course, the more HG modes are included in this summation, the more the intensity patterns will differ from each other. For simplicity, we will set all coefficients $c_m^n = 1$ since the resilient character of the modes is independent of an initial phase and relative non-zero weights. Since the auxiliary eigenvectors are composed of orthogonal modes and each mode can only be associated with a single auxiliary eigenvector, they are also orthogonal among themselves, regardless of the choice of relative weights and/or phases. The Table 3.1 explicitly summarises the superpositions used in this work, with corresponding equivalence classes and eigenvalues up until $N_{max} = 6$. The normalisation factor

[j]	Eigenvalue	Mode Superposition
[0]	1	$\left\|HG_3^3\right\rangle + \left\|HG_2^2\right\rangle + \left\|HG_1^1\right\rangle + \left\|HG_0^0\right\rangle$
[1]	$\sqrt[4]{-1}$	$\left\|HG_3^2\right\rangle + \left\|HG_2^1\right\rangle + \left\|HG_1^0\right\rangle$
[2]	i	$\left\|HG_0^6\right\rangle + \left\|HG_4^2\right\rangle + \left\|HG_3^1\right\rangle + \left\|HG_2^0\right\rangle$
[3]	$(-1)^{3/4}$	$\left\|HG_0^5\right\rangle + \left\|HG_4^1\right\rangle + \left\|HG_3^0\right\rangle$
[4]	-1	$\left\|HG_1^5\right\rangle + \left\|HG_5^1\right\rangle + \left\|HG_4^0\right\rangle + \left\|HG_0^4\right\rangle$
[5]	$-\sqrt[4]{-1}$	$\left\|HG_1^4\right\rangle + \left\|HG_5^0\right\rangle + \left\|HG_0^3\right\rangle$
[6]	$-i$	$\left\|HG_2^4\right\rangle + \left\|HG_6^0\right\rangle + \left\|HG_1^3\right\rangle + \left\|HG_0^2\right\rangle$
[7]	$-(-1)^{3/4}$	$\left\|HG_2^3\right\rangle + \left\|HG_1^2\right\rangle + \left\|HG_0^1\right\rangle$

TABLE 3.1: **Equivalence Class Superpositions.** Table showing the equivalence class, its respective eigenvalue and relevant HG mode superposition. The weighting coefficients in the superposition are all set to 1 and the maximum mode order considered is $N_{max} = 6$.

was omitted.

From the above discussion, it is clear that there are an infinite number of HG modes in each equivalence class $[j]$. Additionally, since the weighting coefficients c_m^n in Equation 3.22 are both continuous and complex, there are also an infinite number of possible superpositions for a given finite set of modes within the same equivalence class. Such cases will all result in differing intensity distributions both in the waist plane and in propagation. To simplify our investigation of these modes, we will choose to set each of the coefficients in any superposition to $c_m^n = 1$. The specific superpositions we will analyse in this section are given in Table 3.1 with the appropriate equivalence class and eigenvalue. We will consider superpositions up to maximum mode order of $N_{max} = 6$.

3.2 Experimental Setup

To test the generation of the eigenmodes, a 633 nm HeNe laser was expanded using a 10x times objective lens and then passed through a second lens ($f =$ 250 mm) for collimation. This expanded beam was then impinged onto a digital micromirror-device (DMD). The modes were generated by encoding binary holograms onto the DMD [43, 44]. The encoded beam waist for all the superpositions was $w_0 = 0.75$ mm. Before we can test the robustness of the modes, we need to ensure that the binary holograms are indeed generating the correct HG superpositions. This was done by constructing a 4f imaging system using a single lens. This is shown schematically in Figure 3.7 A and involves placing a lens of focal length f a distance $2f$ away from the the DMD and then placing the CCD camera a distance $2f$ from the lens. This should

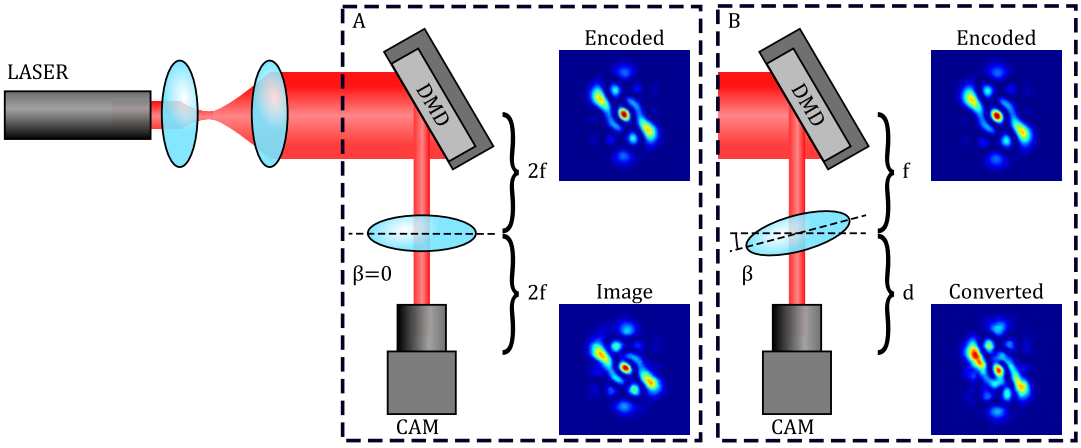


FIGURE 3.7: **Experimental Setup.** The experiment consists of a mode generation step and an optical imaging step. For mode generation, a laser beam is expanded and collimated so that it impinges on and overfills the screen of a DMD. The imaging step changes depending on what is being measured. In situation A, a 4f imaging system is constructed with a single lens to exactly image the prepared mode onto the camera. In situation B, the lens is placed one focal length away from the DMD.
This figure was adapted from reference [40] with consent from the authors.

perfectly image the generated modes from the hologram onto the plane of the sensor. The exact focal length of the lens used was $f = 300$ mm.

Since the action of the operator we have described previously is only valid in a single plane after the tilted lens, the setup must then be adjusted to test the robustness of the eigenmodes. To this end the distance between the DMD and the $f = 300$ mm lens was adjusted so that it was just a single focal length away of from the DMD. This is shown schematically in 3.7 B. This setup is constitutes a $2f$ imaging systems which allows one to see the far field distribution of the encoded field. To confirm that the setup was working as intended, a binary hologram for a Laguerre Gaussian (LG) beam was encoded onto the DMD and the camera was place one focal length away from the lens. An LG beam was chosen as its near field and far field intensity distributions are nearly identical allowing for an easy confirmation of the correct plane. Once this was this was done, the camera was moved to a precalculated distance $d = 279$ mm, the distance at which the conversion plane for the tilted lens was determined to be in the previous sections. The lens was then tilted by an angle of approximately $\beta \approx 24°$. The the tilting of the lens also slightly deflects the propagation direction of the beam and so this had be compensated for in the positioning of the camera. We then encoded binary holograms of the superpositions given in Table 3.1.

3.2.1 Propagation

Before we look at the robustness, it is worth considering the propagation dynamics of a superposition of HG modes and how these relate to the operator describing the effect of the tilted lens system. The operator for the tilted lens as used above describes three different actions as seen in Figure 3.1,

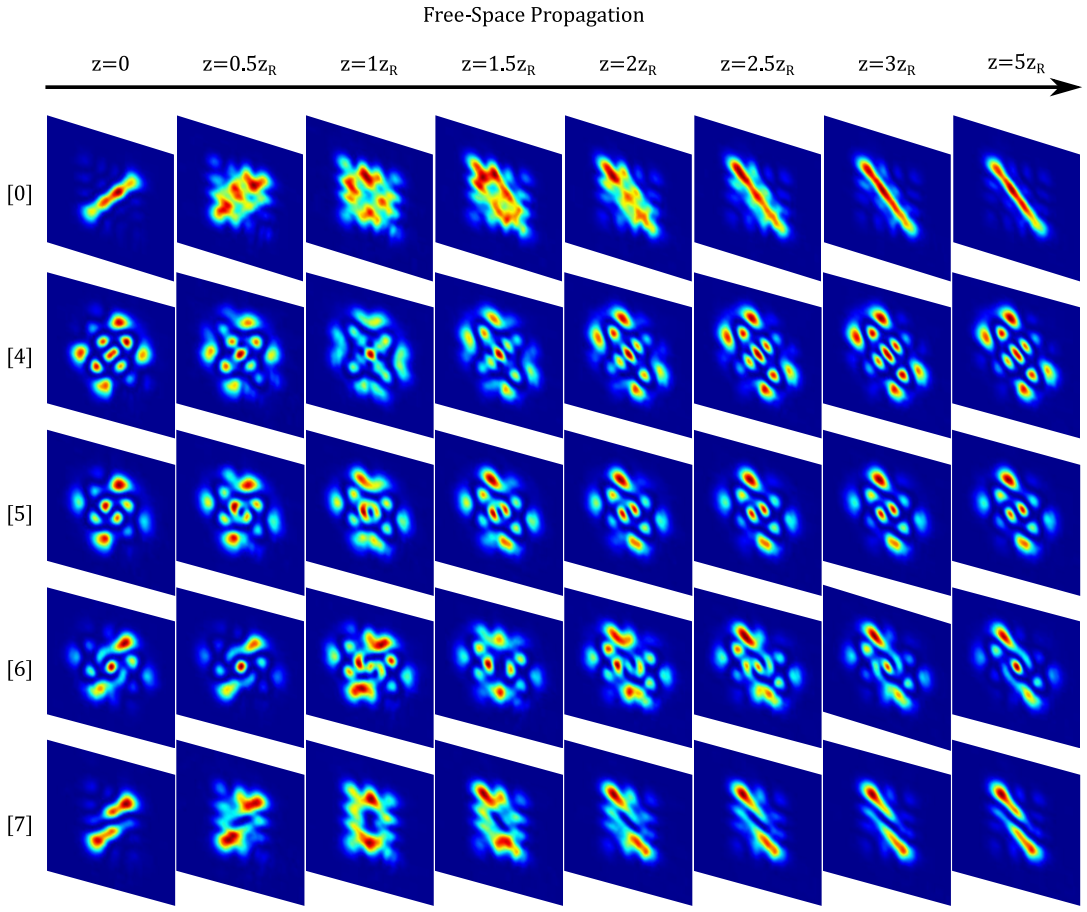


FIGURE 3.8: **Eigenmodes in Propagation.** The propagation of various auxiliary eigenmodes through free space. The modes considered here had a maximum mode order of $N_{max} = 6$. This figure was adapted from reference [40] with consent from the authors.

1. Propagation from the initial plane to the tilted lens,
2. Application of the astigmatic phase from the tilted lens,
3. Propagation from the tilted lens to the conversion plane.

The operator itself cannot only consider the astigmatic phase of the lens but must also take into account propagation before and after the lens. To see why, we must examine the propagation dynamics of a single HG mode. It is an eigenmode of free space and changes in two ways during propagation, both of which are predicted by its functional form. Firstly, the transverse area of the beam will increase due to the divergence of the laser beam. This is typical for all HG and LG modes and the divergence occurs at the same rate for all HG beams of the same beam waist w_0. This does not have a significant effect on the phenomenon we wish to study. Secondly, the beam will pick up phase according to the Gouy phase factor. Since this is simply a uniform phase across the entire transverse plane of the beam, it does not affect the intensity distribution of a single mode. However, the situation becomes little more complex when one considers a superposition of modes. The Gouy phase factor is proportional to the mode order and so two HG beams with different mode orders will gain Gouy phase at different rates. If superimposed, this change in relative phase means that the interference pattern between the two modes will also change in propagation. If we wish to send a single HG mode or a superposition of HG modes with the same mode order, the propagation before and after the lens is irrelevant. However, if we wish to send a superposition of modes of differing mode order (as is the case with the auxiliary eigenvectors), the propagation before and after the lens may significantly alter the spatial profile of the beam and thus must be considered when modelling the tilted lens system. There are two additional interesting consequences of the accumulation of the Gouy phase by HG superpositions of varying mode order. The first is a consequence of the fact that the accumulation of Gouy phase is simply the build up of an intra-modal phase between the component HG modes. Thus, as an auxiliary eigenmode propagates, it constitutes a new superposition in each and every subsequent plane. These new superpositions are all also auxiliary eigenmodes, each with a new combination of relative phases in the superposition. The second is that in the far-field, the Gouy phase accumulated by each mode of every mode order tends to the same value of $\pi/2$. Thus, in the far field, the spatial profile of the auxiliary eigenvector is that of itself flipped or mirrored across the y axis. This can be seen experimentally in Figure 3.8.

In order to account for the effects of propagation on the auxiliary eigenvectors, we employed two different methods. The first method made use of the angular spectrum and digital propagation techniques demonstrated in Ref [45]. Here, a lens function is applied to the hologram of the mode in order to move the Fourier plane. The second approach takes advantage of the paraxial nature of the HG modes. Because the modes are paraxial, we may choose an appropriate beam waist w_0 such that the divergence of the beam is negligible over the length scale used in the experiment. As such, the only

significant effect is that of propagation which can be replicated by appropriately adjusted the hologram on the DMD such that the field produced by the DMD will in turn produce our desired field after its has propagated through the tilted lens system. Both approaches showed identical results when observing their effects in the conversion plane.

To further substantiate this, we may turn to Ref [24], where it is shown that the astigmatic phase of the system is applied to the mode only when it reaches the tilted lens. A single HG mode will not change significantly in propagation and so will be almost identical at the initial plane and at the plane where it reaches the tilted lens. This is in contrast to superpositions of HG modes with varying mode order, where the field changes substantially when propagating at the same length scales.

The two techniques employed to compensate for the propagation are thus equally valid. However, it is important to note some limitations. The first method discussed is able to faithfully produce the spatial profile in the both the near field and at the conversion plane but has much stricter limitations placed on the distance it can compensate for. The method employs the angular spectrum method and so the applied phase in the frequency domain can only vary as much as the pixel size of the SLM allows and as slowly as the size of the SLM screen allows, therefore placing bounds on the propagation distance it can propagate for. The second method cannot produce both planes as the near-field spatial profile differs from the conversion plane spatial profile. It is however, relative to the first method, unlimited in the range of propagation distances it can compensate for.

To further investigate this observation, we can alter the experimental setup so that we use a digital hologram to apply the astigmatic phase. We do this by moving the lens to an untilted position ($\beta = 0^\circ$) and subsequently applying the Zernike polynomial associated with vertical/horizontal astigmatism, commonly denoted by Z_2^2. This allows us to examine the evolution of the mode solely under the influence of the astigmatism. The lens is one focal length f away from the screen of the DMD and, if we place the camera one focal length f after the lens, we are able to observe the far-field of the encoded field on the DMD. This configuration replicates a system in which the input field *does not* propagate before reaching the tilted lens but simply gains the astigmatic phase and then propagates to the far-field.

3.3 Results

We first wish to test the robustness of the auxiliary eigenmodes through the tilted lens system. The results of this are shown in Figure 3.9. The first column shows simulated intensity profiles of the various auxiliary eigenmodes. The second column shows the generated modes at the focal point of the lens with the lens untilted corresponding to configuration A of Figure 3.7. The final column shows the modes at the conversion plane of the lens when it is tilted corresponding to configuration B of Figure 3.7. From these images we see that the intensity of the calculated auxiliary eigenmodes remain almost

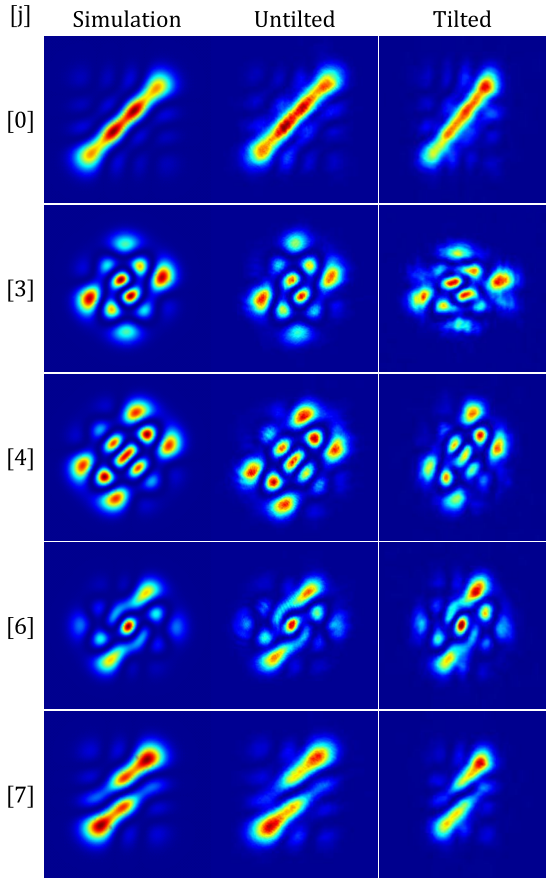


FIGURE 3.9: **Robust Eigenmodes of the Tilted Lens.** Experimental images showing the auxiliary eigenmodes at the focal point of an untilted lens (Untilted) and at the conversion plane of a tilted lens (Tilted). The modes are grouped by the equivalence classes$[j]$ and have a maximum mode order $N_{max} = 6$. First column shows theoretical simulations of the intensity profile (Simulation). This figure was adapted from reference [40] with consent from the authors.

unchanged at the conversion plane of the tilted lens. In these results, the maximum mode order was $N_{max} = 6$.

Despite the Cartesian symmetry of HG modes' intensity profiles, we see a surprising lack of these highly symmetric features in our calculated auxiliary eigenmodes. All modes where $[j] \neq [0], [4]$ exhibit no reflection symmetry. This can be explained by examining the phase of each of the component HG modes for these equivalence classes. While the intensity profiles of these exhibit Cartesian symmetry, the phase profiles do not and the component modes for each of the auxiliary eigenmodes will have different symmetries. These differing symmetries end up braking each other and result in the lack of Cartesian symmetry in the auxiliary eigenmodes. In the case of $[j] = [0]$, we see that every HG mode in this equivalence class has matching indices, i.e., $m = n$ for HG^n_m. All these modes have phase and intensity profiles that are symmetric across the diagonal and antidiagonal axes, which result in an auxiliary eigenmode which is also symmetric across these axes. For $[j] = [4]$, if the equivalence class contains the mode $HG^{n'}_{m'}$, it must also contain the mode $HG^{m'}_{n'}$, i.e. $HG^{m'}_{n'} \in [4] \leftrightarrow HG^{n'}_{m'} \in [4]$. $HG^{m'}_{n'}$ is the reflection of $HG^{n'}_{m'}$ across either of the diagonal axes. The presence of both these modes in the equivalence class means they will both be in the superposition to form the auxiliary eigenmode and so the auxiliary eigenmode has the same reflection symmetry.

Another noticeable feature of the auxiliary eigenmodes is that their intensity profiles are aligned along the diagonal (45°) axis. This again is a result of the symmetries of the HG modes discussed the previous paragraph and not related to the resilience of the HG modes to astigmatism. It is well known that while an HG mode rotated by 45° might appear to be aligned to the x-y axes, it is not resilient to the astigmatism induced by the tilted lens and in fact undergoes mode conversion to and LG mode in the conversion plane[14]. Thus, there is an important subtlety to take note of. An HG mode in general is not resilient to some arbitrary astigmatic phase. An HG mode define in x-y is only resilient to astigmatism if that astigmatism is aligned over the x axis or y axis. If an HG mode is aligned along any other axis (such as 45° from the x axis), the HG mode will not be resilient to the astigmatic phase and will undergo mode conversion. This explains why the HG mode in the top row of Figure 3.10 remains unchanged under the applied astigmatism: the HG mode is aligned with x-y axis. In contrast to this, the LG mode in the second row is able to undergo mode conversion into an HG mode rotated by 45°. This HG mode is not aligned to the x-y axes and so is not resilient to the applied astigmatism.

Now that we know that the modes are robust through the astigmatic system, we can now examine how the modes evolve as we gradually increase the strength of the astigmatic phase. These results are shown in Figure 3.10. We first test an HG mode with indices $m, n = 4, 4$. This is an elementary eigenmode of the system since it is a pure HG mode. Its evolution under increasing astigmatism is shown in the first row and it remains unchanged as expected save for the divergence present in all common paraxial beams. We next send through an LG mode with indices $l, p = 5, 4$. Its evolution

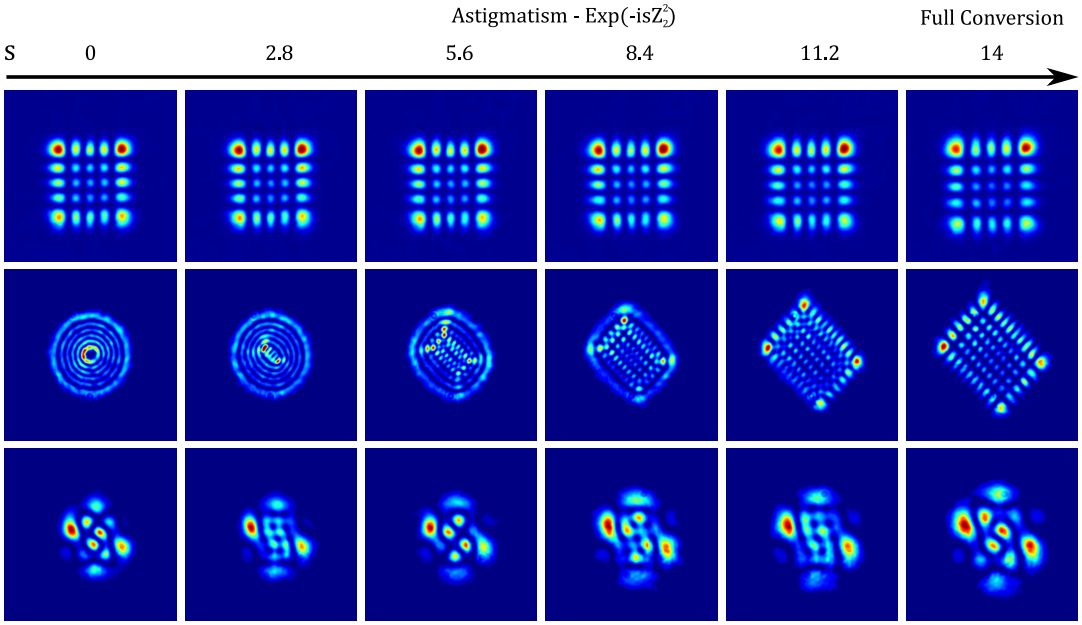


FIGURE 3.10: **Structured Beams under Varying Astigmatism.** Experimentally captured images of an HG beam, LG beam and auxiliary eigenmodes as increasing levels of astigmatism are introduced using Zernike polynomials. The top row shows that the HG mode remains invariant regardless of the degree of astigmatism added to the beam. The second row shows the modal conversion of a high order LG beam into a high order HG beam as the degree of astigmatism increases. The final row shows how an auxiliary eigenvector is affected by varying degrees of astigmatism.
This figure was adapted from reference [40] with consent from the authors.

under gradually increasing astigmatism is shown in the second row and it converts to an HG oriented at 45° as expected. We may also visually deduce the indices of the the converted HG to confirm the l and p indices of the incident LG beam according to Ref [13]. We finally send an auxiliary eigenmode through the system. The component HGs of the auxiliary eigenmode have a maximum mode order of $N_{max} = 6$ and all belong the to equivalence class $[j] = [3]$. Here we see that the intensity profile of the beam does change as the level of astigmatism increases. However, the original profile is recovered when the level of astigmatism is equal to that which would result in a full conversion of an incident LG beam. This reinforces the idea that while the auxiliary eigenmode is robust through the astigmatic channel, the definition of the channel is of vital importance. The operator we used to find the auxiliary eigenmode considers the mode at the initial plane as the input vector and the mode at the conversion plane as the output vector. While it might be possible that an eigenmode remains unchanged throughout the whole channel, that is not always the case and we can only in general be certain that the input mode will be recovered at the conversion plane. In all three cases, we see some scaling/axial divergence of the input mode as the level of astigmatism is increased. While this is one property of the beam that does change, it is not dissimilar to how HG and LG beams diverge in propagation but are still referred to as eigenmodes of free space. Our auxiliary eigenmodes are thus still valid eigenmodes of the system.

3.4 Discussion and Conclusion

While the task of finding structured light that is resilient to astigmatic systems is not new [30, 46], proposed studies have primarily focused on light with optical vortices. We see in particular that Ref [46] shows results that agree well with those seen in Figure 3.10. In contrast, the work in this section focuses on light that does not contain optical vortices and provides a solution to the challenge that uses well known beam shaping techniques and the well known HG modes.

Here, we leveraged the natural modal description of light present in the behaviour of the astigmatic system to define an operator that accurately describes the channel and allows us to find its eigenmodes. We started by first describing the channel using a novel mathematical model for the tilted lens as an optical element. We provided an accurate description of the channel and, for the first time in the literature, an analytical relationship between the level of astigmatism in the system and the plane of conversion. We then used the modal description to define an operator of this highly aberrated and astigmatic system to find the eigenvectors of this operator and their corresponding eigenvalues. We investigated a new class of these eigenvectors which we called the auxiliary eigenvectors/eigenmodes which were obtained using superpositions of HG modes, which are themselves eigenvectors of the operator. To simplify our investigation, we set the weighting coefficients in these superpositions all to 1. However this is not necessary for modes to remain robust through the system. We can choose the size and propagation dynamics of these auxiliary eigenvectors by selecting a maximum mod order. The modes in general do not remain unchanged when propagating through system, but do maintain the same profile at both the initial input plane and at the conversion plane of the lens, as was define by our operator. All of the auxiliary eigenvectors exhibit the same far field behaviour, which results in the intensity profile of the mode being reflected about the y axis when compared to the mode in the initial plane. A particularly interesting result is that the propagation of these auxiliary eigenmodes results in the build up of an intra-modal phase between the component HG modes in the superposition. This is a result of the mode order dependence of the Gouy phase. This intra-modal phase means that the intensity profile of the mode will change, but the mode as described in each subsequent plane of propagation is still an eigenmode of the system. However, it is also important to note that the strength of the astigmatism affects our ability to faithfully recover the eigenmode as shown in Figure 3.10. This work also has relevant practical implications, demonstrating that the eigenmodes of an aberration can also be adjusted to compensate for propagation after undergoing the relevant perturbations and still have a valid eigenmode at a user defined plane after the aberration. Such a method has potential applications is fields such as laser machining and for techniques such as robust quantum key distribution and quantum state tomography through aberrated media.

We have developed a procedure for finding the eigenmodes of an astigmatic system and we believe that this approach can be extended to other

unitary, aberrated optical systems. By taking advantage of the modal description of light and using it to probe the system, we can find not only the eigenmodes but also find useful structures and features (such as the periodicity of the eigenvalues). We can then extend the use of these eigenvalues to create informed superpositions, which are also eigenmodes and may have properties beyond the initial eigenmodes we obtain.

While we defined a specific equivalence classes in this investigation, different optical systems will lend themselves to other definitions for their equivalence class. These changes will be dictated by the behaviour and properties of that system and could vary greatly in size and type. However, the use of equivalence classes can be very flexible, with certain applications using the the Gouy phase and its effects to create these classes [39, 47].

Chapter 4

Modelling Atmospheric Turbulence

4.1 Kolmogorov Theory of Turbulence

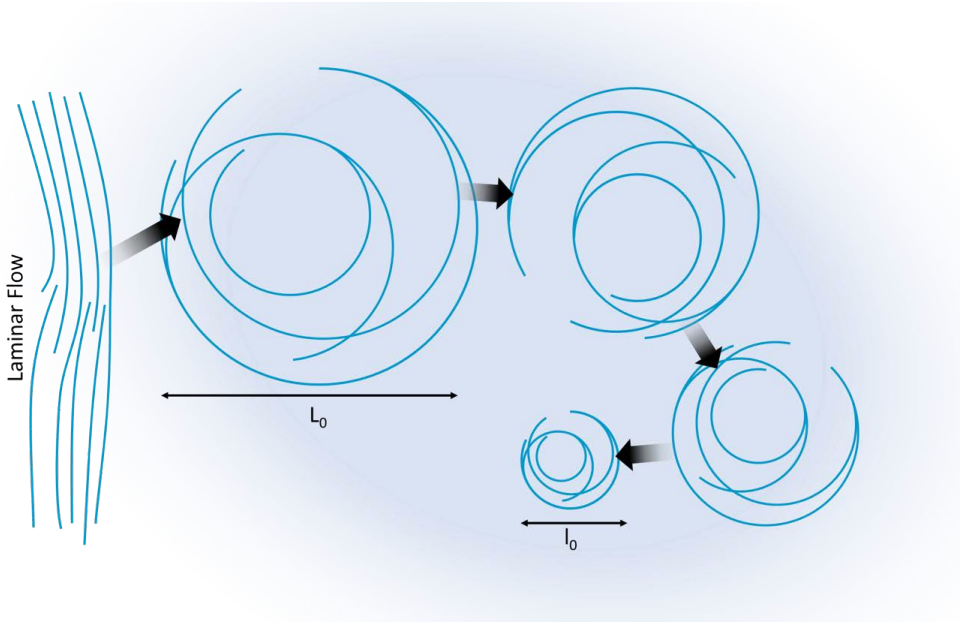


FIGURE 4.1: **Turbulent Energy Cascade.** The Kolmogorov model of turbulence models the cascade of energy through different length scales.We start at lengths large than the outer scale, at which all flow appears laminar due to the relative size of the flcutautions being too small to distinguish. Energy is then injected from this scale into the turbulent flow and the outer length scale L_0. The energy then Cascades through smaller and smaller eddies. Eventually the energy reaches the smallest eddies where the scale is small enough for the viscosity of the medium to dominate and energy is lost to heat and friction.

The atmosphere is a highly turbulent medium and thus very difficult to describe using typical fluid mechanics approaches such as the Navier-Stokes equations. In 1941, Andrey Kolmogorov proposed a statistical treatment of fluids with high Reynolds numbers. The Reynolds number is used to quantify and characterise how turbulent a particular medium is and is given by

[48]:

$$Re = \frac{\rho v L}{\mu} \tag{4.1}$$

where ρ is the density of the liquid, v is the speed of the fluid flow, L is the characteristic linear dimension and μ is the viscosity. Media with low Reynolds numbers are considered close to smooth/ laminar flows and media with high Reynolds numbers are considered turbulent flow.

In Kolmogorov's theory of turbulence, proposed by Andrey Kolomogorov in the 1940s [49], we study the flow of energy through the system. We begin at *outer length scale* L_0, at which energy is being injected into the system, driving the turbulent flow. The exact value of L_0 corresponds to the length at which two points in the system are still correlated. At any scale larger than L_0, the system will appear to have laminar flow. The injected energy cascades down to smaller length scales in the form of turbulent eddies. Here, the particles that make up the medium lose energy due to inelastic collisions with other particles, leading to the the formation of smaller and smaller eddies and the downward energy cascade. This energy loss will be captured by the energy dissipation rate ϵ. This process continues until the *inner length scale* l_0 is reached. At this scale the kinetic energy of the particles has become small enough that the viscosity μ of the medium becomes significant. The viscosity quantifies the effects of the friction created by the attractive forces between molecules in the medium. Thus, in this regime, the potential energy between the molecules becomes comparable to their kinetic energies. Since we are dealing with a fluid medium, we will use the kinematic viscosity $\eta = \mu/\rho$, which normalises out the volume and mass considerations to capture only the effect of the attractive and repulsive forces. The range of length scales between L_0 and l_0 is known as the *inertial sub-range*.

We can quantify the *inner length scale* l_0, also known as the *Kolmogorov micro-scale*, through the use of dimensional analysis. At this scale, the flow is dictated by two parameters: the energy dissipation rate ϵ, quantifying the behaviour due to the kinetic energy, and the kinematic viscosity η, quantifying the behaviour due to the potential energy. The units of both are $[\epsilon] = m^2.s^{-3}$ and $[\eta] = m^2.s^{-1}$. Combining both of these allows us to find a characteristic length scale l_0 and a characteristic time-scale t_0, given by,

$$l_0 = \left(\frac{\eta^3}{\epsilon}\right)^{\frac{1}{4}}, \tag{4.2}$$

$$t_0 = \left(\frac{\eta}{\epsilon}\right)^{\frac{1}{2}}. \tag{4.3}$$

The Kolmogorov model is powerful as it allows us to quantify the fluctuation in the medium within the inertial sub-range. We know that the energy changes as we move from larger eddies to smaller eddies. Thus, we can relate the velocity fluctuations δv to the length scale of the eddies we are interested in l. From these two quantities, we can determine a time scale at which these

fluctuations occur,

$$\tau = \frac{l}{\delta v}\,. \tag{4.4}$$

The turbulent kinetic energy E, the kinetic energy per unit mass in the medium must by definition be given by

$$E = \frac{1}{2}(\delta v)^2\,. \tag{4.5}$$

As the same kinds of particles are colliding at all length scale, we may assume that the loss in kinetic energy due the inelastic collisions is the same at all length scales and thus the energy dissipation rate is constant within our inertial sub-range. By combining Equations 4.4 and 4.5, we then have,

$$\begin{aligned} \epsilon &= \frac{E}{\tau} \\ &= \frac{1}{2}(\delta v)^2\frac{\delta v}{l} \\ &= \frac{1}{2}\frac{(\delta v)^3}{l} \\ \Rightarrow \delta v &= C_v l^{\frac{1}{3}},\ C_v = (2\epsilon)^{\frac{1}{3}}\,, \end{aligned} \tag{4.6}$$

where C_v is known as the velocity structure constant. We may also examine the behaviour of the fluctuations outside the inertial sub-range. For scales above the outer-scale L_0, we see laminar flow and so $\delta v = 0$ for $l \gg L_0$. For scales below the inner-scale/micro-scale l_0, we will consider an arbitrary length scale l_1 such that $l_0 > l_1$. The larger l_0 is compared to l_1, the more time it takes for energy to cascade down from l_0 to l_1. Consequently there is lower energy and smaller velocity fluctuations. Thus we see an inverse relationship between l_0 and δv in this regime. We may then adapt this into equation 4.6 as follows,

$$\delta v = C_v l_0^{-\frac{2}{3}} l\,, \tag{4.7}$$

where the extra factor of $l^{\frac{2}{3}}$ is brought in to keep everything dimensionally consistent. We therefore have,

$$\delta v = \begin{cases} C_v l^{\frac{1}{3}}, & \text{for } L_0 > l > l_0 \\ C_v l_0^{-\frac{2}{3}} l, & \text{for } l_0 > l \end{cases}\,. \tag{4.8}$$

We are also able to find relationships between the length scales and the energy. We must first define a spatial frequency or wavenumber such that $\kappa = l^{-1}$. We then define an energy spectrum $g(\kappa)$ such that the turbulent kinetic energy in the range from κ to $\kappa + \mathrm{d}\kappa$ is given by,

$$E = g(\kappa)\mathrm{d}\kappa\,. \tag{4.9}$$

Combining this with Equations 4.5 and 4.8 gives us the following,

$$\begin{aligned} g(\kappa)\mathrm{d}\kappa &= C_v \kappa^{-\frac{2}{3}} \\ \Rightarrow g(\kappa) &= C_v \kappa^{-\frac{5}{3}} \end{aligned} \tag{4.10}$$

From the above, we are able to easily calculate the energy at any particular length scale.

4.2 Statistics for Random Processes

In the previous section, we saw how we were able to relate the velocity fluctuations in our medium to the particular length scale and energy dissipation rate when working in the inertial sub-range. The only quantity that was not well defined was the velocity fluctuations. In this section we will find a clear and physical way of quantifying these fluctuations. Ideally, one would calculate these using principles from fluid dynamics such as the Navier-Stokes equations. However, Kolmogorov's model allows us to treat the flow as a random process. In this section we will then go through the various statistical concepts we will need in order to properly quantify the behaviour of our turbulent medium.

Let us assume we want to study a random process $x(t)$. As part of this investigation, we will measure/sample the variable x, n number of times at times $t_1, ..., t_n$. If this process depends on the difference between the times $\tau = t_2 - t_1$, then it is known as a stationary random process. For such processes, the moments exhibit time translation symmetry.

We may define the expectation value of a random process $x(t)$(also sometimes called the ensemble average) as follows,

$$\langle x(t) \rangle = m(t) = \int_{-\infty}^{\infty} x p_x(x,t)\mathrm{d}x\,, \tag{4.11}$$

where $p_x(x,t)$ the probability of measuring a value x at a position x at time t. The variance of the process is given by,

$$\sigma_x^2(t) = \langle x^2(t) \rangle - m^2(t) = \int_{-\infty}^{\infty} (x(t) - m(t))^2 p_x(x,t)\mathrm{d}x\,. \tag{4.12}$$

Here we have indicated a variance for any random process, but if our process is stationary, then it will be constant over time.

The correlation function for a stationary random process is given by,

$$R_x(t1,t2) = R_x(\tau) = \langle x(t_1)x(t_2) \rangle = \int_{-\infty}^{\infty}\int_{-\infty}^{\infty} x_1 x_2 p_x(x_1, x_2; \tau)\mathrm{d}x_1\mathrm{d}x_2\,. \tag{4.13}$$

The covariance function is given by,

$$\begin{aligned} B_x(t_1, t_2) &= \langle (x(t_1) - \langle x(t_1) \rangle)(x(t_2) - \langle x(t_2) \rangle) \rangle \\ &= \langle x(t_1)x(t_2) \rangle - m(t_1)m(t_2) \end{aligned} \tag{4.14}$$

From the covariance function we may calculate a quantity known as the power spectral density. Such a quantity allows us to study the random processes or events in frequency space. It is given by,

$$\Phi_x(\omega) = \int B_x(t) e^{2\pi i \omega t} \mathrm{d}t \,. \tag{4.15}$$

In certain models, both values should be real and so we may simplify the above to,

$$\Phi_x(\omega) = \int B_x(t) \cos(2\pi\omega t) \mathrm{d}t \,. \tag{4.16}$$

Turbulence is usually modelled as a small fluctuation from a mean value. We may model such a random process as,

$$x(t) = m(t) + x_1(t) \,, \tag{4.17}$$

where $x(t)$ is the variable of interest, $m(t)$ is the mean of that variable and $x_1(t)$ is how far that variable deviates from the mean at a time t. We define a special function for this process known as a structure function which is given by,

$$\begin{aligned} D_x(t_1, t_2) &= \langle (x(t_1) - x(t_2)) \rangle \\ &= (m(t_1) - m(t_2))^2 - \langle (x_1(t_1) - x_1(t_2)) \rangle \end{aligned} \tag{4.18}$$

We assume that for our process, the mean does not significantly change over time and so we have $m(t_1) \approx m(t_2)$ for small enough time period and so the structure function simplifies to,

$$D_x(t_1, t_2) \approx \langle [x_1(t_1) - x_2(t_2)]^2 \rangle \tag{4.19}$$

The structure function is related to the power spectral density via,

$$D_x(t_1, t_2) = 2 \int \Phi(\omega)(1 - \cos(2\pi\omega t)) \mathrm{d}\omega \tag{4.20}$$

4.3 Quantifying Atmospheric Turbulence

4.3.1 Refractive Index Fluctuations

We see that we can statistically quantify the fluctuations in a specific variable using the structure function as shown in Equation 4.19. We also saw that we can describe the velocity fluctuations in a turbulent medium using Equation 4.8. We may then combine these two observations as follows to obtain the

velocity structure function,

$$D_v(r) = \begin{cases} C_v^2 r^{\frac{2}{3}}, & \text{for } L_0 > r > l_0 \\ C_v^2 l_0^{-\frac{4}{3}} r^2, & \text{for } l_0 > r \end{cases} . \tag{4.21}$$

We see a natural extension of this theory for the velocity fluctuations to the temperature fluctuations, as both relate to the motion of the particles in our medium. We then get a temperature structure function as follows,

$$D_T(r) = \begin{cases} C_T^2 r^{\frac{2}{3}}, & \text{for } L_0 > r > l_0 \\ C_T^2 l_0^{-\frac{4}{3}} r^2, & \text{for } l_0 > r \end{cases} . \tag{4.22}$$

Any change in the temperature of the medium will alter the optical path length of any light propagating through it and thus will change the refractive index. This effect is what results in the phenomenon of atmospheric turbulence. Fluctuations in the refractive index over time and over space cause structured light fields to experience a different refractive index across the transverse plane, accumulating random phases as it propagates and ultimately leading to a distorted spatial profile at the output of a channel. Since these fluctuations also change with time, this distorted spatial profile will additionally change over time. We will then apply the various tools we have developed to understand and simulate the behaviour of the refractive index in a turbulent channel. To begin, we must work with a statistically homogeneous and isotropic variable. The refractive index n does not fit this criteria and so we will instead split it up into two components,

$$n(\mathbf{r}) = 1 + \delta n(\mathbf{r}) \tag{4.23}$$

The first term corresponds the mean value of the refractive index, which for air is $n_{\text{air}} = 1$. The second term δn represents the fluctuations in the refractive index. This variable has a mean value of $\langle \delta n \rangle = 0$ and is homogeneous and isotropic. The statistics of this variable are what will be interested in for the remainder of this chapter.

Refractive index fluctuations are related to the changes in the medium's temperature T and pressure P via [50, 51],

$$\delta n(\mathbf{r}) = 77.6 \times 10^{-6}(1 + 7.52 \times 10^{-3}\lambda^{-2})\frac{P(\mathbf{r})}{T(\mathbf{r})} , \tag{4.24}$$

which, for optical and near-infrared wavelengths frequently used in optical communication, simplifies to,

$$\delta n(\mathbf{r}) \approx 79 \times 10^{-6}\frac{P(\mathbf{r})}{T(\mathbf{r})} , \tag{4.25}$$

This is a good time to note that while atmospheric turbulence is a major contributor to the distortion of optical field through free space, there are several

other phenomenon that also affect beam propagation including but not limited to Mie scattering, Rayleigh scattering, molecular absorption and magnetic permeability changes in the ionosphere (in the case of ground to satellite links). These are all important phenomena to understand and overcome for use of optical light fields in atmospheric propagation and communication. However, we will restrict our investigation solely to the refractive index fluctuations caused by turbulent flow in the atmosphere. Pressure fluctuations are negligible when compared to temperature fluctuations. We therefore expect the behaviour of the refractive index fluctuations to follow the behaviour of the temperature fluctuations. We may then easily infer the refractive index structure function to be [51],

$$D_n(r) = \begin{cases} C_n^2 r^{\frac{2}{3}}, & \text{for } L_0 > r > l_0 \\ C_n^2 l_0^{-\frac{4}{3}} r^2, & \text{for } l_0 > r \end{cases} . \tag{4.26}$$

The proportionality constant C_n^2 is called the *refractive index structure constant* and is typically the quoted value when quantifying the strength of atmospheric turbulence. It typically changes over time and in space. The larger this value, the greater the fluctuations in the refractive index, and the stronger we consider the atmospheric turbulence. However, it is not the most ideal as there are additional factors that it does not take into account. More holistic ways of quantifying the effects of atmospheric turbulence will be discussed later. The value for C_n^2 is challenging to directly measure. Its value, and thus the strength of the turbulence is experimentally determined by measuring the temperature fluctuations in a medium and then relating the temperature structure constant to the refractive index structure constant via,

$$C_n = 79 \times 10^{-6} \frac{P}{T^2} C_T \, . \tag{4.27}$$

We are also able to obtain the power spectral density of the refractive index to be,

$$\Phi(k) = 0.033 C_n^2 k^{-\frac{11}{3}}, \ \frac{1}{l_0} > k > \frac{1}{L_0} \, . \tag{4.28}$$

4.3.2 Turbulence Parameters

As mentioned previously, the refractive index structure constant C_n^2 is not the most ideal measure for characterising a turbulent channel. Firstly, it has dimensions of length$^{1/3}$ and lacks an intuitive physical interpretation. This problem is overcome by the introduction of the Fried parameter r_0. For a channel with uniform C_n^2 throughout the path length, it is given by [51],

$$r_0 = \left(0.423 k^2 \int_0^L C_n^2(z) \mathrm{d}z \right)^{-\frac{3}{5}} = \left(0.423 C_n^2 k^2 L \right)^{-\frac{3}{5}} , \tag{4.29}$$

where L is the length of the channel and k is the wavenumber. The assumption that the refractive index structure constant remain unchanged over the propagation path, i.e., $C_n^2(z) = C_n^2$, is valid as long as the speed at which light propagates is much faster than the time taken for distortions along the path to change. The Fried parameter has dimensions of length and corresponds to the average distance between two points at which the refractive indices are correlated. For this reason, it is also sometimes called the *atmospheric coherence length*. A larger value for r_0 corresponds to longer correlation lengths and thus less severe turbulence and weaker distortions. Smaller values of r_0 correspond to points only being correlated over short distances and thus more severe turbulence and stronger induced distortions. While this quantity is more intuitive, it is important to consider it relative to the optical system we wish to characterise. Let us assume our system has an aperture of radius D, on the scale of the size of the optical beam we wish to send through the channel. If the Fried parameter is larger than the aperture of our system, $r_0 > D$, we would not expect there to be a lot of induced distortions from the refractive index fluctuations as they will be minimal at this scale. If the we have $D > r_0$, we would see that the fluctuations are no longer correlated within our aperture and thus we will observe significant distortions in our spatial profile. Thus not only is the correlation length of importance when characterising the optical system, but so is the size of the optical field or beam we wish to send through the system. To deal with these scale considerations and to allow for greater ease of comparison between systems, it is typical to not only quote the Fried parameter, but also the dimensionless quantity D/r_0, which takes these scale issue into considerations.

Now that we have a more intuitive way to characterise the refractive index fluctuations in our channel, we should now turn to the effects of propagation distance on the distortion. Let us consider an optical channel with a fixed value for r_0 and D. Since the distortions are induced by the accumulation of a random phase, we see that as the beam propagates further through channel, the spatial profile becomes increasingly aberrated. Thus, the performance and efficiency of the optical channel depends not only on the severity of the refractive index fluctuations, but also on the distance through which the beam must propagate. This prompts the introduction of new metric - the Rytov variance σ_R^2, which is given by,

$$\sigma_R^2 = 2.25k^{\frac{7}{6}} \int_0^L C_n^2(z)(L-z)^{\frac{5}{6}} \mathrm{d}z = 1.23 C_n^2 k^{\frac{7}{6}} L^{\frac{11}{6}} . \tag{4.30}$$

In the calculation of this parameter, we see that both the refractive index structure constant and the propagation path are included in the integrand. Consequently, both the refractive index fluctuations and the accumulated phase distortions from propagation are all taken into account when characterising the channel. A Rytov variance of $\sigma_R^2 < 1$ is generally considered weak turbulence while $\sigma_R^2 > 1$ would be considered to be in the strong regime. Values of $\sigma_R^2 \approx 1$ would be considered to be of a medium strength.

It is important to note that the Rytov variance does not take the aperture

size into account while the Fried parameter does. Thus, one should carefully consider the parameter of choice when simulating a turbulent channel. This ensures an accurate representation of the results are presented and allows for a fair comparison to other systems and methods.

The above metrics are all very valuable and allow for fair and robust characterisation of a simulated channel. However, these parameters are not easy to obtain experimentally. Additional metrics have been developed which allow for rapid, real world quantification of the turbulence strength. The first one of these we will look at is the Strehl ratio SR. This is defined as the ratio of the average on-axis intensity of the beam through a turbulent channel to the on-axis intensity in the absence of turbulence. If we assume the intensity of our beam is some spatially and temporally varying function $I(x, y, z, t)$ with turbulence and $I_0(x, y, z)$ in the absence of turbulence. Then we may express the Strehl ratio as,

$$\mathrm{SR} = \frac{\langle I(0,0,L,t)\rangle}{I_0(0,0,L)}\,, \tag{4.31}$$

where L is the length of the channel and $\langle\cdot\rangle$ represents the time average. We may relate the value of the Strehl ratio to the Fried parameter through the following approximation,

$$\mathrm{SR} \approx \frac{1}{\left[1 + (D/r_0)^{\frac{5}{3}}\right]^{\frac{6}{5}}} \tag{4.32}$$

Such a parameter is significantly easier to obtain as it can be calculated directly from intensity measurements taken through the channel. In cases where the intensity in the absence of turbulence I_0 is unknown, such as when measuring the turbulence through a real-world free space link or in general non-laboratory environments, we can make use of a parameter known as the scintillation index σ_I^2. This parameters characterises the turbulence strength from the intensity spread at the receiver and is given by,

$$\sigma_I^2 = \frac{\langle I^2\rangle - \langle I\rangle^2}{\langle I\rangle^2} = \frac{\langle I^2\rangle}{\langle I\rangle^2} - 1 \tag{4.33}$$

In the regime of weak turbulence, the scintillation index can be taken to be approximately the same as the Rytov variance.

4.4 Modelling the Phase Distortions

Before we can begin simulating turbulence, we must understand how the refractive index fluctuations affect the phase of each point in our optical field. To do this, we will turn again to the Helmholtz Equation 1.13 which governs the dynamics of a waves spatial profile in propagation. We will rewrite it to include the refractive index as follows,

$$\left(\nabla^2 + k^2 n^2\right) U(\mathbf{r}) = 0\,, \tag{4.34}$$

where previously the refractive index was set to $n = 1$ for vacuum propagation. We are now working with a non-uniform refractive index given by $n(\mathbf{r}) = 1 + \delta n$. We will assume that the fluctuations are small such that $1 \gg \delta n$. We may then make the approximation $n^2(\mathbf{r}) \approx 1 + 2\delta n$ via the binomial approximation. We may then rewrite Equation 4.34 as,

$$\left(\nabla^2 + k^2\right) U(\mathbf{r}) = -2\delta n(\mathbf{r}) k^2 U(\mathbf{r}) \,. \tag{4.35}$$

This has the same form as Equation 1.27 - an inhomoegeneous Helmholtz equation where the driving term is given by $f(\mathbf{r}) = 2\delta n(\vec{)}k^2 U(\mathbf{r})$. We may then use the results from Equation 1.43 and substitute in our driving term to get,

$$U(\mathbf{r}) = \int \frac{e^{ik|\mathbf{r}-\mathbf{r}'|}}{4\pi|\mathbf{r}-\mathbf{r}'|} 2\delta n(\mathbf{r}') k^2 U(\mathbf{r}') \mathrm{d}^3 r' \,. \tag{4.36}$$

This is now an integral equation and is in general not initially very useful as it requires knowledge of the field $U(\mathbf{r}')$. We may overcome this by making use of the *Born Approximation* [51]. This approximation assumes we may expand our field $U(\mathbf{r})$ as a sum of component fields,

$$U = U_0 + U_1 + U_2 + ... \tag{4.37}$$

If we substitute this expansion into Equation 4.35, we obtain,

$$\begin{aligned} \nabla^2 U_0 + \nabla^2 U_1 + \nabla^2 U_2 + ... + k^2 U_0 + k^2 U_1 + k^2 U_2 + ... \\ = -2\delta n k^2 U_0 - 2\delta n k^2 U_1 - 2\delta n k^2 U_2 - ... \end{aligned} \tag{4.38}$$

We wish to look at the 0th, 1st and 2nd order expansions of our optical field. With this in mind, we can easily compare and group terms with the same order and thus are left with the following equations,

$$\left(\nabla^2 + k^2\right) U_0 = 0 \,, \tag{4.39}$$

$$\left(\nabla^2 + k^2\right) U_1 = -2\delta n k^2 U_0 \,, \tag{4.40}$$

$$\left(\nabla^2 + k^2\right) U_0 = -2\delta n k^2 U_1 \,. \tag{4.41}$$

Looking at Equation 4.39, we see that the zeroth order expansion of the field U_0 satisfies the homogeneous Helmholtz equation. Thus, the zeroth order terms of our field should correspond to the eigenmodes of free space derived in Chapter 1 (Bessel-,Laguerre- and Hermite-Gaussian beams). Thus to see how the refractive index fluctuations affect the field we must move to the next order perturbations. Equation 4.36 implies that the 1st and 2nd order

perturbations to the field (U_1 and U_2 respectively) are given by,

$$U_1(\mathbf{r}) = \int \frac{e^{ik|\mathbf{r}-\mathbf{r}'|}}{4\pi|\mathbf{r}-\mathbf{r}'|} 2\delta n(\mathbf{r}')k^2 U_0(\mathbf{r}')\mathrm{d}^3r' . \tag{4.42}$$

$$U_2(\mathbf{r}) = \int \frac{e^{ik|\mathbf{r}-\mathbf{r}'|}}{4\pi|\mathbf{r}-\mathbf{r}'|} 2\delta n(\mathbf{r}')k^2 U_1(\mathbf{r}')\mathrm{d}^3r' . \tag{4.43}$$

While these fields can be solved, they require a significant amount of computation and one must solve several integral equations and obtain various statistical quantities for the refractive index fluctuations.

An easier approach to understanding the effect of the refractive index fluctuations is through the use of the Rytov approximation. In this approximation, we assume that the perturbed field may be written as follows,

$$U(\mathbf{r}) = U_0(\mathbf{r})e^{G(\mathbf{r})} . \tag{4.44}$$

This separates the field into two factors: U_0 is the unperturbed field and thus satisfies the homogeneous Helmholtz equation 4.34 and the exponential with $G(\mathbf{r})$ which is a complex valued, spatially varying function that captures the deviations from the vacuum/unperturbed solutions caused by the atmospheric turbulence. The exact form for the function $G(\mathbf{r})$ can be obtained when we stay in the weak turbulence regime with a Rytov variance of $\sigma_R^2 < 1$. In such a regime, we assume that the effects of atmospheric turbulence manifest solely as a phase perturbation in the field [51]. Thus we have,

$$G(\mathbf{r}) = i\Theta(\mathbf{r}_\perp), \text{ with } \Theta(\mathbf{r}_\perp) = k\int_0^L \delta n(\mathbf{r}_\perp, z)\mathrm{d}z , \tag{4.45}$$

where $\mathbf{r}_\perp$ is the position vector in the transverse x-y plane and L is the path-length of the channel. Here, the spatially varying phase function $\Theta(\mathbf{r}_\perp)$ represents the total phase distortions accumulated by the optical field as it propagates through a turbulent channel of path-length L.

Equation 4.45 shows that the phase function is simply an integral (or sum) over the refractive index fluctuations. Since most of the statistical properties we have been interested are linear, this means all the relationships that apply to δn will also apply to Θ. This phase function is therefore statistically homogeneous and isotropic. This has the convenient result of depending solely on the absolute distance between two points $|\mathbf{r}_\perp| = r$ and not the azimuthal angle.

Now that we know the relationship between the accumulated phase and the refractive index fluctuations, we can look at the the statistical properties

of the phase. The covariance function is given by,

$$\begin{aligned}\mathcal{B}_\Theta(r) = \langle\Theta(\mathbf{r}'_\perp)\Theta(\mathbf{r}''_\perp)\rangle &= k^2\iint\langle\delta n(\mathbf{r}'_\perp,z')\delta n(\mathbf{r}''_\perp,z'')\rangle\mathrm{d}z'\mathrm{d}z'' \\ &= k^2\iint\delta(z'-z'')A_n(r)\mathrm{d}z'\mathrm{d}z'' \\ &= 4\pi Lk^2\int_0^\infty q\Phi(q)J_0(qr)\mathrm{q} \end{aligned} \tag{4.46}$$

Due to the delta correlation between the refractive index fluctuations in the direction of propagation in our turbulence model, we see that the function A_n is the power spectral density of the refractive index. We can use the earlier definition of the power spectral density to find the covariance function as follows,

$$\begin{aligned}\mathcal{B}_\Theta(r) &= 2\pi zk^2\int\Phi_n(\mathbf{q})e^{i\mathbf{q}\cdot\mathbf{r}}\mathrm{d}^2\mathbf{q} \\ &= \int\Phi_\Theta(\mathbf{q})e^{i\mathbf{q}\cdot\mathbf{r}}\mathrm{d}^2\mathbf{q} \\ \Rightarrow\Phi_\Theta(k) &= 2\pi zk^2\Phi_n(k) = 0.49\frac{k^{-\frac{11}{3}}}{r_0^{\frac{5}{3}}}. \end{aligned} \tag{4.47}$$

From the above we can also immediately obtain the structure function for the phase as,

$$\mathcal{D}_\Theta(r) = 2\int\Phi_\Theta(q)\left[1-\cos(i\mathbf{q}\cdot\mathbf{r})\right]\mathrm{d}q = 6.88\left(\frac{r}{r_0}\right)^{\frac{5}{3}}. \tag{4.48}$$

4.5 Turbulence Phase Screens

We now have a sufficient understanding of the statistics and Physics of atmospheric turbulence to numerically and experimentally simulate a turbulent channel. We begin by recalling that, in the weak regime, turbulence is considered only a phase perturbation and thus can be approximated by apply a single phase screen element to our incident optical field and then propagating it through the length of the channel. It is vital to note that this only replicates a channel with weak turbulence ($\sigma_R^2 < 1$), and methods to replicate medium and strong turbulence will be discussed in a later section. This phase element will consist of the aberrated phase Θ, discussed in the previous section. There are many ways to accurately replicate this aberrated phase, but we will focus on the *Fourier transform method* which will be used in all the numerical and experimental investigations throughout the remainder of this work. We will first give an overview of how we may sample from a distribution of a Gaussian-random variable to construct our turbulence phase screen, improve our sampling method to accurately match experimental observables to ensure our phase screen matches the theoretical predictions of the model

we used to construct them; and then give an overview of the calibration procedure required for an effective and accurate experimental implementation of these screens.

4.5.1 Fourier Transform Method

The idea behind the the Fourier transform method is to generate the phase aberrations, not in the spatial domain, but instead in the frequency domain. Then perform an inverse Fourier transform to obtain the spatially varying profile of the phase aberration. Since we may only numerically define the spatial domain up to a certain minimum size (the size of a single pixel for example), we shall define our aberrated phase as a function of the discrete coordinates (x_p, y_q) where the indices run from $p = 1, ..., N$ and $q = 1, ..., M$ respectively. Let the sample spacing/pixel size be δx and δy in the horizontal and vertical directions, respectively. In this way we have $x_p = p\delta x$ and $y_q = q\delta y$. In other words, x_p gives the value of p-th discrete coordinate in the x-direction and y_q gives the value of q-th discrete coordinate in the y-direction. The total size of the field is then given by $L_x = N\delta x$ and $L_y = M\delta y$. The aberrated phase Θ may be expanded as a 2-dimensional discrete Fourier series as follows,

$$\Theta(x_p, y_q) = \sum_n \sum_m c_{nm} e^{2\pi i \left[\frac{np}{N} + \frac{mq}{M}\right]} . \tag{4.49}$$

From this we can immediately infer the Fourier coefficient c_{nm} to be given by,

$$c_{nm} = \frac{1}{NM} \sum_p \sum_q \Theta(x_p, y_q) e^{-2\pi i \left[\frac{np}{N} + \frac{mq}{M}\right]} \tag{4.50}$$

Since we have extensively studied the statistical properties of this phase perturbation, it is natural then to study the variance of these coefficients as we know the variance of the phase perturbation. Using the relationships derived earlier in this chapter, we may relate the variance of these coefficients to power spectral density of perturbation by,

$$\begin{aligned} \langle |c_{nm}|^2 \rangle &= \frac{1}{N^2 M^2} \sum_{pp'} \sum_{qq'} \langle \Theta(x_p, y_q) \Theta(x_{p'}, y_{q'}) \rangle e^{-2\pi i \left[\frac{n(p-p')}{N} + \frac{m(q-q')}{M}\right]} \\ &= \frac{1}{N^2 M^2} \sum_{pp'} \sum_{qq'} \mathcal{B}(x_p, y_q) e^{-2\pi i \left[\frac{n(p-p')}{N} + \frac{m(q-q')}{M}\right]} \\ &= \frac{1}{L_x L_y} \Phi(k_n, l_m) . \end{aligned} \tag{4.51}$$

Here k_n and l_m are the sampled, discrete horizontal and vertical frequencies respectively. The result of Equation 4.51 allows us to sample the expansion coefficients c_{nm} from a Gaussian distribution with mean of 0 and a variance of $\Phi(k_n, l_m)\delta k \delta l$. These may then be plugged into equation 4.49 to construct our turbulent phase screen.

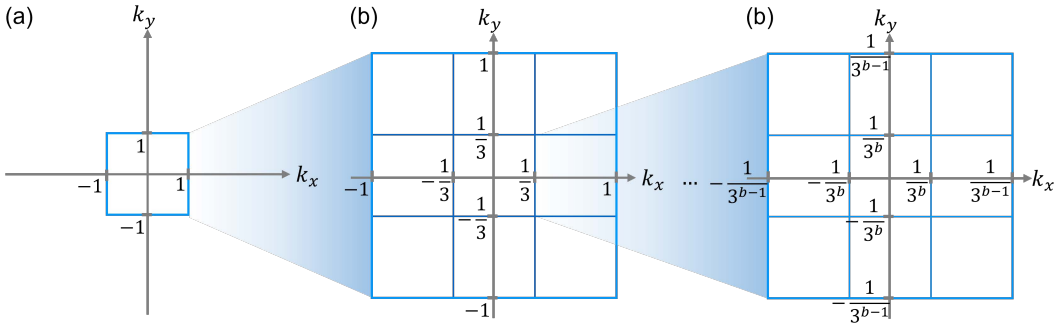


FIGURE 4.2: **Subharmonic Sampling.** (a) We isolate a square of twice unit side-length around the origin of our phase profile in the Fourier domain. (b) We divide this small square into a 3×3 grid and use these new, small grid squares to sample smaller frequencies. (c) We can repeat this process up to an arbitrary number of subharmonics where the sizes of the grids are determined through the shown dimensions, where b is the subharmonics we are sampling.

Subharmonic Sampling

We have now developed a method of naively producing a turbulence phase screen using Fourier transforms. However these screens also fall short when we consider the form of our energy spectrum/power spectral density given by Equation 4.28. Here, the wavenumber is raised to the power of $-11/3$. So, very small frequencies will have a significant contribution to the overall field. The smallest frequencies sample by our method are given by the reciprocal of our field's size in real space $k = 1/L_x$ and $l = 1/L_y$. To ensure frequencies smaller than these are included in the spectrum, we will employ a technique known as subharmonic sampling.

We begin by focusing on the region around the origin in the Fourier domain, dividing it into a three-by-three grid. The sides of the central grid square are therefore located a distance of $1/3$ of the units from the origin. This is shown visually in Figure 4.2 (a) and (b). This new, smaller grid gives us access to what is called the first *subharmonic* and allows us to sample smaller frequencies and consequently more accurately construct the phase screen using the method described in the previous section. We can repeat this process, each time using the central square from the previous subharmonic to sample decreasingly smaller frequencies and obtain an ever more accurate phase screen. It is important to note that since these subharmonic grids consist of pixels that are smaller than the pixels used to sample the higher frequencies (by a factor of $1/3$ for each subharmonic), we must scale the contributions of the subharmonic terms by a factor of $(1/3)^b$, where b is the number of the subharmonic. We can express this subharmonic sampling as,

$$\Theta_{sub}(x_p, y_q) = \sum_b \sum_n \sum_m c_{nm} e^{2\pi i \left[\frac{np}{3^b N} + \frac{mq}{3^b M}\right]}. \tag{4.52}$$

Here, the term with $n = m = 0$ is not summed over. The coefficient for the subharmonic grid are sample from a Gaussian distribution with mean zero

and variance of,

$$\left(\frac{1}{3^b}\right)^2 \frac{\Phi(k_n, l_m)}{L_x L_y}. \tag{4.53}$$

Once these subharmonic terms have been calculated, they can be added to the naively computed phase screen with only the high frequencies. Thus our total phase screen is given by,

$$\begin{aligned}\Theta(x_p, y_q) &= \Theta_{high}(x_p, y_q) + \Theta_{sub}(x_p, y_q) \\ &= \sum_n \sum_m c_{nm} e^{2\pi i\left[\frac{np}{N} + \frac{mq}{M}\right]} + \sum_b \sum_n \sum_m c_{nm} e^{2\pi i\left[\frac{np}{3^b N} + \frac{mq}{3^b M}\right]}.\end{aligned} \tag{4.54}$$

One question then remains: what is a suitable number of subharmonics to accurately recreate the effects of atmospheric turbulence? To investigate this, we performed a Strehl ratio test. We simulate the propagation of a Gaussian beam propagating through a weakly turbulent channel. This is done by adding on the turbulent phase from the calculated phase screen and propagating the beam to the far field. We compare the average on axis intensity of these aberrated Gaussian beam profiles with that of a Gaussian beam that has been propagated through a uniform, unaberrated channel and calculate the Strehl ratio according to Equation 4.31. This can be compared to the theoretical behaviour of the Strehl ratio give in Equation 4.32. The results of this investigation are shown in Figure 4.3. From this we can see that once the screen is calculated to 5 subharmonics or more, we closely match the theoretical curve predicted for the Strehl ratio. Thus, going forward, unless otherwise stated, any turbulence phase screen is calculated to 5 subharmonics. The reason being that additional subharmonics will not provide any significant improvement but will greatly increase the computation time taken to generate each screen.

4.5.2 Split Step Method

We now know how to calculate and simulate the phase aberrations induced by optical atmospheric turbulence. As mentioned previously, the single phase screen approximation only replicates turbulence in the weak regime ($\sigma_R^2 < 1$). In the most general case, we will want to simulate channels of varying turbulence strengths, including medium and strong turbulence $\sigma_R^2 \geq 1$. To replicate the effects of the higher regimes, we will employ a procedure known as the *split step method*.

The split step method involved breaking up the total path-length into smaller segments or steps. The length and aberration strength of each of these segments is chosen such that the turbulent effects in that segment meet the criteria for the weak regime (σ_R^2). Thus, for each segment, we may use the single phase screen approximation. The final simulation will therefore involve applying an initial phase screen, then propagating the field a distance Δz. The next phase screen is applied and the field is propagated a further distance Δz. This is repeated until the desired effects/strength is obtained.

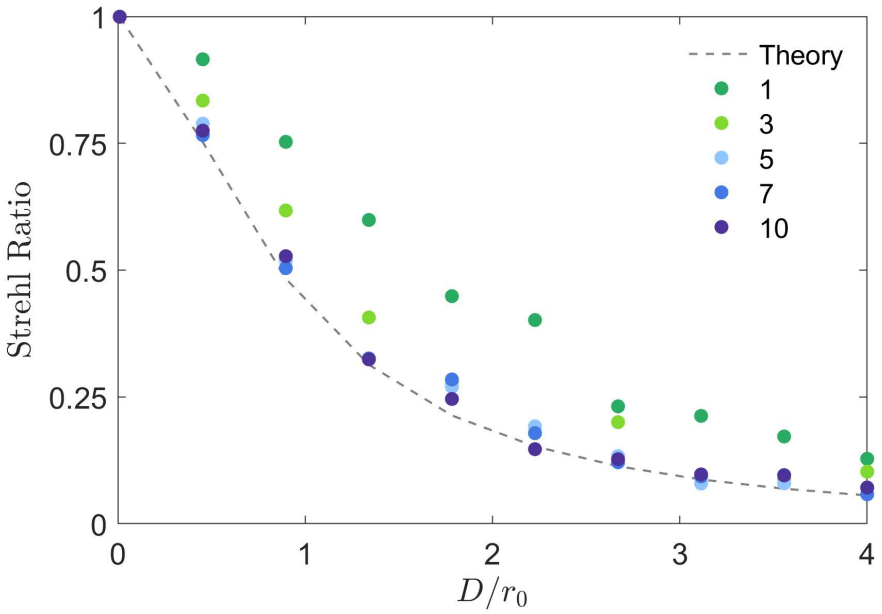


FIGURE 4.3: **Strehl Ratio Test.** Here we see the calculated Strehl ratio from the simulated propagation of a Gaussian beam through a turbulent channel. This is plotted against the turbulence strength D/r_0 programmed into the turbulence phase screen constructed using the Fourier transform method to various subharmonics. The dashed line show the theoretically predicated relationship between the Strehl ratio and the turbulence strength D/r_0.

To determine how many screens we need to use and the strength of the aberration on each screen, we must return to our definitions for the Fried parameters r_0 and Rytov variance σ_R^2. Since our method is taking a continuous volume of aberrations and breaking it up into a discrete number of phase screens, we must change our integral in Equation 4.29 into a discrete sum,

$$r_0 = \left(0.423k^2C_n^2\sum_{j=1}^{N}\Delta z_j\right)^{-\frac{3}{5}}, \tag{4.55}$$

where we have divided our channel into N segments and assume that our refractive index structure constant is uniform throughout the channel. We will assume each segment is of equal length and so $\Delta z_j = \Delta z = L/N$, where L is the total path-length. From this, we are able to find the Fried parameters for each of the segments $r_{0,s}$ (which will be needed for generating the individual phase screen),

$$r_{0,s} = \left(0.423k^2C_n^2\Delta z\right)^{-\frac{3}{5}}, \tag{4.56}$$

and the Fried parameters for the entire channel r_0 (which is needed to quantify the turbulence strength of the entire channel). These are related, via

Equation 4.55 as follows,

$$\begin{aligned} r_0 &= \left(0.423k^2C_n^2\sum_{j=1}^{N}\Delta z\right)^{-\frac{3}{5}} \\ &= \left(\sum_{j=1}^{N}0.423k^2C_n^2\Delta z\right)^{-\frac{3}{5}} \\ &= \left(\sum_{j=1}^{N}\left(\left(0.423k^2C_n^2\Delta z\right)^{-\frac{3}{5}}\right)^{-\frac{5}{3}}\right)^{-\frac{3}{5}} \\ &= \left(\sum_{j=1}^{N}r_{0,s}^{-\frac{5}{3}}\right)^{-\frac{3}{5}} \\ &= \left(Nr_{0,s}^{-\frac{5}{3}}\right)^{-\frac{3}{5}} \\ &= N^{-\frac{3}{5}}r_{0,s} \end{aligned} \tag{4.57}$$

One of the implications of Equation 4.57 that the Fried parameter of the entire channel is larger than the Fried parameters of each individual segment and screen. To obtain a discretized form of the Rytov variance, we will perform a similar procedure and change the integral in Equation 4.30 into a discrete sum,

$$\sigma_R^2 = 2.25k^{\frac{7}{6}}C_n^2\sum_{j=1}^{N}(L-z_j)^{\frac{5}{6}}\Delta z\,. \tag{4.58}$$

If we position the screens in the centre of each of the segments and ensure that each segment is of equal length, we obtain on expression for z_j,

$$z_j = \frac{L}{2N} + \frac{L(j-1)}{N}\,, \tag{4.59}$$

Thus we get the following expression for the discrete Rytov variance,

$$\sigma_R^2 = 2.25k^{\frac{7}{6}}C_n^2L^{\frac{5}{6}}\sum_{j=1}^{N}\left[1-\frac{1}{N}\left(j-\frac{1}{2}\right)\right]^{\frac{5}{6}}\Delta z\,, \tag{4.60}$$

where $z = L/N$. Since we define the power spectral density of our phase screens in terms of the Fried parameter, it is useful to also express our Rytov variance in terms of the Fried parameters of each segments so that we more easily see the link between the two. This relationship is obtained by

combining Equations 4.56 and 4.60 to obtain,

$$\sigma_R^2 = 5.32k^{-\frac{5}{6}}L^{\frac{5}{6}}r_{0,s}^{-\frac{5}{3}}\sum_{j=1}^{N}\left[1-\frac{1}{N}\left(j-\frac{1}{2}\right)\right]^{\frac{5}{6}} = \sum_{j=1}^{N}\sigma_{R,j}^2\,. \tag{4.61}$$

There is a very interesting observation we can make when studying Equation 4.61: the Rytov variance decreases as we move through one segment to the next. This implies that the closer the phase screen is to the source of the light field, the greater the effect it will have on the distortion of the beam at the receiver. This makes intuitive sense as the phase aberrations in earlier screens along the path will have significantly more propagation distance to manifest themselves as phase and amplitude perturbations compared to aberrations introduced later in the propagation. This observation also makes it significantly easier to ensure our model holds to the single phase screen approximation for atmospheric turbulence. We simply need to enforce the condition that the Rytov variance of the first phase screen is in the weak regime, i.e.,

$$\sigma_R^2 = 5.32k^{-\frac{5}{6}}L^{\frac{5}{6}}r_0^{-\frac{5}{3}}\left[1-\frac{1}{N}\left(\frac{1}{2}\right)\right]^{\frac{5}{6}} < 1\,, \tag{4.62}$$

to ensure that the effects of each segment in our split step propagation path meet the requirements for the weak turbulence regime. However, by using Equation 4.61, we may model a channel of any strength σ_R^2 (weak, medium or strong) and any distance L simply by selecting an appropriate number of segments N and the appropriate Fried parameter for the phase screen in each segment $r_{0,s}$.

4.5.3 Calibration of Experimental Phase Screens

We have now developed a way to experimentally simulate the effects of weak turbulence using turbulence phase screens and simulate medium and strong turbulence using a careful choice of multiple, evenly space turbulent phase screens. Before we can use these screens to perform tests on real-world beams, we must calibrate the screens relative to the size of the beam being used. This is because the beam must interact with a sufficient area of the turbulence phase screen to constitute the same experience of turbulence under the programmed turbulence conditions. If the aperture size is chosen to be too small, a large portion of the beam will not experience the distortions and so we will not measure the perturbations that accurately correspond to the programmed turbulence strength. Meaning, we must find a suitable value for the aperture size D relative to the size of the beam waist w_0 that returns the expected degree of distortion from the turbulence phase screens. We would then adjust the turbulence by changing the correlation length/Fried parameter r_0.

Since we will be comparing programmed values to experimental measurements, it is natural to again use the Strehl ratio as a metric since it links an easily measured quantity to the aperture size D and Fried parameter

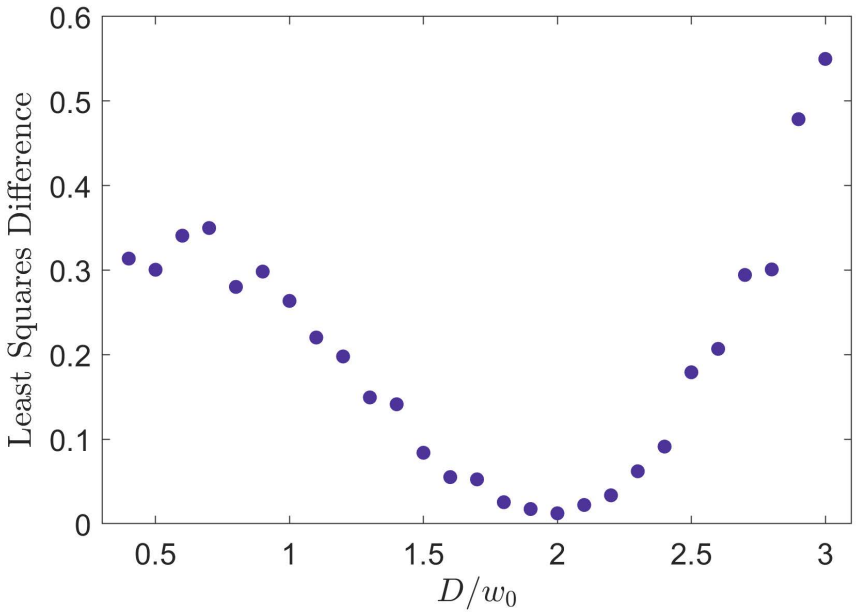


FIGURE 4.4: **Least Squares Fitting.** Plot showing the least squares difference (LSD) between the theoretically predicted Strehl ratio vs. the simulated Strehl ratio for various choices of normalised aperture size D/w_0. For this simulation we average over 100 turbulence phase screens for each turbulence strength D/r_0, measure 40 turbulence strengths for each choice of aperture size D and measure the aperture size between $D = 0.4w_0$ to $D = 3w_0$ in increments of $0.1w_0$. The beam used is a Gaussian beam of waist w_0.

r_0 through an analytical expression. We may then iterate through various values of D and measure the Strehl ratio for a various range of turbulence strengths D/r_0 and see which value of D most closely matches the theoretical Strehl ratio given by Equation 4.32. Since we will need to choose various apertures sizes D and for each choice of D measure various turbulence strengths D/r_0 and average over a large number of screens for each turbulence strengths, we will first simulate the various parameters to see which gives the best fit to the theoretical Strehl ratio. For this simulation, we use 100 turbulence phase screens for each turbulence strength, measure 40 turbulence strengths for each choice of aperture size and measure the aperture size between $0.4w_0$ to $3w_0$ in increments of $0.1w_0$. To quantify how well each choice of D fits the theoretical Strehl ratio curve in Equation 4.32, the least squares difference (LSD) between the simulated results and the theoretical curve wave calculated. The results of this are shown in Figure 4.4. From these results, we see that the optimal choice for the aperture size id $D = 2w_0$. The beam used in this simulation is a Gaussian beam with a beam waist of w_0. The minimum achieved by this fitting procedure may not be the global minimum. However, the range of values tested in the simulation are the range of value possible for implementation in the the experimental setups that are available to simulate the turbulent channel. Thus, this optimal value is the only choice in order to best replicate the desired turbulent channel.

We next experimentally confirm the choice of $D = 2w_0$ experimentally.

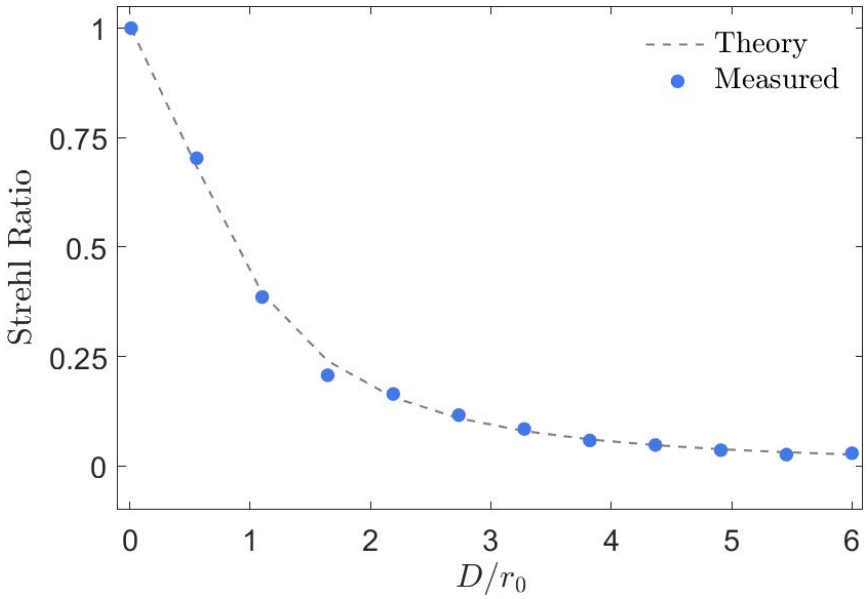


FIGURE 4.5: **Phase Screen Calibration.** Plot showing the least squares difference (LSD) between the theoretically predicted Strehl ratio vs. the simulated Strehl ratio for various choices of normalised aperture size D/w_0. For this simulation we average over 100 turbulence phase screens for each turbulence strength D/r_0, measure 40 turbulence strengths for each choice of aperture size D and measure the aperture size between $D = 0.4w_0$ to $D = 3w_0$ in increments of $0.1w_0$. The beam used is a Gaussian beam of waist w_0.

A Gaussian beam multiplied by the turbulence phase screen was encoded onto the SLM via complex amplitude modulation (see Chapter 2). The on-axis intensity, with and without turbulence, is measured using a CCD. The results form this are shown in Figure 4.5, where we plot the measure Strehl ratio vs. the programmed turbulence strength. This plot is compared to the theoretical relationship predicted by Equation 4.32. From these results we see almost perfect agreements between the measured values and the theoretical prediction, thus confirming the accuracy of calibration procedure and our choice of $D = 2w_0$.

Chapter 5

Eigenmodes of Atmospheric Turbulence

This chapter is based on the paper:

Asher Klug, **Cade Ribeiro Peters** and Andrew Forbes, "Robust structured light in atmospheric turbulence," (2023)
Advanced Photonics, Vol. 5, Issue 1, 016006

C. Peters performed several of the numerical simulations, assisted in designing and building the experiment, performed the experiment, analysed the data and contributed to writing the manuscript.

Structured light is routinely used in free space optical communication channels, both classical and quantum, where information is encoded in the spatial structure of the mode for increased bandwidth. Both real-world and experimentally simulated turbulence conditions have revealed that free-space structured light modes are perturbed in some manner by turbulence, resulting in both amplitude and phase distortions, and consequently, much attention has focused on whether one mode type is more robust than another, but with seemingly inconclusive and contradictory results. Here, we present complex forms of structured light which are invariant under propagation through the atmosphere: the true eigenmodes of atmospheric turbulence. We provide a theoretical procedure for obtaining these eigenmodes and confirm their invariance both numerically and experimentally. Although we have demonstrated the approach on atmospheric turbulence, its generality allows it to be extended to other channels too, such as aberrated paths, underwater and in optical fibre.

5.1 Introduction

Free-space transmission of electromagnetic waves is crucial in many diverse applications, including sensing, detection and ranging, defence and communication, and extends over distances from the long (Earth monitoring) to the

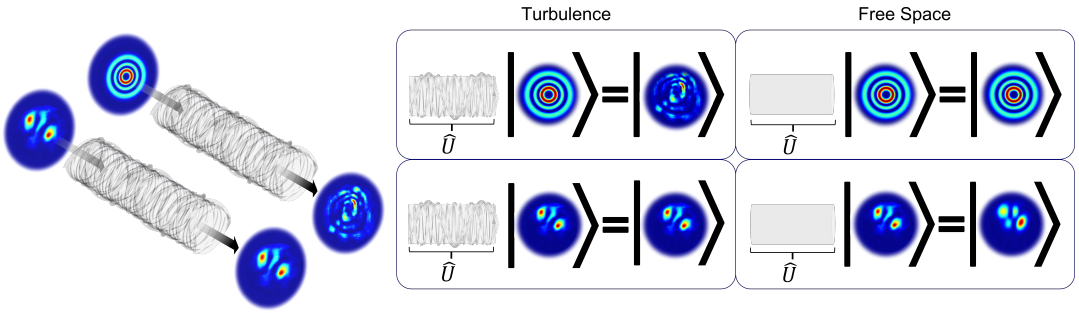


FIGURE 5.1: **Propagation through Turbulence.** Most common forms of structured light (such as Laguerre-Gaussian modes) become distorted when propagating through free space due to the effects of atmospheric turbulence, whereas an eigenmode of atmospheric turbulence will remain unchanged when propagating through the same channel, as shown in the left panels. In contrast, the eigenmodes of turbulence will not be the eigenmodes of pristine free space, as shown on the right panels.

short (WiFi and LiFi). Lately there has been a resurgence of interest in free-space optical links [52, 53], driven in part by the need for increased communication bandwidths [54, 55], with the potential to bridge the digital divide in a manner that is license-free [56]. Here the spatial modes of light have come to the fore, for so-called space division multiplexing [57] and mode division multiplexing [58], where the spatial structure of light is used as an encoding degree of freedom. This in turn has fuelled interest in structured light [59, 60], where light is tailored in all its degrees of freedom, including amplitude, phase and polarisation, enabled by a modern structured light toolkit [61].

A commonly used form of structured light is that of beams carrying orbital angular momentum (OAM), where the phase spirals around the path of propagation azimuthally [62]. These modes provide a (theoretically) infinite and easily realised alphabet for encoding information [63, 64] and have been used extensively in optical communication (see Refs. [65, 66] for good reviews). Vectorial combinations of such beams create inhomogeneous polarisation structures [15, 67, 68] and too have found applications in free-space links [69, 70]. Although these structured light fields hold tremendous potential for free-space optical communication, they are distorted by atmospheric turbulence as a phase perturbation in the near-field and an amplitude, phase and polarisation perturbation in the far-field [71]. This corrects the myth that vectorial light is immune to atmospheric turbulence by virtue of its polarisation components - it is not. What is invariant is its vectorness, how inhomogeneous the polarisation structure is (but not how it looks), which can potentially be exploited for error-free optical communication [72]. This modal scattering induced cross-talk decreases the information capacity of classical atmospheric transmission channels [73–82] while reducing the degree of entanglement in quantum links [83–92]. Mitigating this remains an open challenge that is intensely studied.

Arguments have been put forward for one mode family being more robust than another, with studies covering Bessel-Gaussian [93–104], Hermite-Gaussian [105–108], Laguerre-Gaussian [109–113] and Ince-Gaussian [114]

beams, with mixed and contradictory results. In the context of OAM, since the atmosphere itself can be thought of giving or taking OAM from the beam, it has been shown theoretically and experimentally that atmospheric turbulence distortions are independent of the original OAM mode [115], all susceptible to the deleterious effects of atmospheric turbulence, and indeed OAM has been suggested as not the ideal modal carrier through turbulence [116]. Vectorial structured light has been suggested to improve resilience because of the invariance of the polarisation degree of freedom, but numerous studies in turbulence [117–124] have been inconclusive, with some reporting that the vectorial structure is stable [118, 119, 124], and others not [120–123, 125]. Careful inspection of the studies that report vectorial robustness in noisy channels reveal that the distances propagated were short and the strength of perturbation low, mimicking a phase-only near-field effect where indeed little change is expected, and hence these are not true tests for robustness or invariance. Studies that claim enhanced resilience of vector modes over distances comparable to the Rayleigh length [118, 124] have used the variance in the field's intensity as a measure, a quantity that one would expect to be robust due to the fact that each polarisation component behaves independently and so will have a low covariance. This failing of structured light in turbulence has led to numerous correction techniques, including novel encoding/decoding methods [126], modal diversity as an effective error-reduction scheme [127], traditional adaptive optics for pre- and post-correction [128–130] as well as vectorial adaptive tools [131], iterative routines [132] and deep learning models [133].

Here we present a class of structured light whose entire structure in amplitude and phase remains invariant as they propagate through a turbulent free-space channel. We deploy an operator approach to find the eigenmodes of atmospheric turbulence, a significant departure from prior phenomenological approaches. Unlike other spatial modes, these exotically structured eigenmodes need no corrective procedures and are naturally devoid of deleterious effects such as modal crosstalk. Moreover, they are valid over long paths and strong aberrations, a regime that is no longer phase-only and thus traditional adaptive solutions for correction fail. We demonstrate this invariance numerically and confirm it experimentally with a laboratory simulated long path comprising weak, medium and strong turbulence, implemented using multiple turbulent phase screens along the propagation path. Our approach offers a new pathway for exploiting structured light in turbulence, and can be easily extended to arbitrary noisy channels.

5.2 The Eigenmodes of Turbulence

5.2.1 Instantaneous eigenmodes

The concept we tackle here is illustrated in left panels of Fig. 5.1. Some optical field passes through an arbitrary distance of atmospheric turbulence, treated as a continuous medium of potentially strong turbulence, and which we will refer to as our channel. The conventional forms of structured light such as

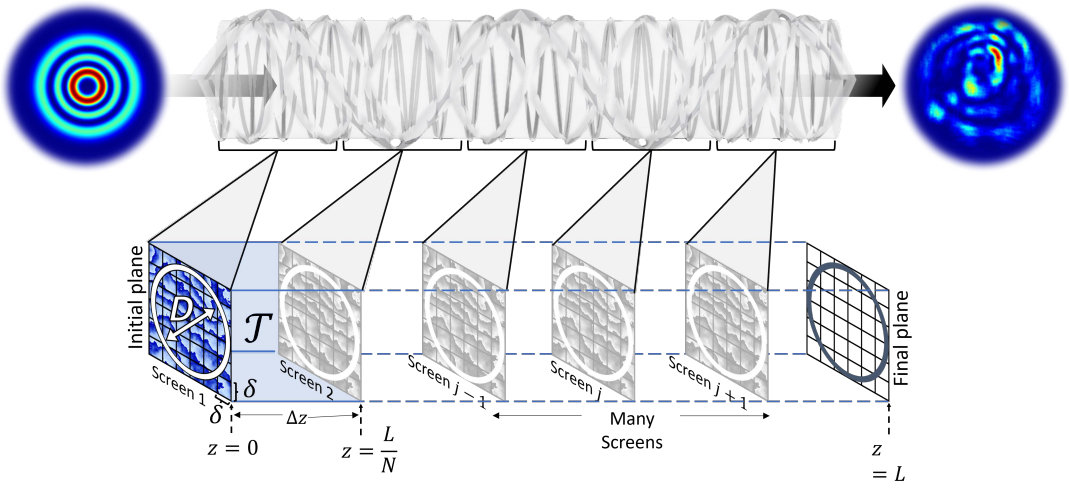


FIGURE 5.2: **The Unit Cell.** The first turbulent screen is placed at the beginning of the channel, at $z = 0$, with subsequent screens placed a distance $\Delta z = L/N$ away from the prior, where N is the number of turbulent phase screens used. Each phase screen and distance form a unit cell, the first highlighted in blue, forming N unit cells over the complete path length of $z = L$. The operator for each unit cell, $\mathcal{T}$, is identical, so we need only consider the first unit cell. The initial plane is discretised into pixels with side length δ and turbulence is simulated with a strength characterised by the ratio D/r_0, where D is the aperture of the inscribed circle and r_0 is the Fried parameter. The operator describes the action of an imprinted turbulent phase on the beam, followed by vacuum propagation over a distance Δz.

Laguerre-Gaussian beams are typically distorted after propagation through such a channel, but are invariant to unperturbed free-space. In contrast, the eigenmodes of the medium are complex forms of structured light that are invariant to the channel, emerging distortion free, but then are not eigenmodes of unperturbed free-space.

In our approach to the problem, we treat the channel as an operator, $\hat{\mathcal{U}}$, that acts on the input field to return an output field, namely

$$\hat{\mathcal{U}} u_{\text{in}} = u_{\text{out}} \,. \tag{5.1}$$

This is illustrated in right panels of Fig. 5.1, with the operator and input/output fields shown schematically (note that in the absence of turbulence the operator just describes free-space). The operator is unitary if the transmitting and receiving apertures are sufficiently large to accommodate the number of eigenmodes utilised, which can be approximated by its free space limit of $N_{\text{max}} \approx A_t A_r/(\lambda^2 L^2)$ where A_t and A_r are the transmitter and receiver aperture areas separated by a distance L for light of wavelength λ. Equation 5.1 can be recast as an eigenvector problem by insisting that $u_{\text{in}} = u_{\text{out}} = |\gamma\rangle$ so that

$$\hat{\mathcal{U}} = \sum_i s_i \, |\gamma_i\rangle \, \langle\gamma_i| \,. \tag{5.2}$$

The challenge is to find these eigenvectors, $|\gamma_i\rangle$, by decomposition of the channel operator as a transmission matrix with elements U_{ij} that maps the

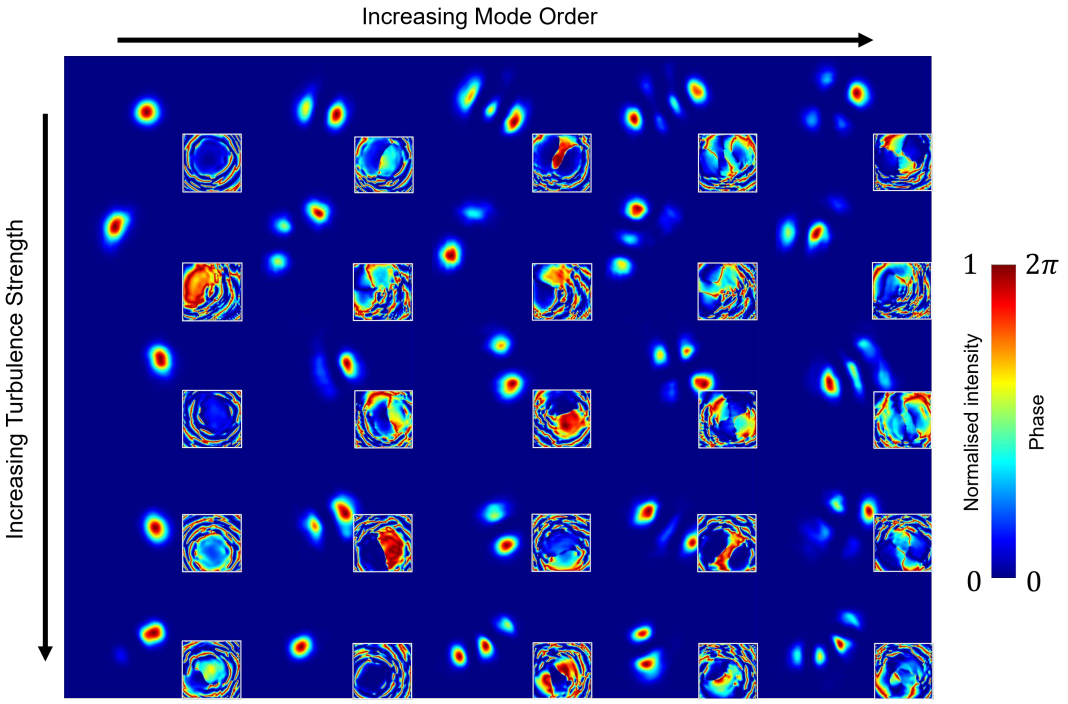


FIGURE 5.3: **Eigenmodes of Turbulence.** The numerically calculated eigenmodes of turbulence, showing the first five modes (columns) as a function of turbulence strength (rows). The insets show the phase profile. All eigenmodes were calculated for a total propagation path of 100 m through weak, medium and strong turbulence as defined by the Rytov variance (σ_R^2) and Fried parameter (r_0). The first two rows show eigenmodes of weak turbulence with $\sigma_R^2 = 0.5$ and $r_0 = 1.8$ mm. The next two rows show eigenmodes of medium turbulence with $\sigma_R^2 = 1$ and $r_0 = 1.2$ mm. The last row shows eigenmodes of strong turbulence with $\sigma_R^2 = 1.5$ and $r_0 = 0.91$ mm.

input to the output, i.e.,, $u_i = \sum_j U_{ij} u_j$. This is a variant of singular value decomposition (SVD), which solves the eigenvector equation at *two* planes for *two different* sets of modes [134]. This ensures orthogonality at the receiver by allowing the optical fields to evolve in transmission, say from modes $|\phi_i\rangle$ at the transmitter to $|\psi_i\rangle$ at the receiver, but at the expense of invariance. We wish to find the modes that are invariant (robust) to the channel, the true eigenmodes of the channel, so that transmitter and receiver share a common mode set. Because of the unitarity of the problem, the eigenvector equation is numerically stable and can be solved by a variety of standard numerical tools, so the task is to decompose the channel operator as matrix elements. There are a variety of approaches to do this, with successful theoretical demonstrations including using SVD in turbulence with OAM and pixel modes at the transmitter and receiver [135, 136], and experimental demonstrations using point sources for eigenmodes of scattering media [137, 138]. In the language of quantum mechanics, the nature of the problem lends itself to a process tomography of the channel [139], which by the isomorphism of

channel and state means that a quantum state tomography [140] will completely retrieve the channel matrix, as shown in quantum channels of complex optical fibre [141] as well as in classical-quantum channels through turbulence [142, 143]. We believe that this is a promising avenue to explore as it may offer benefits over the classical approach, which typically probes the channel one mode at a time. Nevertheless, the point is that standards tools exist to tackle the problem both experimentally and computationally.

In our work we will use the pixel basis to express the eigenmodes, inspired by the form of the paraxial free-space Green's function. The channel tomography however can be done in any complete and orthogonal basis for sending and receiving modes, to reconstruct a channel matrix $A = PUQ^\dagger$, where P and Q are the unitary matrices that perform the basis transformations, which following the earlier example might be $Q = \sum_p |\phi_p\rangle \langle\gamma_p|$ and $P = \sum_q |\psi_q\rangle \langle\gamma_q|$ from which U can be again deduced.

5.2.2 Time Averaged Eigenmodes

The analysis in the previous section assumed that the channel matrix was fixed at some instant in time, or equivalently, that the light transit time is much shorter than the coherence time of the turbulence. It is instructive to consider what might happen if one instead considers a time averaged result. Turbulence is a stochastic process in which the refractive index of the Earth's atmosphere varies according to well-known statistics, having zero mean and some non-zero variance. To see the impact of averaging over many different instances of turbulence on the robustness of modes, we use the the Helmholtz equation in the non-paxarial form through a thick and varying medium defined by the function $\delta n(\mathbf{r})$

$$\left(\nabla^2 + k^2\right) \mathrm{V} = -2k^2 \delta n \mathrm{V}, \tag{5.3}$$

which has the solution

$$\mathrm{V}(\mathbf{r}') = 2k^2 \int \mathrm{d}^3\mathbf{r}\ G(\mathbf{r}, \mathbf{r}') \mathrm{V}(\mathbf{r}) \delta n(\mathbf{r}), \tag{5.4}$$

with $G(\mathbf{r}, \mathbf{r}') = \exp(ik\|\mathbf{r} - \mathbf{r}'\|)/4\pi\|\mathbf{r} - \mathbf{r}'\|$ being the free-space Green's function and $\mathbf{r} = (\mathbf{x}, z)$. Taking the ensemble average and using the result that $\langle \delta n \mathrm{V} \rangle = \mathcal{A} \langle \mathrm{V} \rangle$ [144], we find

$$\left\langle \mathrm{V}(\mathbf{r}') \right\rangle = 2k^2 \mathcal{A} \int \mathrm{d}^3\mathbf{r}\ G(\mathbf{r}, \mathbf{r}') \left\langle \mathrm{V}(\mathbf{r}) \right\rangle, \tag{5.5}$$

where the constant $\mathcal{A}$ is related to the covariance of the refractive index fluctuations. We recognize that Eq. 5.5 is identical to the usual, zero-turbulence Fresnel integral, up to a constant. Therefore, the averaged eigenmodes should be solutions to the free-space, no turbulence, case. In other words, if the channel involves some form of averaging, say at the detector, then the best mode

set in this case is identically the traditional free-space modes in various geometries, e..g, the Hermite-Gaussian and Laguerre-Gaussian modes.

5.3 Numerical Simulation: Multiple Phase Screen Example

Conceptually one can imagine that the real path through turbulence is subdivided into many units, each containing a single phase-only turbulent screen and a zero turbulence propagation path of length Δz. We realise that in the language of operators, the action of each unit on some field is given by the product of the operators for turbulence and free-space propagation, which we denote by $\mathcal{T}$. This picture serves to confirm that the complete channel operator can be treated as unitary since it can be written as a product of unitary operators. We will now use this approach *by way of example* to build up a turbulence operator for the long/thick medium because (in the absence of a real-world channel) it lends itself directly to numerical testing and experimental verification of the concept in the laboratory.

To begin, we note that the effects of turbulence are mathematically captured in the stochastic refractive index $n = 1 + \delta n$, where δn is the random variation in the refractive index of the Earth's atmosphere. It is assumed that δn has a zero mean value, i.e., $\langle \delta n \rangle = 0$, and that the variation is small, so $|\delta n| \ll 1$. The introduction of this varying term produces the stochastic paraxial Helmholtz equation for a field $\mathrm{V}(x, y, z)$

$$\left(\nabla_t^2 + 2ik\partial_z + 2k^2\delta n\right)\mathrm{V} = 0, \tag{5.6}$$

where ∇_t^2 is the transverse Laplacian and $k = 2\pi/\lambda$ is the wavenumber for wavelength λ.

Equation 5.6 can be solved numerically according to the split-step method [145], illustrated in Fig. 5.2. Multiple random phase screens are placed at various distances along the beam's propagation path. Importantly, each screen is in the weak turbulence limit and contributes a random phase Θ_j, where j labels the jth screen, so that a single screen approximation is valid, but the sum of many such screens can lead to medium or even strong turbulence. In general the screens at each distance are different, but for pedagogical reasons we start with a simplistic example (to illustrate the concept) where we imagine that the path is subdivided into identical units, each containing such a single screen and a zero turbulence propagation path of length Δz. The action of $\mathcal{T}$ on a field V is given by the Huygen-Fresnel integral with a turbulent phase factor

$$\mathcal{T}\mathrm{V} \equiv \int \mathrm{d}^2\mathbf{x}\ g(\mathbf{x}, \mathbf{x}'; \Delta z) \exp(i\Theta)\mathrm{V}(\mathbf{x}, z = 0), \tag{5.7}$$

where

$$g(\mathbf{x}, \mathbf{x}'; \Delta z) = \frac{1}{i\lambda\Delta z} \exp\left(\frac{i\pi}{\lambda\Delta z}\|\mathbf{x} - \mathbf{x}'\|^2\right) \tag{5.8}$$

is the paraxial free space Green's function and $\mathbf{x}$, $\mathbf{x}'$ are the two-dimensional coordinates of the initial and final planes, respectively. We then discretize $\mathbf{x}$ and $\mathbf{x}'$ into grids of $N \times N$ points. The coordinates are labelled $\mathbf{x} \equiv (x_\alpha, y_\beta)$ and $\mathbf{x}' \equiv (x_\mu, y_\nu)$, so that $\mathcal{T}$ is given by

$$\begin{aligned}\mathcal{T}_{\mu\nu\alpha\beta} = \frac{1}{i\lambda\Delta z} \exp\left(\frac{i\pi}{\lambda\Delta z}\left(x_\mu - x_\alpha\right)^2\right) \\ \times \exp\left(\frac{i\pi}{\lambda\Delta z}\left(y_\nu - y_\beta\right)^2\right) \exp\left(i\Theta(x_\alpha, y_\beta)\right).\end{aligned} \tag{5.9}$$

An eigenmode E is then a solution to the tensor eigenvalue equation

$$\gamma_n \mathrm{E}^n_{\mu\nu} = \mathcal{T}_{\mu\nu\alpha\beta}\mathrm{E}^n_{\alpha\beta}, \tag{5.10}$$

where γ_n is the eigenvalue of the nth eigenmode. Repeated indices are implicitly summed over and $\mathrm{E}_{\mu\nu} \equiv \mathrm{E}(x_\mu, y_\nu)$. To convert the above tensor equation into the usual matrix-vector form, we specify a mapping ρ that acts on the indices (α, β) and (μ, ν) and "counts" them, first by columns and then by rows, such that $\rho(1,1) = 1$, ..., $\rho(N,1) = N$, $\rho(1,2) = N+1$ up to $\rho(N,N) = N^2$. This mapping lets us rewrite Eq. 5.10 as

$$\gamma_n \mathrm{E}^n_i = \mathcal{T}_{ij}\mathrm{E}^n_j, \tag{5.11}$$

since $\rho(\alpha, \beta) = j$ and $\rho(\mu, \nu) = i$. This equation can be routinely solved using numerical methods to find the eigenmodes of the unit cell operator. The action of the full channel is then described by the product $\mathcal{T}_n ... \mathcal{T}_1$ of repeated unit cells, and as per the definition of eigenmodes, they remain invariant regardless of the number of operators applied. To simulate more realistic conditions that change from cell to cell, the individual operators can be set appropriately so that in general $\mathcal{T}_n \neq \mathcal{T}_{n+1}$, but the product of operators still holds true.

5.3.1 Numerical Results

We follow the split-step approach shown in Fig. 5.2 to calculate the eigenmodes and numerically propagate them through atmospheric turbulence. For clarity and brevity we show only the low order eigenmodes and use the OAM modes as our point of comparison. We describe the turbulence conditions by Fried's parameter $r_0 = \left(0.423k^2C_n^2L\right)^{-3/5}$ and the Rytov variance $\sigma_R^2 = 1.23C_n^2k^{7/6}L^{11/6}$ using the plane-wave approximations [51] over a path of length L. These parameters are given in the captions of all results.

Examples of the intensity and phase of the eigenmodes are shown in Fig. 5.3 for various examples of turbulence. Here the first five eigenmode solutions are shown in the left column, increasing from left to right, with the rows corresponding to the turbulence strength, increasing from top to bottom. Although these are complex forms of structured light, as eigenmodes of

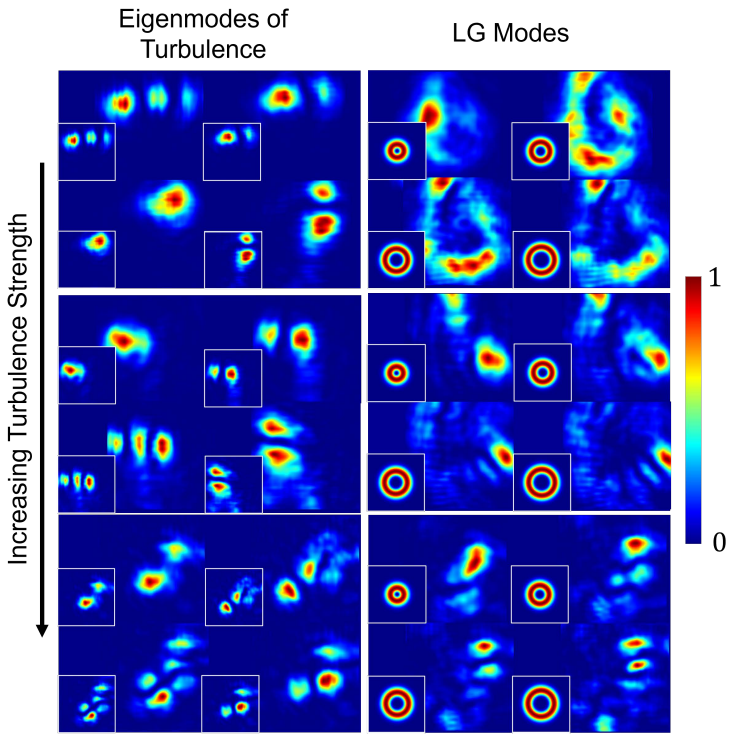


FIGURE 5.4: **Invariance of Eigenmodes under Numerical Propagation through Turbulence.** The eigenmodes (left) and LG modes (right) after numerical propagation through weak, medium and strong turbulence through a channel equivalent to propagating over a distance of 100 m. The insets shows the modes before experiencing turbulence. The numerical simulations used the split step method with three unit cells each consisting of a turbulence screen with a given r_0 followed by 33.33 m of propagation. Three unit cells were chosen to most closely match the experimental conditions implemented later in this chapter. Weak turbulence was characterised by $\sigma_R^2 = 0.5$ and $r_0 = 1.8$ mm, medium turbulence by $\sigma_R^2 = 1$ and $r_0 = 1.2$ mm and strong turbulence by $\sigma_R^2 = 1.5$ and $r_0 = 0.91$ mm

turbulence they should be invariant after propagation through a turbulent atmosphere. To test this, we propagate OAM carrying Laguerre-Gaussian (LG) modes and the eigenmodes through various scenarios of turbulence over a 100 m path length, with the results shown in Fig. 5.4. OAM modes were selected as they are very popular forms of structured light used in free-space studies. Their popularity, however, is not commensurate with their robustness in turbulence, as their phase profiles are sensitive to atmospheric distortions. We see that while the OAM modes are distorted (as expected), the eigenmodes are robust. This can be quantified by performing a modal analysis [9] at the end of the turbulent channel, as would be the case in optical communication at the receiver. In Fig. 5.5 we see that while the crosstalk is substantial for OAM modes when propagated through turbulence, evident from the many off-diagonal terms, the eigenmode crosstalk matrix remains diagonal after the same channel, for minimal crosstalk.

It is useful to study the behaviour of the eigenmodes of turbulence as they propagate through a channel with no turbulence and that is absent of any

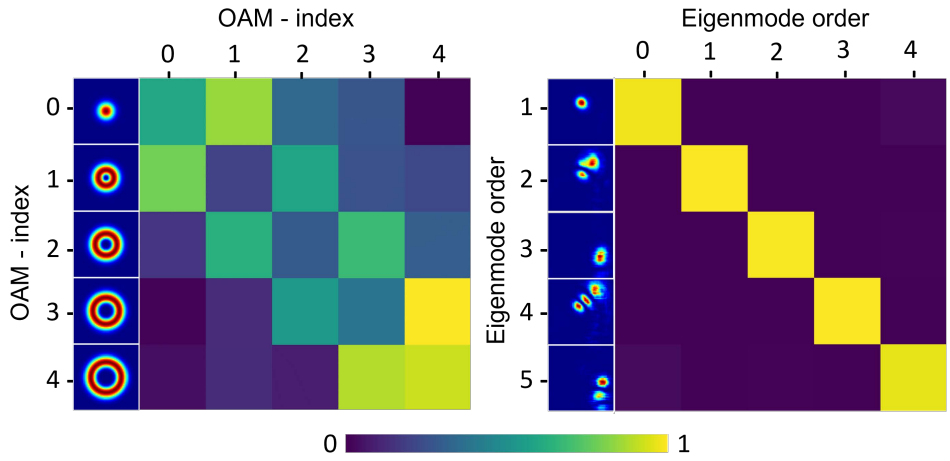


FIGURE 5.5: **Crosstalk-Free Transmission.** Simulated crosstalk matrices for OAM modes $\ell \in [0, 4]$ (top) and eigenmodes (bottom) with insets showing the intensity of the beams. The eigenmodes are unchanged and remain orthogonal, whereas the OAM modes scatter into each other. Turbulence results shown for $D/r_0 = 2$ with a total path length of 100 m and a beam waist parameter for the OAM beams of $w_0 = 6.67$ mm.

other perturbations. Laguerre-Gaussian and Hermite-Gaussian are eigenmodes of such a channel and thus will propagate through it unperturbed. This can be seen in the first row of Figure 5.6 where several LG modes of increasing OAM are numerically propagate through a 100 m free space channel and show no aberrations. The eigenmodes of weak, medium and strong turbulence (in the second, third and fourth rows respectively) are also propagated through this channel. They show very noticeable changes in their intensity distributions thus demonstrating that they are not eigenmodes of free space. However, the change they undergo in free space is not so significant as to make them unrecognizable and they retain many of their original features such as a general pattern and number of lobes. When comparing this to Figure 5.4, it appears that the changes undergone by eigenmodes of turbulence in free space are less severe than changes undergone by the eigenmodes of free space in turbulence.

Real-world turbulent channels have differing unit cells, and to illustrate such an example we simulate a slant path from high altitude to the Earth's surface. In this case, the turbulence strength changes as a function of altitude, and likewise the phase screen in each cell. The starting altitude of the channel was 500 m and the zenith angle was 170° (the zenith angle is greater than 90° as we are propagating downward from a point of high altitude to the surface of the Earth). This corresponds to a path length of 508 m and an angle of 80° below the horizontal. To calculate the turbulence strength at each altitude, the Tartarski model [146] was used to calculate the values for the refractive index structure constant

$$C_n^2(h) = C_{n0}^2 h^{-b}, \tag{5.12}$$

where $C_{n0}^2 = 4.16 \times 10^{-13}$ m$^{2/3}$ and $b = 4/3$ are constants selected to most

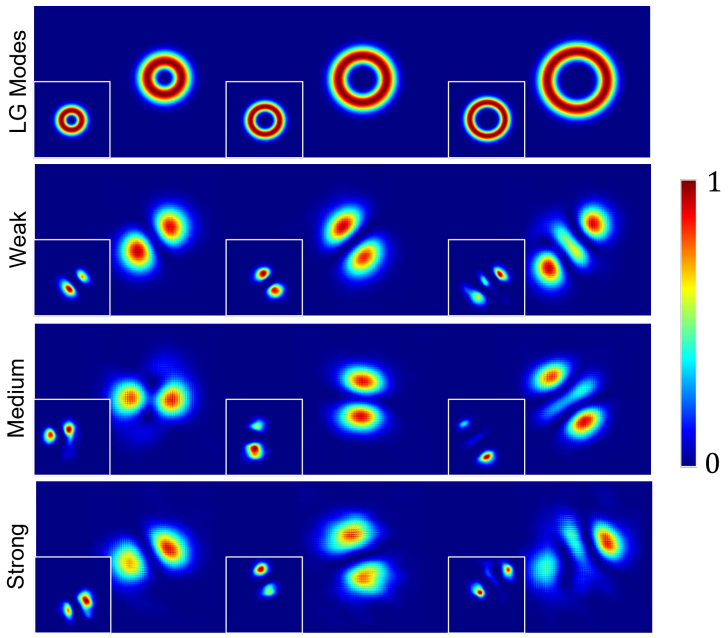


FIGURE 5.6: **Eigenmodes of Turbulence through an Unperturbed, Uniform Medium**. The Laguerre-Gaussian modes (top row) propagate through free space unaberrated as they are solutions to the free space paraxial Helmholtz equation. The eigenmodes of weak, medium and strong turbulence (second, third and fourth row respectively), while still recognizable, show noticeable changes in when passing through a channel with no turbulence. The insets show the modes before propagation and the larger images show the modes after propagation through a 100 m free space channel with no turbulence. Weak turbulence was characterised by $\sigma_R^2 = 0.5$ and $r_0 = 1.8$ mm, medium turbulence by $\sigma_R^2 = 1$ and $r_0 = 1.2$ mm and strong turbulence by $\sigma_R^2 = 1.5$ and $r_0 = 0.91$ mm

closely fit experimental data and h is the altitude. The slant path length through the atmospheric layer is given by $\Delta l_i^2 = \Delta h_i^2 + \Delta z_i^2$ where Δh_i^2 is the height of the atmospheric layer and Δz_i^2 is the horizontal component of the beam's path through the layer and the channel was broken up into 14 unit cells. The phase screens were then distributed evenly along the path and the values for $C_{n_i}^2$ where calculated for each phase screen at position of each phase screen. The calculated eigenmodes for this example are shown in Figure 5.7, where we see some striking similarity to low-order superpositions of the free space modes. More importantly, we note that the before and after intensity structures are in good agreement, indicative of an eigenmode.

5.4 Experimental Results

The experiment, shown in Fig. 5.8, is conceptually divided into three parts. In the generation stage, a He-Ne laser beam (wavelength $\lambda = 633$ nm) was expanded using a $10\times$ objective lens L_1 and then collimated by L_2 (f_2 = 150 mm) before being directed onto a reflective PLUTO-VIS HoloEye spatial light modulator (SLM). The initial field was generated by using the Arrizón type 3 technique [147] to shape the incident beam into the desired mode by complex

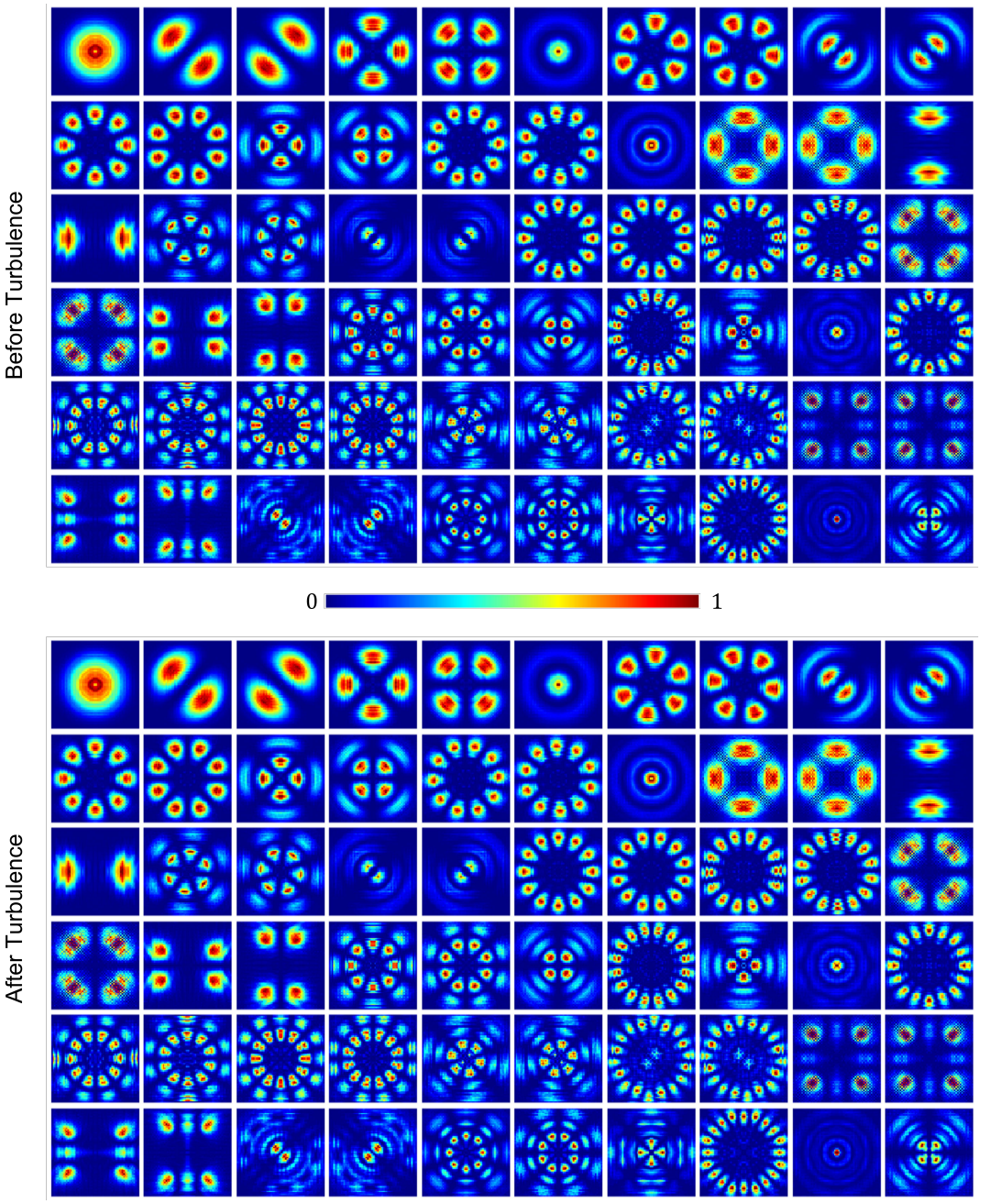


FIGURE 5.7: **Eigenmodes of a Slant Path.** The initial eigenmodes (top) and those after propagation (bottom) through a slant path towards the ground. The invariance is clear with the before and after intensity structures remarkably similar. We also note the strong similarity to free-space modes because the turbulence conditions were moderate.

amplitude modulation (amplitude and phase control). This field then entered the turbulent section of the setup where it passed through three unit cells, each comprising the same random phase screen and a propagation distance of one metre. The same phase screen was repeated for ease of calculation. In a real-world channel, the phase screens would not be correlated, however, the method would still remain unchanged as demonstrated in the previous section. The phase screens were generated using the sub-harmonic random

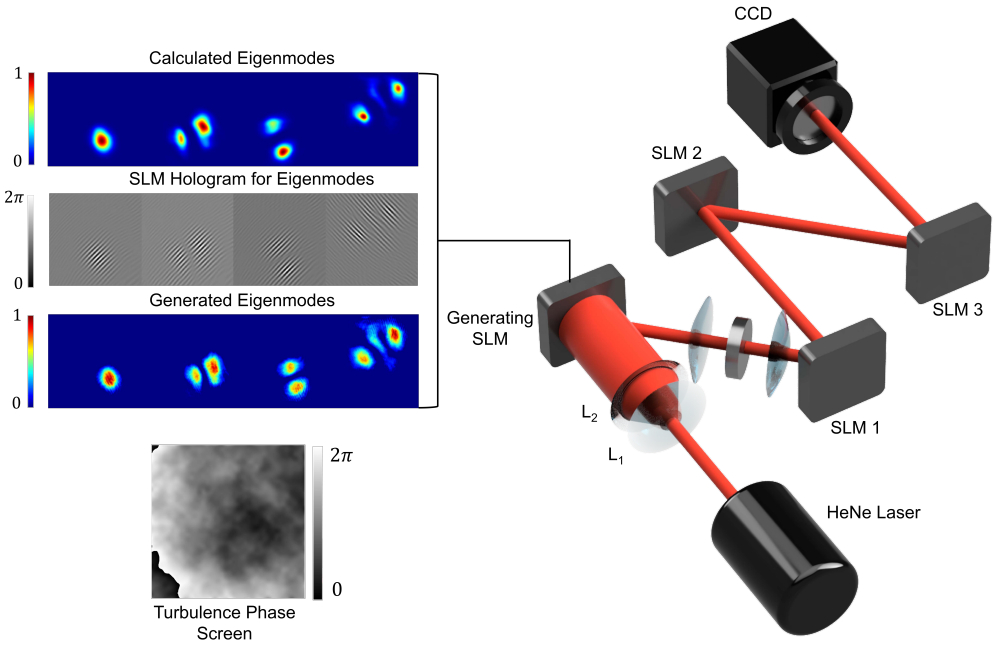


FIGURE 5.8: **Experimental Setup.** Lenses L_1 and L_2 expand and collimate a laser beam onto an SLM on which a phase-only hologram of the initial beam is displayed, but implementing amplitude and phase control by complex amplitude modulation. The ideal, turbulence-free beam is generated at this plane and subsequently propagates through three turbulent screens which are also displayed on SLMs, each followed by 1 m of free-space propagation. The final aberrated field is captured on a CCD to image its intensity. The panels on the right show examples of the desired eigenmodes (Calculated Eigenmodes), the holograms to create them, and the measured eigenmodes without any turbulence or propagation (Generated Eigenmodes).

matrix transform method [145] and displayed on the (phase-only) SLMs. The intensity of the perturbed field was then detected and measured on a camera (CCD). The panels on the left of the experimental setup in Fig. 5.8 show four examples of the desired (calculated) eigenmodes, the holograms to create them by complex amplitude modulation, and the experimental validation that without any turbulence or propagation, that they are created (generated eigenmodes) with high fidelity (bottom panel).

Our setup differs from conventional laboratory simulations of turbulence in that we are able to mimic a thick path, from weak to strong turbulence, whereas often only a single phase screen is used, allowing only weak turbulence to be tested. Using our setup, we studied an effective real-world channel of $L = 100$ m, at our wavlength of $\lambda = 633$ nm and with Rytov variances of $\sigma_R^2 = 1.5$, 1 and 0.5, corresponding (respectively) to strong, medium and weak turbulence, with Fried parameters (r_0) of 0.47 mm, 0.62 mm and 0.93 mm, respectively. We required three screens for each turbulence strength, separated by a distance of 33.3 m, each with effective Fried parameters $r_{0,s} =$ 0.9 mm, 1.2 mm and 1.8 mm while maintaining a Rytov variance in each slab (segment of the channel) to be smaller than 0.9, 0.6 and 0.3, respectively. This channel was simulated on the setup shown in Fig. 5.8 using the Fresnel scaling procedure [148], allowing a long path to be generated within laboratory

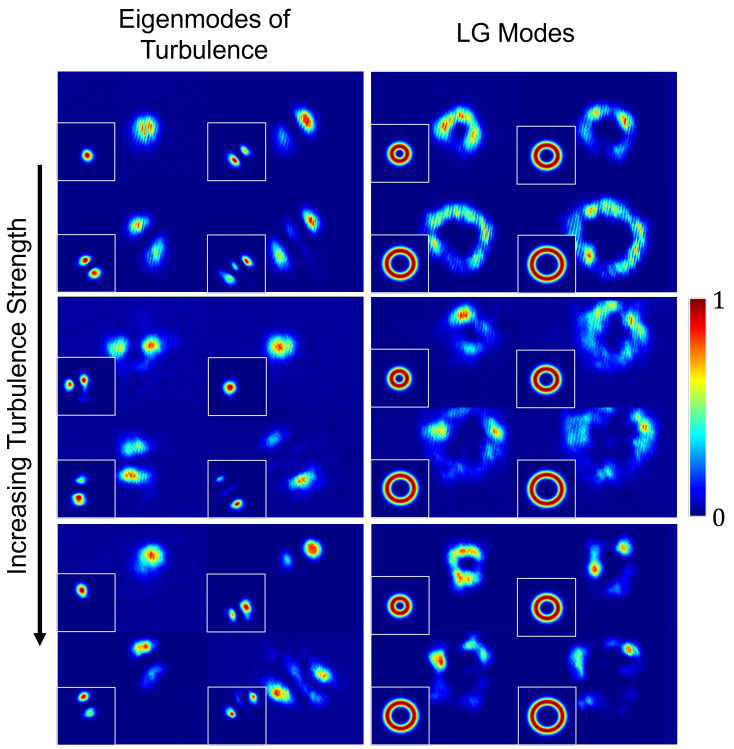


FIGURE 5.9: **Experimental Eigenmodes.** In the left column we see the measured intensities of the eigenmodes of turbulence after propagating through the experimental setup. The results show eigenmodes of weak, medium and strong turbulence. In the right column we see the measured intensities of OAM modes after propagating through the same experimental setup with the same turbulence phase screens for comparison. The insets show the initial input mode. Weak turbulence was characterised by $\sigma_R^2 = 0.5$ and $r_0 = 1.8$ mm, medium turbulence by $\sigma_R^2 = 1$ and $r_0 = 1.2$ mm and strong turbulence by $\sigma_R^2 = 1.5$ and $r_0 = 0.91$ mm

distances. The scaling factors were chosen to be: $\alpha_x = \alpha_{x'} = \sqrt{0.03} \approx 0.173$ and $\alpha_z = 0.03$. This corresponded to a total path length of $L' = 3$ m and segment Fried parameters of $r_{0,s} = 0.081$ mm, 0.11 mm and 0.16 mm (see Appendix for details).

The results of OAM and the eigenmodes for weak, medium and strong turbulence are shown in Fig. 5.9. The collage shows the final measured eigenmodes after the channel, with the insets showing the initial mode as prepared prior to the channel. The robustness of the eigenmodes is clearly evident, in contrast to the highly distorted OAM modes. While there are slight intensity changes for the eigenmodes of turbulence, these are extremely small in comparison to the intensity fluctuations experienced by the OAM modes. The level of distortion in the eigenmodes does seem more profound for the weak turbulence case. However, each turbulence strength constitutes a different realisation of turbulence and so this cannot be taken as a general trend until a large number of eigenmodes for various realisations of turbulence have been generated an analysed.

5.4.1 Fresnel Scaling

Some channel parameters, such as path length, are highly restricted in the laboratory setting. This presents an apparent difficulty to experimentally verifying the eigenmodes. However, a scaling procedure exists [148] which allows us to verify real-world channels in the laboratory. This procedure is presented below.

The Fresnel integral for the full (real-world) channel of length L is

$$\mathrm{U}_f(\mathbf{r}, L) = \frac{\exp(ikL)}{i\lambda L} \int \mathrm{d}^2\mathbf{r}' \, \mathrm{U}_i(\mathbf{r}') \exp\left(\frac{i\pi}{\lambda L}\|\mathbf{r} - \mathbf{r}'\|^2\right). \tag{5.13}$$

We then apply the following scaling parameters: $\mathbf{r}_{\text{lab}} = \alpha_r \mathbf{r}$, $\mathbf{r}'_{\text{lab}} = \alpha_{r'}\mathbf{r}'$ and $L' = \alpha_z L$, where $\mathbf{r}_{\text{lab}}$ and $\mathbf{r}'_{\text{lab}}$ are the coordinates used in the experiment. The diffraction integral becomes

$$\begin{aligned}\mathrm{U}_f\left(\frac{\mathbf{r}_{\text{lab}}}{\alpha_r}, L'\right) = \frac{\exp\left(ikL'/\alpha_z\right)}{i\alpha_{r'}^2\lambda L'} \int \mathrm{d}^2\mathbf{r}'_{\text{lab}} \, \mathrm{U}_i\left(\frac{\mathbf{r}'_{\text{lab}}}{\alpha_{r'}}\right) \times \\ \times \exp\left(\frac{i\pi\alpha_z}{\lambda L'}\left\|\frac{\mathbf{r}_{\text{lab}}}{\alpha_r} - \frac{\mathbf{r}'_{\text{lab}}}{\alpha_{r'}}\right\|^2\right).\end{aligned} \tag{5.14}$$

To keep the diffraction equivalent with these scaled coordinates we require the Fresnel number

$$F = \frac{\pi D_i D_f}{4\lambda L} \tag{5.15}$$

to be the same in both the full and scaled-down cases, where D_i and D_f are the aperture diameters in the initial and final planes, respectively. This sets $\alpha_r\alpha_{r'} = \alpha_z$ and the diffraction integral becomes

$$\begin{aligned}\frac{\exp\left(ikL'\left(1 - \frac{1}{\alpha_z}\right)\right)}{\alpha_r}\mathrm{U}_f\left(\frac{\mathbf{r}_{\text{lab}}}{\alpha_r}\right) = \exp\left(-\frac{i\pi r_{\text{lab}}^2}{\lambda f_r}\right)\frac{\exp\left(ikL'\right)}{i\lambda L'} \times \\ \times \int \mathrm{d}^2\mathbf{r}'_{\text{lab}} \; \mathrm{U}_i\left(\frac{\mathbf{r}'_{\text{lab}}}{\alpha_{r'}}\right)\exp\left(-\frac{\pi(r'_{\text{lab}})^2}{\lambda f_{r'}}\right)\exp\left(\frac{i\pi}{\lambda L'}\|\mathbf{r}_{\text{lab}} - \mathbf{r}'_{\text{lab}}\|\right),\end{aligned} \tag{5.16}$$

where

$$f_r = \frac{L'}{1 - \alpha_{r'}/\alpha_r}, \tag{5.17}$$

$$f_{r'} = \frac{L'}{1 - \alpha_r/\alpha_{r'}}. \tag{5.18}$$

Setting $\alpha_r = \alpha_{r'}$ means that the final and initial planes have the same size in the laboratory setting and $f_{r,r'} \to \infty$. Ignoring constant phase factors which

arise due to scaling, the final Fresnel integral becomes

$$\mathrm{U}_f\left(\frac{\mathbf{r}_{\mathrm{lab}}}{\alpha_r}\right) = \frac{\alpha_r \exp(ikL')}{i\lambda L'} \int \mathrm{d}^2\mathbf{r}'_{\mathrm{lab}}\ \mathrm{U}_i\left(\frac{\mathbf{r}'_{\mathrm{lab}}}{\alpha_{r'}}\right) \times \exp\left(\frac{i\pi}{\lambda L'}\left\|\mathbf{r}_{\mathrm{lab}} - \mathbf{r}'_{\mathrm{lab}}\right\|\right). \tag{5.19}$$

5.5 Discussion

We have outlined how to find the eigenmodes of a turbulent path, and demonstrated it with a laboratory-based split-step example both numerically and experimentally. These modes are eigenmodes in their truest sense, i.e,. they are fixed under the action of the channel. Importantly, our approach works even when the medium is long and the aberration strong, a regime where traditional adaptive optics often fails (beyond a Rytov variance of order 1) [149, 150].

A natural feature of the eigenmodes is that they are channel specific. To be useful in a real-world setting, the transmission should be faster than the coherence time of the turbulence. For typical turbulence conditions this is always true, with the atmosphere changing on millisecond time scales (typically $1 - 10$ ms), whereas the transport of light across km length scales is on the order of nanoseconds. The turbulence thus appears frozen, and numerical simulations on singular value modes have shown that they outperform adaptive solutions even in dynamic turbulence [151]. The time frames of acquiring the information to deduce the eigenmodes can be very fast. A tomography of the channel can be done by modal decomposition in any basis [9] with projective holograms, which with digital micro-mirror devices (DMDs) and photodiodes can certainly be done on millisecond time scales. This can be improved down to microseconds (limited by the response of fast photodiodes) if the projective holograms are hardcoded, such as on a diffractive optical element or metasurface, possible because the channel does not have to be probed in the basis of eigenmodes. Further, one can surmise that machine learning would be ideally suited to the task of anticipating the new eigenmodes in a dynamical system given the prior set, certainly appealing if the conditions are slowly changing. We take some confidence from the fact that such channel analysis is needed in MIMO as well as in singular value decomposition approaches, both of which have been applied to non-turbulence studies already with success. Nevertheless, it is a challenge that should not be downplayed, and is certainly deserving of a full experimental study. We point out that turbulence was used here only as an extreme example, whereas the formulation of the idea is such that it will work for any long path in a complex media, for instance, turbid, underwater, optical fibre or thermally aberrated paths, all of which may change more slowly or not at all. Our analysis only considered scalar modes, whereas it is clear that vectorial superpositions would also be eigenmodes of this channel. In this way the invariance of the inhomogeneity of vectorial light in complex channels [71]

could be generalised to the invariance of all properties of the field, an appealing notion for energy transport and imaging through complex systems.

5.6 Conclusion

The search for robust states of structured light in noisy channels is a pressing challenge, promising enhanced channel capacity and reach. Here, using free-space and atmospheric turbulence as our example, we have outlined a theoretical approach to finding the complex forms of structured light which are invariant under propagation through the atmosphere, the true eigenmodes of turbulence, and confirmed its validity both numerically and experimentally. These exotically structured eigenmodes need no corrective procedures, are naturally devoid of deleterious effects and are valid over any path length in the medium. Our approach offers a new pathway for exploiting structured light in turbulence, and can be easily extended to other noisy channels, such as underwater and optical fibre.

Chapter 6

Numerical Orthogonality Considerations

It has now been demonstrated that by obtaining a sufficient understanding of the Physics governing the behaviour of a complex, aberrated medium, it is possible to tailor structured light fields so that they propagate unchanged through that medium. In this work we have demonstrated this using a tilted spherical lens and atmospheric turbulence as examples of such channels. In both cases, the approach was to define an operator that sufficiently describes the action of the channel on the input state as to allow us to correctly calculate the output state. Once the operator is obtained, it is then a matter of finding the eigenstates or eigenmodes of that operator. A key but subtle point that was not discussed in depth is that the states with which we are dealing and the operator which describes the action of the channel must be specified using a basis. We are able to choose from a large variety of bases: the Hermite Gaussian beams were used as a basis for the tilted lens, while position/pixels were used for atmospheric turbulence. In both cases, these bases were chosen as we were able to most easily express the perturbations (and by extension the action) of the channel in the respective bases. This allowed us to easily determine the eigenmodes of those channels.

While choosing a basis that results from our initial definition and understanding of the channel is useful for determining the eigenmodes, it can make the application and use of these eigenmodes more challenging. The key property of structured light fields that allows for their use in techniques such as mode division multiplexing, modal decomposition and modal imaging (to name a few) is that each mode family forms a complete, orthonormal basis. This means that if one is given any arbitrary light field $|\Psi\rangle$, one can describe this arbitrary field as a linear superposition of these modes,

$$|\Psi\rangle = \sum_{n,m} c_{nm}^{HG} |HG_{nm}\rangle = \sum_{l,p} c_{lp}^{LG} |LG_{lp}\rangle = \sum_{i,j} c_{ij} |x_i, y_j\rangle \ . \tag{6.1}$$

Within this linear superposition, every mode in the basis is orthogonal to every other mode and thus can be separated out and its contribution $c_{nm}^{HG}/c_{lp}^{LG}/c_{ij}$ to the overall field can be uniquely and exactly determined.

There are a theoretically infinite number of basis modes in each of the mode families mentioned, and so there is generally no issue with switching between different bases when performing our calculations. However, when

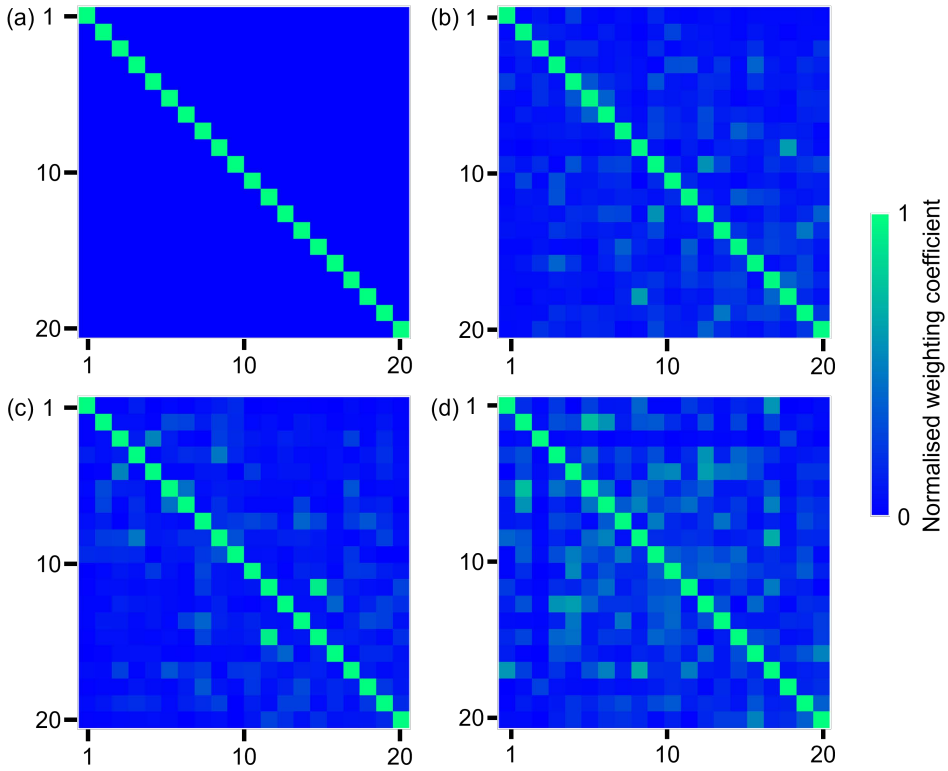


FIGURE 6.1: **Orthogonality of Pixel Basis Eigenmodes.** Here we the crosstalk matrices of several different mode-sets. (a) The ideal crosstalk matrix between a set of orthogonal modes that remain invariant through a medium. (b) Crosstalk matrices between eigenmodes calculated for a weak turbulent channel ($\sigma_R^2 < 1$). (c) Crosstalk matrices between eigenmodes calculated for a medium turbulent channel ($\sigma_R^2 \approx 1$). (b) Crosstalk matrices between eigenmodes calculated for a strong turbulent channel ($\sigma_R^2 > 1$).

implementing these eigenmodes, we are limited to only a finite number of basis elements. This restriction results from practical considerations (such as the number of pixels on the SLM screen on which we wish to programme our turbulence phase screen), or the time taken to compute the operator limiting us to only a set number of calculations (such as when needing to calculate the weighting coefficient of HG modes). In certain cases, the choice of basis may affect the orthogonality of the numerically calculated eigenmodes as we are not able to access the entire basis and not faithfully reproduce the desired eigenmode with the finite number of basis elements available. The choice of basis can also make understanding the behaviour and any underlying structure present in the set of eigenmodes easier, as the dynamics and properties of certain basis modes are more or less understood depending on the context.

A prime example of this are the eigenmodes of turbulence calculated in the pixel-basis. We may check the orthogonality of the eigenmodes, such as those obtained in the previous chapter, using a crosstalk matrix. In such a computation, we compute the overlap integral between each and every basis mode. For example, we set $|\Psi\rangle = |HG_{n'm'}\rangle$ and determine the overlap coefficient with every $|HG_{nm}\rangle$. If the modes are orthogonal, the overlap integral

should only be non-zero if the mode is being overlapped with itself,

$$c_{nm}^{HG} = \langle HG_{nm} | HG_{n'm'} \rangle = \delta_{n,n'}\delta_{m,m'}\,, \tag{6.2}$$

where $\delta(\cdot)$ is the Dirac delta function. A similar relation holds for the LG, position and pixel bases. From this, we expect that the crosstalk matrix would be a perfect identity matrix with the only non-zero elements along the diagonal as shown in Figure 6.1 (a). In Figure 6.1, we see that the eigenmodes of (b) weak, (c) medium and (d) strong turbulence all exhibit non-zero elements along the diagonal, but also many non-zero elements off the diagonal. This is evidence of non-orthogonal behaviour and, since these imperfections will only be amplified due to experimental error, this will make the eigenmodes very difficult to implement in real-world applications.

The pixel basis is used because it is how we describe the statistics and the phase aberration imparted on the beam. The downsides are that we may only use a finite number of pixels which can only cover a set region of space leading to the truncation of the eigenmodes, breaking the orthogonality. The pixels themselves also have a non-zero size, and thus we only know the modes to an accuracy given by the size of each pixel, which will additionally break the orthogonality. We will therefore try to move from the pixel basis to another, which will hopefully allow us to determine eigenmodes that exhibit much stronger orthogonality even with the numerical restrictions we typically encounter. For inspiration in finding this new basis, we turn to work that has been done which gives evidence for the atmosphere giving and taking orbital angular momentum (OAM) from a structured light beam [115]. OAM forms part of the LG basis and so we will transform our pixel basis operators to the OAM basis and then recalculate the eigenmodes in the new basis. Because the OAM basis consists of completely continuous functions that are analytically defined over all of space, we expect the use of this new basis to overcome many of the issues encountered when using the pixel basis.

6.1 Phase Aberrations in the OAM Basis

In the position basis, we describe the phase perturbations induced by the refractive index fluctuations as simply an aberrated phase $e^{i\Theta(x,y)}$ multiplied onto the incident field. It assigns, to every point in space, a phase value that represents how accelerated or delayed the phase of the incident beam will be when it interacts with the turbulent medium. Its action therefore takes in an input state $|\mathbf{x}_j\rangle$ (position or pixel) and outputs the same state multiplied by a phase given by $e^{i\Theta(\mathbf{x}_i)}$. We can represent this as an operator as follows,

$$\hat{A} = \int |\mathbf{x}\rangle \langle \mathbf{x}| \, e^{i\Theta(\mathbf{x})} \mathrm{d}^2 x \tag{6.3}$$

Such that for a given input state $|\mathbf{y}\rangle$,

$$\begin{aligned}\hat{A}\,|\mathbf{y}\rangle &= \int |\mathbf{x}\rangle\,\langle\mathbf{x}|\,e^{i\Theta(\mathbf{x})}\,|\mathbf{y}\rangle\,\mathrm{d}^2x \\ &= \int |\mathbf{x}\rangle\,\langle\mathbf{x}|\mathbf{y}\rangle\,e^{i\Theta(\mathbf{x})}\mathrm{d}^2x \\ &= \int |\mathbf{x}\rangle\,\delta(\mathbf{x}-\mathbf{y})e^{i\Theta(\mathbf{x})}\mathrm{d}^2x \\ &= e^{i\Theta(\mathbf{y})}\,|\mathbf{y}\rangle \end{aligned} \tag{6.4}$$

In order to perform a change of basis, we will make use of the fact that the OAM basis is complete, meaning that,

$$\sum_l |l\rangle\,\langle l| = \mathbf{I}\,, \tag{6.5}$$

where $\mathbf{I}$ is the identity matrix. Since multiplication by the identity matrix does not change a matrix, we can multiply our phase aberration operator $\hat{A}$ by the identity matrix as follows,

$$\begin{aligned}\hat{A} &= \int |\mathbf{x}\rangle\,\langle\mathbf{x}|\,e^{i\Theta(\mathbf{x})}\mathrm{d}^2x \\ &= \int \mathbf{I}\,|\mathbf{x}\rangle\,\langle\mathbf{x}|\,\mathbf{I}e^{i\Theta(\mathbf{x})}\mathrm{d}^2x \\ &= \int \left(\sum_{l_1} |l_1\rangle\,\langle l_1|\right) |\mathbf{x}\rangle\,\langle\mathbf{x}|\left(\sum_{l_2} |l_2\rangle\,\langle l_2|\right) e^{i\Theta(\mathbf{x})}\mathrm{d}^2x \\ &= \int \sum_{l_1}\sum_{l_2} |l_1\rangle\,\langle l_1|\mathbf{x}_j\rangle\,\langle\mathbf{x}_j|l_2\rangle\,\langle l_2|\,e^{i\Theta(\mathbf{x})}\mathrm{d}^2x \end{aligned} \tag{6.6}$$

Since the inner products $\langle l_1|\mathbf{x}_j\rangle$ and $\langle\mathbf{x}_j|l_2\rangle$ are the projections of the OAM states into the position basis, they may be expressed as their respective LG functions,

$$\langle l_1|\mathbf{x}\rangle = LG^*_{l_1}(\mathbf{x}) \tag{6.7}$$

$$\langle\mathbf{x}|l_2\rangle = LG_{l_2}(\mathbf{x}) \tag{6.8}$$

Using these relations, Equation 6.6 becomes,

$$\hat{A} = \sum_{l_1}\sum_{l_2}\int LG^*_{l_1}(\mathbf{x})LG_{l_2}(\mathbf{x})e^{i\Theta(\mathbf{x})}\mathrm{d}^2x\,|l_1\rangle\,\langle l_2| = \sum_{l_1}\sum_{l_2} a^{l_1}_{l_2}\,|l_1\rangle\,\langle l_2|\,. \tag{6.9}$$

Where we define the coefficient,

$$a^{l_1}_{l_2} = \int LG^*_{l_1}(\mathbf{x})LG_{l_2}(\mathbf{x})e^{i\Theta(\mathbf{x})}\mathrm{d}^2x \tag{6.10}$$

We interpret this operator as taking in an input OAM eigenstate/basis state $|l_2\rangle$, aberrating it with the phase aberration given by $e^{i\Theta(\mathbf{x})}$ and then checking its overlap with the basis states at the output $|l_1\rangle$. The coefficient $a_{l_2}^{l_1}$ gives the degree to which an input basis mode is aberrated at the output. This operator can be easily calculated and was calculated with 200 basis modes which is shown in Figures 6.2 for (a) weak and (d) strong turbulence, where we have plotted $\hat{A}\hat{A}^{\dagger}$. We see only non-zero elements along the diagonal which closely matches the behaviour of a unitary operator. This is a good indication of the accuracy of the operator as we know the action of turbulence as a whole is unitary. We also see the absolute value squared ((b) and (e)) and phase ((c) and (f)) of the weighting coefficients that would be used to calculate the eigenmodes of this operator from superpositions of the basis modes. The mode order is determined by the eigenvalue for each eigenmode, going from largest to smallest absolute value. We see from the absolute value squared of the coefficients that in general, high order eigenmodes are superpositions of basis modes with larger OAM values $|l|$. Upon comparison between the weak and strong aberrations, we see that there is a greater spread in the contributions from the basis modes for the eigenmodes in the strong case. This is to be expected as stronger turbulence would impart, on average, a larger spread of OAM onto an incident beam. The first few eigenmodes of this operator, for weak and strong phase aberrations are shown in Figure 6.3. Interestingly, we see that the profile of these eigenmodes have a very similar intensity profile of two interfering beams, with regularly spaced intensity fringes.

6.2 Propagation in the OAM Basis

The propagation operator can by inferred from the paraxial Huygens-Fresnel diffraction integral. We express the operator mathematically as,

$$\hat{G}(z) = \iint g(\mathbf{x}, \mathbf{x}'; z) \left|\mathbf{x}'\right\rangle \left\langle \mathbf{x}\right| \mathrm{d}^2x \mathrm{d}^2x' \,, \tag{6.11}$$

where $g(\mathbf{x}, \mathbf{x}'; z)$ is the paraxial free space Green's function given by,

$$g(\mathbf{x}, \mathbf{x}'; z) = \frac{1}{i\lambda z} e^{\frac{i\pi}{\lambda z}|\mathbf{x}-\mathbf{x}'|} \,. \tag{6.12}$$

The action of the operator is to take an input state, which is a point in the input plane $\mathbf{x}$, and maps its plane wave contributions to all of the output states which are all points in the output plane $\mathbf{x}'$. An output state is therefore a sum over all the plane wave contributions from each input state. To perform the change of basis, we take advantage of the same completeness relation as

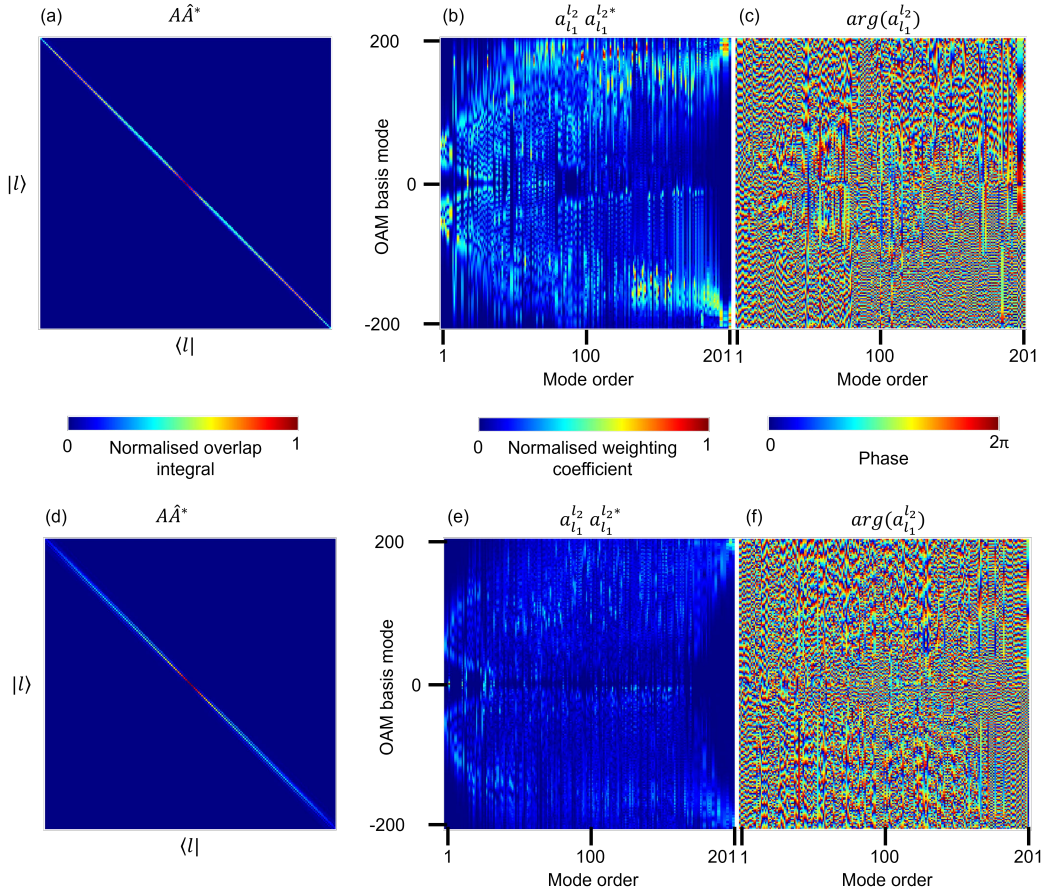


FIGURE 6.2: **Phase Aberration Operator.** The phase aberration operator in the OAM basis multiplied by its conjugate is shown for (a) weak and (d) strong turbulence. This shows us that the phase aberration operator is unitary. The drop off in intensity from the centre indicates that the coefficients are getting smaller as the modes they are acting on get larger. This can be explained by noting that we first defined the phase aberration operator in the pixel basis, which has a limited numerical aperture that will truncate modes of very high order. The (c) and (e) show absolute value squared and the (b) and (f) phase of the coefficients calculated to form eigenmodes of the weak and strong phase aberration operator from superpositions of the basis modes.

before, given by Equation 6.5. The procedure is as follows,

$$\begin{aligned}
\hat{G}(z) &= \iint g(\mathbf{x},\mathbf{x}';z)\,|\mathbf{x}'\rangle\,\langle\mathbf{x}|\,\mathrm{d}^2x\mathrm{d}^2x' \\
&= \iint g(\mathbf{x},\mathbf{x}';z)\mathbf{I}\,|\mathbf{x}'\rangle\,\langle\mathbf{x}|\,\mathbf{I}\mathrm{d}^2x\mathrm{d}^2x' \\
&= \iint g(\mathbf{x},\mathbf{x}';z)\left(\sum_{l_1}|l_1\rangle\,\langle l_1|\right)|\mathbf{x}'\rangle\,\langle\mathbf{x}|\left(\sum_{l_2}|l_2\rangle\,\langle l_2|\right)\mathrm{d}^2x\mathrm{d}^2x' \\
&= \iint \sum_{l_1}\sum_{l_2} g(\mathbf{x},\mathbf{x}';z)\,|l_1\rangle\,\langle l_1|\mathbf{x}'\rangle\,\langle\mathbf{x}|l_2\rangle\,\langle l_2|\,\mathrm{d}^2x\mathrm{d}^2x'\,. \qquad (6.13)
\end{aligned}$$

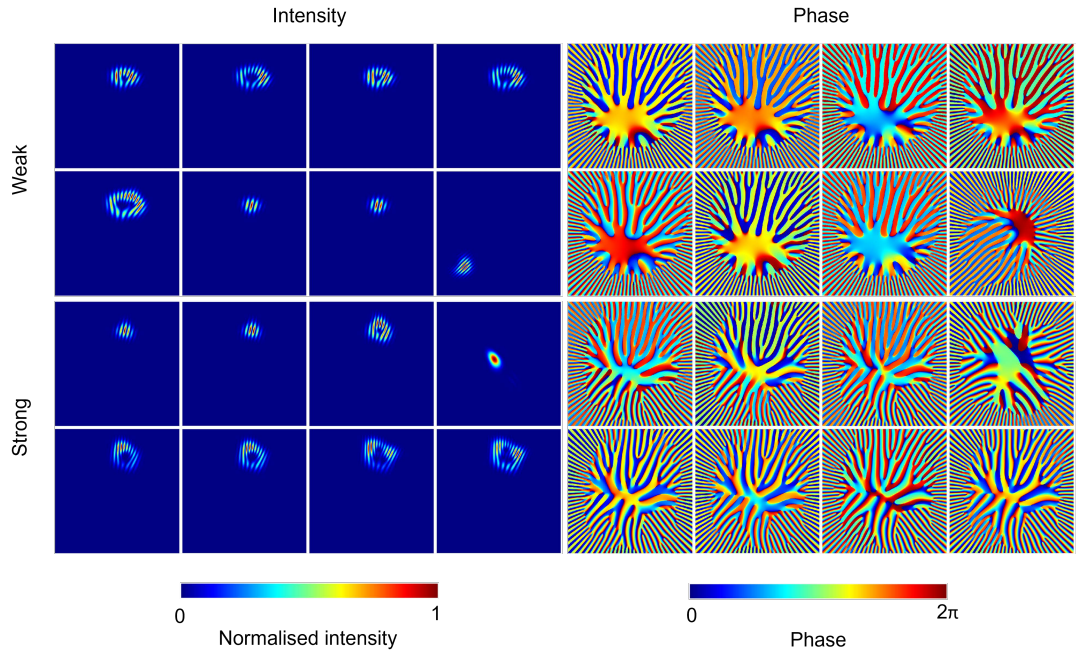


FIGURE 6.3: **Eigenmodes of the Phase Aberration Operator.** Here we see the intensity (left) and phase (right) profiles of the eigenmodes of the phase aberration operator.

We see here again the same terms as in Equations 6.7 and 6.8, allowing us to write,

$$\begin{aligned}\hat{G}(z) &= \iint \sum_{l_1}\sum_{l_2} g(\mathbf{x},\mathbf{x}';z)\,|l_1\rangle\, LG^*_{l_1}(\mathbf{x}')LG_{l_2}(\mathbf{x})\,|l_2\rangle\,\mathrm{d}^2x\mathrm{d}^2x' \\ &= \sum_{l_1}\sum_{l_2}|l_1\rangle\,\langle l_2| \iint g(\mathbf{x},\mathbf{x}';z)LG_{l_2}(\mathbf{x})\mathrm{d}^2xLG^*_{l_1}(\mathbf{x}')\mathrm{d}^2x'\,. \end{aligned} \tag{6.14}$$

For ease of visibility and to break down the action of the new operator more clearly, we may define the following coefficients,

$$b_{l_2}(\mathbf{x}') = \int g(\mathbf{x},\mathbf{x}';z)LG_{l_2}(\mathbf{x})\mathrm{d}^2x' \tag{6.15}$$

$$c^{l_2}_{l_1} = \int b_{l_2}(\mathbf{x}')LG_{l_1}(\mathbf{x}')\mathrm{d}^2x\,, \tag{6.16}$$

so that the final operator looks like,

$$\sum_{l_1}\sum_{l_2} c^{l_2}_{l_1}\,|l_1\rangle\,\langle l_2|\,. \tag{6.17}$$

The first coefficient $b_{l_2}(\mathbf{x}')$, given by Equation 6.15, describes the spatial profile of a basis mode once it has been propagated to the output plane. The second coefficient $c^{l_2}_{l_1}$, given by Equation 6.16, quantifies the overlap between the propagated basis mode and the basis modes of the output plane. The

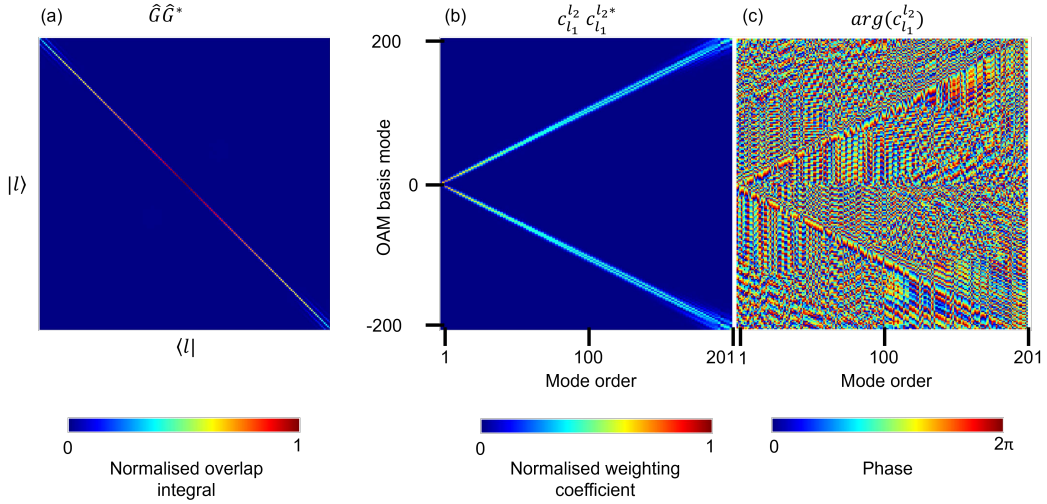


FIGURE 6.4: **Propagation Operator.** (a) The propagation operator in the OAM basis multiplied by its conjugate. This shows us that the propagation operator is unitary. The drop of in intensity from the centre indicates that the coefficients are getting smaller as the modes they are acting get larger. This can be explained by noting that we first defined the propagation operator in the pixel basis, which as a limited numerical aperture that will truncate modes of very high order. The (b) absolute value squared and the (c) phase of the coefficients calculated to form eigenmodes of the propagation operator from superpositions of the basis modes

operator is represented visually in Figure 6.4. Figure 6.4 (a) shows the operator multiplied by its conjugate which returns a matrix with nonzero entries only along the diagonal. This indicates that the operator is close to unitary, with the fall off in values along the diagonal possibly being attributed to the fact that the position basis operator is limited in size, and so as we increase the OAM and move to a larger basis mode, we cannot capture all of their intensity. This is not necessarily bad but does place numerical limits on the accuracy of our operator. We see that its intensity distribution is broader than that of the phase aberration operators. This can be understood by observing that the for the finite numerical aperture used in our simulations, the mode mixing/crosstalk induced by the phase aberration is significantly higher that that induced by propagation in the measured in the same basis. Figure 6.4 (b) and (c) show the coefficients for the eigenmodes of the propagation. There is a clear symmetry across the central line, indicating that the modes are superpositions of basis OAM modes with conjugate OAM. This is clearly seen when we plot the propagation eigenmodes' intensity and phase profiles as shown in Figure 6.5. The eigenmodes in Figure 6.5 are typical superpositions of antisymmetric Laguerre Gaussian (LG) modes. This is a mode made up of two LG modes with equal but opposite OAM. Since we know from Chapter 1 that LG modes are eigenmodes of free space, and from Chapter 3 that modes of the same order gain equal propagation and Gouy-phase, these superpositions will remain unchanged in propagation and thus we can be confident that our OAM basis operator is accurate in modelling propagation as it returns modes that are indeed invariant to the action of the operator. It is also

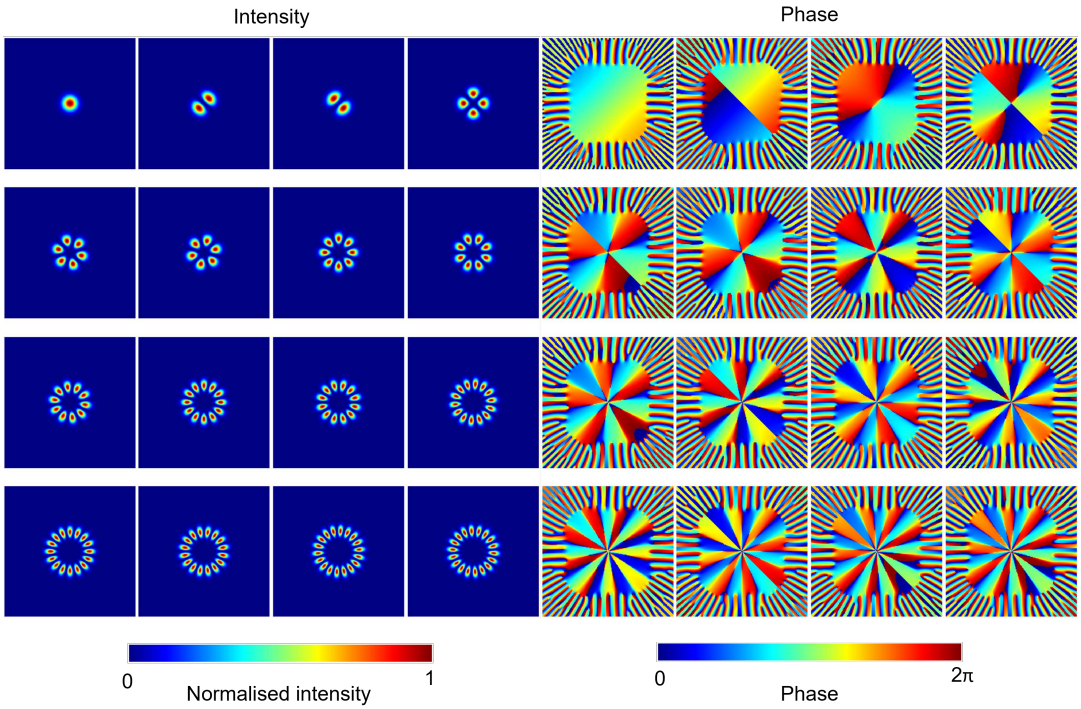


FIGURE 6.5: **Eigenmodes of Propagation.** Here we see the intensity (left) and phase (right) profiles of the eigenmodes of the propagation.

worth noting that these modes have the same intensity as the linearly polarised (LP) modes which are the eigenmodes of propagation through some forms of optical fibre.

6.3 Eigenmodes of Turbulence in the OAM Basis

Now that we have obtained an operator for the phase aberration $\hat{A}$ and an operator for free space propagation $\hat{G}$, we can obtain the operator for a turbulent channel by simply combining the two operators,

$$\hat{T} = \hat{G}\hat{A}\,. \tag{6.18}$$

We can then use the same procedure as before to determine the eigenmodes of turbulence, but now they are calculated in the OAM basis and not the pixel basis. The operator is represented visually in Figure 6.6 for a strong turbulent channel. Figure 6.6 (a) again shows the operator multiplied by its conjugate. It is a diagonal matrix as expected, as both $\hat{G}$ and $\hat{A}$ also returned a diagonal matrix under this representation. This shows that our turbulence operator exhibits close to unitary behaviour, with higher order eigenmodes only losing contributions due to the spatial limitations of the pixel basis from which these operators were derived. However, we see that the values of the elements near the centre of the matrix are all approximately equal. If we only used the lower order eigenmodes, we should see the channel behave in a unitary manner. This is good as atmospheric turbulence is known to be

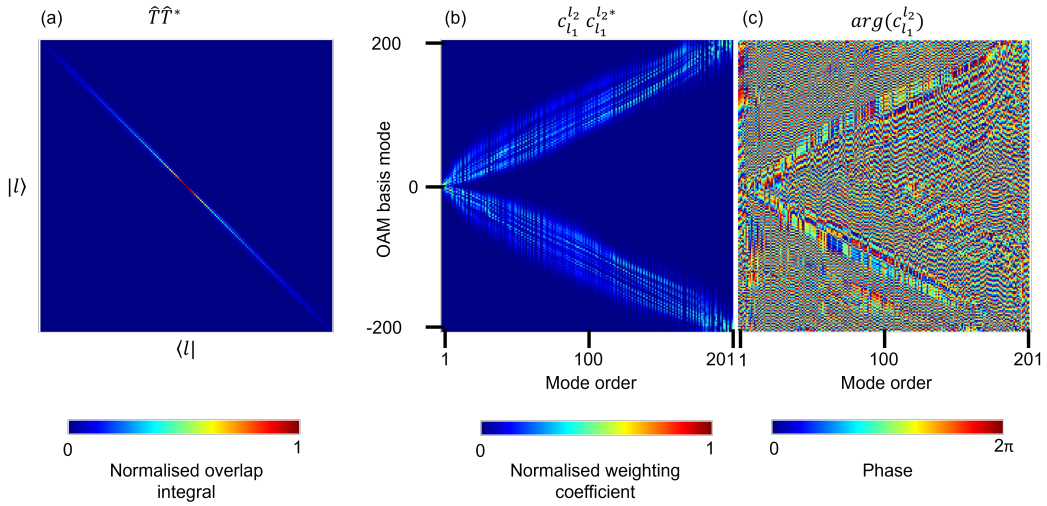


FIGURE 6.6: **Turbulence Operator.** (a) The turbulence operator in the OAM basis multiplied by its conjugate. This shows us that the turbulence operator is unitary. The drop off in intensity from the centre indicates that the coefficients are getting smaller as the modes they are acting on get larger. This is a result of effects seen in the phase aberration and propagation operators and one of the downsides of being limited to the pixel basis to define the initial aberration and propagation operators. The (b) absolute value squared and the (c) phase of the coefficients calculated to form eigenmodes of the turbulence operator from superpositions of the basis modes

a unitary channel. This is already a significant improvement over the pixel basis calculations. Figure 6.6 (b) and (c) show the absolute value and phase of the weighting coefficient of the eigenmodes. Similarly to the propagation operator, we see a symmetry across the $l = 0$ OAM basis mode. This is to be expected as it is most likely inherited from the propagation operator. The intensity and phase profiles of the eigenmodes for this turbulent channel are shown in Figure 6.7. Similarly to the eigenmodes found in the previous chapter, these modes look like heavily aberrated eigenmodes of propagation. However, these modes are in fact robust through the turbulent channel as shown in Chapter 5.

The orthogonality of these modes can be compared to the orthogonality of the pixel basis eigenmodes both calculated for an identical channel with identical phase aberrations. The crosstalk matrices for both approaches are shown in Figure 6.8. It is clear that the eigenmodes calculated in the OAM basis, though not perfect, show much stronger orthogonality when compared to the eigenmodes calculated in the pixel basis.

6.4 Conclusion

The results from this chapter clearly show that the properties of the eigenmodes calculated in the pixel basis make them non-optimal for the many applications for optical eigenmodes. They must be calculated from an operator that is not unitary and thus not accurately capturing the Physics of the medium through which they propagate. They are not orthogonal and

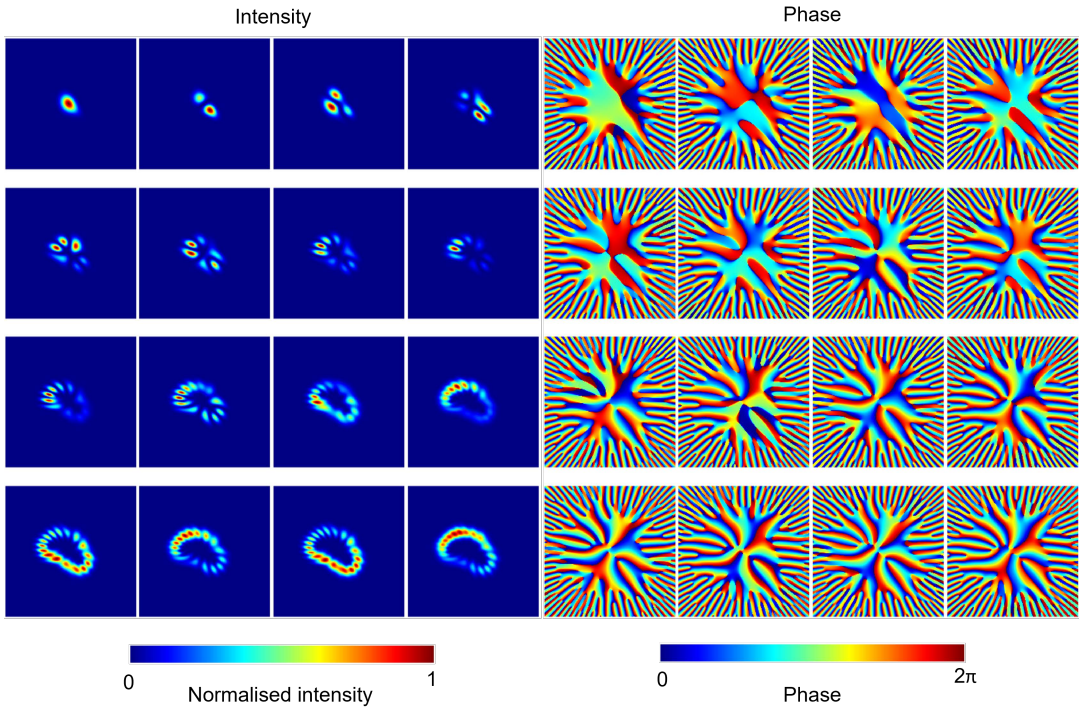


FIGURE 6.7: **Turbulence Eigenmodes.** Here we see the intensity (left) and phase (right) profiles of the eigenmodes of the strong turbulent channel.

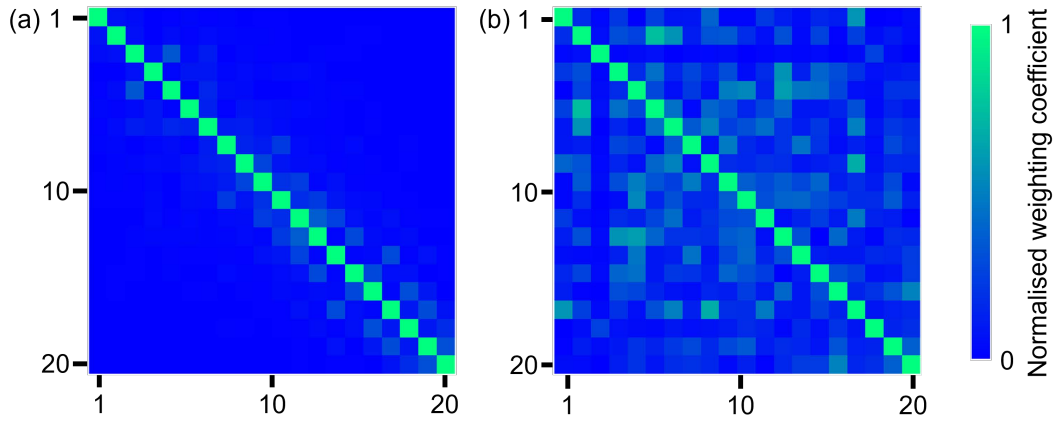


FIGURE 6.8: **Crosstalk of the OAM basis operator.** (a) The crosstalk matrix between the calculated eigenmodes in the OAM basis for a strong turbulent channel. (b) The crosstalk matrix between the calculated eigenmodes if the pixel basis for an identical strong turbulent channel. We see significantly less crosstalk for the modes in the OAM basis. We only show 20 modes in this Figure but this same trend holds for all 200 basis modes calculated earlier in the chapter.

thus will be very challenging to implement for their many proposed applications. However, both of these issues are overcome if we simply perform a change of basis to the OAM basis. The eigenmodes calculated in this basis are derived from an operator that is unitary, and so we can be confident

that it is more closely modelling the Physics of the medium. These eigenmodes also exhibit significantly stronger orthogonality, meaning they will be vastly more effective when being implemented in optical communications, imaging, measurement and sensing.

Bibliography

1. Griffiths, D. J. *Introduction to electrodynamics* (Pearson, 2013).
2. Goodman, J. W. *Introduction to Fourier Optics* ISBN: 0-07-02425402 (McGraw-Hill, 1996).
3. Rosales-Guzmán, C. & Forbes, A. *How to shape light with spatial light modulators* 57. ISBN: 9781510613027 (SPIE Press).
4. Arrizón, V., Ruiz, U., Carrada, R. & González, L. A. Pixelated phase computer holograms for the accurate encoding of scalar complex fields. *JOSA A* **24,** 3500–3507 (2007).
5. Bansal, V. & Saggau, P. Digital micromirror devices: principles and applications in imaging. *Cold Spring Harbor Protocols* **2013,** pdb–top074302 (2013).
6. Padgett, M. J. & Courtial, J. Poincaré-sphere equivalent for light beams containing orbital angular momentum. *Optics letters* **24,** 430–432 (1999).
7. Konrad, T. & Forbes, A. Quantum mechanics and classical light. *Contemporary Physics* **60,** 1–22 (2019).
8. Sroor, H., Moodley, C., Rodríguez-Fajardo, V., Zhan, Q. & Forbes, A. Modal description of paraxial structured light propagation: tutorial. *J. Opt. Soc. Am. A* **38,** 1443–1449 (2021).
9. Pinnell, J. *et al.* Modal analysis of structured light with spatial light modulators: a practical tutorial. *JOSA A* **37,** C146–C160 (2020).
10. Carter, W. H. Spot size and divergence for Hermite Gaussian beams of any order. *Applied optics* **19,** 1027 (1980).
11. Phillips, R. L. & Andrews, L. C. Spot size and divergence for Laguerre Gaussian beams of any order. *Applied optics* **22,** 643 (1983).
12. Da Silva, B. P., Pinillos, V., Tasca, D., Oxman, L. & Khoury, A. Pattern Revivals from Fractional Gouy Phases in Structured Light. *Physical Review Letters* **124,** 033902 (2020).
13. Beijersbergen, M., Allen, L., van der Veen, H. & Woerdman, J. Astigmatic laser mode converters and transfer of orbital angular momentum. *Optics Communications* **96,** 123–132 (1993).
14. O'Neil, A. T. & Courtial, J. Mode transformations in terms of the constituent Hermite–Gaussian or Laguerre–Gaussian modes and the variable-phase mode converter. *Optics Communications* **181,** 35–45 (July 2000).
15. Rosales-Guzmán, C., Ndagano, B. & Forbes, A. A Review of Complex Vector Light Fields and Their Applications. *J. Opt.* **20,** 123001 (2018).

16. Forbes, A. & Nape, I. Quantum mechanics with patterns of light: Progress in high dimensional and multidimensional entanglement with structured light. *AVS Quantum Science* **1,** 011701 (2019).
17. Mazilu, M., Baumgartl, J., Kosmeier, S. & Dholakia, K. Optical Eigenmodes; exploiting the quadratic nature of the energy flux and of scattering interactions. *Optics Express* **19,** 933–945 (2011).
18. De Luca, A. C., Kosmeier, S., Dholakia, K. & Mazilu, M. Optical eigenmode imaging. *Physical Review A* **84,** 021803 (2 2011).
19. Mazilu, M. Optical eigenmodes spin and angular momentum. *Journal of Optics* **13,** 064009 (2011).
20. Piché, K. *et al.* Experimental realization of optical eigenmode superresolution. *Optics express* **20,** 26424–26433 (2012).
21. Kaliteevski, M. A., Abram, R. A. & Nikolaev, V. V. Optical eigenmodes of a cylindrical microcavity. *Journal of Modern Optics* **47,** 677–684 (2000).
22. Kosmeier, S. *et al.* Nonredundant Raman imaging using optical eigenmodes. *Optica* **1,** 257–263 (2014).
23. Allen, L., Beijersbergen, M. W., Spreeuw, R. J. C. & Woerdman, J. P. Orbital angular momentum of light and the transformation of Laguerre-Gaussian laser modes. *Physical Review A* **45,** 8185–8189 (1992).
24. Vaity, P., Banerji, J. & Singh, R. Measuring the topological charge of an optical vortex by using a tilted convex lens. *Physics Letters A* **377,** 1154–1156 (2013).
25. Abramochkin, E. & Volostnikov, V. Beam transformations and nontransformed beams. *Optics Communications* **83,** 123–135 (1991).
26. Collins, S. A. Lens-system diffraction integral written in terms of matrix optics. *JOSA* **60,** 1168–1177 (1970).
27. Shakir, S. A., Fried, D. L., Pease, E. A., Brennan, T. J. & Dolash, T. M. Efficient matrix approach to optical wave propagation and Linear Canonical Transforms. *Optics express* **23,** 26853–26862 (2015).
28. Wada, A., Ohtani, T., Miyamoto, Y. & Takeda, M. Propagation analysis of the Laguerre–Gaussian beam with astigmatism. *JOSA A* **22,** 2746–2755 (2005).
29. Kotlyar, V. V. *et al.* Elliptic Laguerre-Gaussian beams. *Journal of the Optical Society of America A* **23,** 43 (2006).
30. Kotlyar, V. V., Kovalev, A. A. & Porfirev, A. P. Vortex astigmatic Fourier-invariant Gaussian beams. *Optics Express* **27,** 657 (2019).
31. Dennis, M. R. Rows of optical vortices from elliptically perturbing a high-order beam. *Optics Letters* **31,** 1325 (May 2006).
32. Liu, P., Cao, Y., Lu, Z. & Lin, G. Probing arbitrary Laguerre–Gaussian beams and pairs through a tilted biconvex lens. *Journal of Optics* **23,** 025002 (2021).

33. Kotlyar, V. V., Kovalev, A. A. & Porfirev, A. P. Astigmatic transforms of an optical vortex for measurement of its topological charge. *Applied Optics* **56,** 4095 (2017).
34. Kotlyar, V. V., Kovalev, A. A., Porfirev, A. P. & Kozlova, E. S. Three different types of astigmatic Hermite-Gaussian beams with orbital angular momentum. *Journal of Optics* **21,** 115601 (2019).
35. Abramochkin, E., Razueva, E. & Volostnikov, V. General astigmatic transform of Hermite–Laguerre–Gaussian beams. *Journal of the Optical Society of America A* **27,** 2506 (2010).
36. Galvez, E. J. *et al.* Geometric Phase Associated with Mode Transformations of Optical Beams Bearing Orbital Angular Momentum. *Physical Review Letters* **90,** 203901 (2003).
37. Galvez, E. J. & O'Connell, M. A. *Existence and absence of geometric phases due to mode transformations of high-order modes* in (ed Andrews, D. L.) (SPIE, 2005).
38. Syouji, A., Kurihara, K., Otomo, A. & Saito, S. Diffraction-grating-type phase converters for conversion of Hermite-Laguerre-Gaussian mode into Gaussian mode. *Applied Optics* **49,** 1513 (2010).
39. Da Silva, B. P., Marques, B. A. D., Rodrigues, R. B., Ribeiro, P. H. S. & Khoury, A. Z. Machine-learning recognition of light orbital-angular-momentum superpositions. *Physical Review A* **103,** 063704 (2021).
40. Buono, W. T., Peters, C., Tau, J., Nape, I. & Forbes, A. Eigenmodes of aberrated systems: the tilted lens. *Journal of Optics* **24,** 125602 (2022).
41. Epp, S. S. *Discrete mathematics with applications* (Cengage learning, 2010).
42. Koshy, T. *Elementary number theory with applications* (Academic press, 2002).
43. Ren, Y.-X., Lu, R.-D. & Gong, L. Tailoring light with a digital micromirror device. *Annalen der physik* **527,** 447–470 (2015).
44. Scholes, S., Kara, R., Pinnell, J., Rodríguez-Fajardo, V. & Forbes, A. Structured light with digital micromirror devices: a guide to best practice. *Optical Engineering* **59,** 041202 (2019).
45. Singh, K., Buono, W. T., Forbes, A. & Dudley, A. Accelerating polarization structures in vectorial fields. *Opt. Express* **29,** 2727–2737 (2021).
46. Abramochkin, E. G. & Volostnikov, V. G. Generalized Gaussian beams. *Journal of Optics A: Pure and Applied Optics* **6,** S157–S161 (2004).
47. Zhong, R.-Y. *et al.* Gouy-phase-mediated propagation variations and revivals of transverse structure in vectorially structured light. *Physical Review A* **103,** 053520 (2021).
48. Reynolds, O. XXIX. An experimental investigation of the circumstances which determine whether the motion of water shall be direct or sinuous, and of the law of resistance in parallel channels. *Philosophical Transactions of the Royal Society of London* **174,** 935–982 (1883).

49. Kolmogorov, A. The Local Structure of Turbulence in Incompressible Viscous Fluid for Very Large Reynolds Numbers. *Proceedings: Mathematical and Physical Sciences, Turbulence and Stochastic Process: Kolmogorov's Ideas 50 Years On* **434,** 9–13 (1991).
50. Owens, J. C. Optical refractive index of air: dependence on pressure, temperature and composition. *Applied optics* **6,** 51–59 (1967).
51. Andrews, D. L. *Laser Beam Propagation through Random Media* Second (SPIE Press, 2005).
52. Trichili, A., Park, K.-H., Zghal, M., Ooi, B. S. & Alouini, M.-S. Communicating Using Spatial Mode Multiplexing: Potentials, Challenges, and Perspectives. *IEEE Communications Surveys & Tutorials* **21,** 3175–3203 (2019).
53. Trichili, A., Cox, M. A., Ooi, B. S. & Alouini, M.-S. Roadmap to free space optics. *JOSA B* **37,** A184–A201 (2020).
54. Richardson, D. J. Filling the light pipe. *Science* **30,** 327–328 (2010).
55. Richardson, D., Fini, J. & Nelson, L. Space-division multiplexing in optical fibres. *Nature Photonics* **7,** 354 (2013).
56. Lavery, M. P. *et al.* Tackling Africa's digital divide. *Nature Photonics* **12,** 249–252 (2018).
57. Li, G., Bai, N., Zhao, N. & Xia, C. Space-division multiplexing: the next frontier in optical communication. *Advances in Optics and Photonics* **6,** 413–487 (2014).
58. Berdagué, S. & Facq, P. Mode division multiplexing in optical fibers. *Appl. Opt.* **21,** 1950–1955 (1982).
59. Forbes, A., de Oliveira, M. & Dennis, M. R. Structured light. *Nature Photonics* **15,** 253–262 (2021).
60. Forbes, A. Structured Light: Tailored for Purpose. *Optics and Photonics News* **31,** 24–31 (2020).
61. Shen, Y. Rays, waves, SU (2) symmetry and geometry: toolkits for structured light. *Journal of Optics* **23,** 124004 (2021).
62. Padgett, M. J. Orbital angular momentum 25 years on. *Optics Express* **25,** 11265–11274 (2017).
63. Gibson, G. & Courtial J. and. Padgett, M. J. Free-space information transfer using light beams carrying orbital angular momentum. *Optics Express* **12,** 5448–5456 (2004).
64. Wang, J. *et al.* Terabit free-space data transmission employing orbital angular momentum multiplexing. *Nature photonics* **6,** 488–496 (2012).
65. Willner, A. E. *et al.* Optical communications using orbital angular momentum beams. *Advances in Optics and Photonics* **7,** 66–106 (2015).
66. Willner, A. E., Pang, K., Song, H., Zou, K. & Zhou, H. Orbital angular momentum of light for communications. *Applied Physics Reviews* **8,** 041312 (2021).

67. Zhan, Q. Cylindrical vector beams: from mathematical concepts to applications. *Advances in Optics and Photonics* **1,** 1–57 (2009).
68. Otte, E., Alpmann, C. & Denz, C. Polarization Singularity Explosions in Tailored Light Fields. *Laser & Photonics Reviews* **12,** 1700200 (2018).
69. Milione, G. *et al.* Gbit/s mode division multiplexing over free space using vector modes and a q-plate mode (de)multiplexer. *Optics Letters* **40,** 1980–1983 (2015).
70. Sit, A. *et al.* High-dimensional intracity quantum cryptography with structured photons. *Optica* **4,** 1006 (2017).
71. Nape, I. *et al.* Revealing the invariance of vectorial structured light in complex media. *Nature Photonics* **16,** 538–546 (2022).
72. Singh, K., Nape, I., Buono, W. T., Dudley, A. & Forbes, A. A robust basis for multi-bit optical communication with vectorial light. *arXiv preprint arXiv:2209.15559* (2022).
73. Anguita, J. A., Neifeld, M. A. & Vasic, B. V. Turbulence-induced channel crosstalk in an orbital angular momentum-multiplexed free-space optical link. *Appl. Opt.* **47,** 2414–2429 (2008).
74. Ren, Y. *et al.* Experimental characterization of a 400 Gbit/s orbital angular momentum multiplexed free-space optical link over 120 m. *Optics Letters* **41,** 622–625 (2016).
75. Krenn, M. *et al.* Communication with spatially modulated light through turbulent air across Vienna. *New Journal of Physics* **16,** 113028 (2014).
76. Zhao, Y. *et al. Experimental demonstration of 260-meter security free-space optical data transmission using 16-QAM carrying orbital angular momentum (OAM) beams multiplexing* in *Optical Fiber Communication Conference* (2016), Th1H–3.
77. Rodenburg, B. *et al.* Influence of atmospheric turbulence on states of light carrying orbital angular momentum. *Optics Letters* **37,** 3735 (2012).
78. Krenn, M. *et al.* Twisted light transmission over 143 km. *Proceedings of the National Academy of Sciences* **113,** 13648–13653 (2016).
79. Zhang, L., Shen, F., Lan, B. & Tang, A. Mode-dependent crosstalk and detection probability of orbital angular momentum of optical vortex beam through atmospheric turbulence. *Journal of Optics* **22,** 075607 (2020).
80. Malik, M. *et al.* Influence of atmospheric turbulence on optical communications using orbital angular momentum for encoding. *Optics express* **20,** 13195–13200 (2012).
81. Chen, C., Yang, H., Tong, S. & Lou, Y. Changes in orbital-angular-momentum modes of a propagated vortex Gaussian beam through weak-to-strong atmospheric turbulence. *Optics express* **24,** 6959–6975 (2016).
82. Tyler, G. A. & Boyd, R. W. Influence of atmospheric turbulence on the propagation of quantum states of light carrying orbital angular momentum. *Optics letters* **34,** 142–144 (2009).

83. Paterson, C. Atmospheric turbulence and orbital angular momentum of single photons for optical communication. *Phys. Rev. Lett.* **94,** 153901 (2005).

84. Jha, A. K., Tyler, G. A. & Boyd, R. W. Effects of atmospheric turbulence on the entanglement of spatial two-qubit states. *Phys. Rev. A* **81,** 053832 (2010).

85. Tyler, G. A. & Boyd, R. W. Influence of atmospheric turbulence on the propagation of quantum states of light carrying orbital angular momentum. *Optics Letters* **34,** 142–144 (2009).

86. Hamadou Ibrahim, A., Roux, F. S., McLaren, M., Konrad, T. & Forbes, A. Orbital-angular-momentum entanglement in turbulence. *Phys. Rev. A* **88,** 012312 (2013).

87. Gopaul, C. & Andrews, R. The effect of atmospheric turbulence on entangled orbital angular momentum states. *New Journal of Physics* **9,** 94 (2007).

88. Zhang, Y., Prabhakar, S., Roux, F. S., Forbes, A., Konrad, T., *et al.* Experimentally observed decay of high-dimensional entanglement through turbulence. *Physical Review A* **94,** 032310 (2016).

89. Pors, B.-J., Monken, C., Eliel, E. R. & Woerdman, J. Transport of orbital-angular-momentum entanglement through a turbulent atmosphere. *Optics express* **19,** 6671–6683 (2011).

90. Goyal, S. K., Roux, F. S., Konrad, T., Forbes, A., *et al.* The effect of turbulence on entanglement-based free-space quantum key distribution with photonic orbital angular momentum. *Journal of Optics* **18,** 064002 (2016).

91. Leonhard, N. D., Shatokhin, V. N. & Buchleitner, A. Universal entanglement decay of photonic-orbital-angular-momentum qubit states in atmospheric turbulence. *Physical Review A* **91,** 012345 (2015).

92. Sorelli, G., Leonhard, N., Shatokhin, V. N., Reinlein, C. & Buchleitner, A. Entanglement protection of high-dimensional states by adaptive optics. *New Journal of Physics* **21,** 023003 (2019).

93. Mphuthi, N., Botha, R. & Forbes, A. Are Bessel beams resilient to aberrations and turbulence? *JOSA A* **35,** 1021–1027 (2018).

94. Mphuthi, N. *et al.* Free-space optical communication link with shape-invariant orbital angular momentum Bessel beams. *Applied Optics* **58,** 4258–4264 (2019).

95. Lukin, I. P. Mean intensity of vortex Bessel beams propagating in turbulent atmosphere. *Applied optics* **53,** 3287–3293 (2014).

96. Bao-Suan, C. & Ji-Xiong, P. Propagation of Gauss–Bessel beams in turbulent atmosphere. *Chinese Physics B* **18,** 1033 (2009).

97. Zhu, K., Zhou, G., Li, X., Zheng, X. & Tang, H. Propagation of Bessel-Gaussian beams with optical vortices in turbulent atmosphere. *Optics Express* **16,** 21315–21320 (2008).

98. Nelson, W., Palastro, J., Davis, C. & Sprangle, P. Propagation of Bessel and Airy beams through atmospheric turbulence. *JOSA A* **31,** 603–609 (2014).

99. Ahmed, N. *et al.* Mode-division-multiplexing of multiple Bessel-Gaussian beams carrying orbital-angular-momentum for obstruction-tolerant free-space optical and millimetre-wave communication links. *Scientific reports* **6,** 22082 (2016).

100. Cheng, M., Guo, L., Li, J. & Zhang, Y. Channel capacity of the OAM-based free-space optical communication links with Bessel–Gauss beams in turbulent ocean. *IEEE Photonics Journal* **8,** 1–11 (2016).

101. Doster, T. & Watnik, A. T. Laguerre–Gauss and Bessel–Gauss beams propagation through turbulence: analysis of channel efficiency. *Applied Optics* **55,** 10239–10246 (2016).

102. Watkins, R. J. *et al.* Experimental probing of turbulence using a continuous spectrum of asymmetric OAM beams. *Optics express* **28,** 924–935 (2020).

103. Vetter, C. *et al.* Realization of Free-Space Long-Distance Self-Healing Bessel Beams. *Laser & Photonics Reviews* **13,** 1900103 (2019).

104. Yuan, Y. *et al.* Beam wander relieved orbital angular momentum communication in turbulent atmosphere using Bessel beams. *Scientific reports* **7,** 1–7 (2017).

105. Cox, M. A. *et al.* The Resilience of Hermite- and Laguerre-Gaussian Modes in Turbulence. *Journal of Lightwave Technology* **37,** 3911–3917. ISSN: 0733-8724 (2019).

106. Ndagano, B., Mphuthi, N., Milione, G. & Forbes, A. Comparing mode-crosstalk and mode-dependent loss of laterally displaced orbital angular momentum and Hermite–Gaussian modes for free-space optical communication. *Optics Letters* **42,** 4175. ISSN: 0146-9592 (2017).

107. Restuccia, S., Giovannini, D., Gibson, G. & Padgett, M. Comparing the information capacity of Laguerre–Gaussian and Hermite–Gaussian modal sets in a finite-aperture system. *Optics Express* **24,** 27127. ISSN: 1094-4087 (2016).

108. Ndagano, B., Mphuthi, N., Milione, G. & Forbes, A. Comparing mode-crosstalk and mode-dependent loss of laterally displaced orbital angular momentum and Hermite–Gaussian modes for free-space optical communication. *Optics letters* **42,** 4175–4178 (2017).

109. Trichili, A. *et al.* Optical communication beyond orbital angular momentum. *Scientific Reports* **6,** 27674 (2016).

110. Zhao, N., Li, X., Li, G. & Kahn, J. M. Capacity limits of spatially multiplexed free-space communication. *Nature photonics* **9,** 822 (2015).

111. Zhou, Y. *et al.* Using all transverse degrees of freedom in quantum communications based on a generic mode sorter. *Optics express* **27,** 10383–10394 (2019).

112. Xie, G. *et al.* Experimental demonstration of a 200-Gbit/s free-space optical link by multiplexing Laguerre–Gaussian beams with different radial indices. *Optics letters* **41,** 3447–3450 (2016).

113. Li, L. *et al.* Power loss mitigation of orbital-angular-momentum-multiplexed free-space optical links using nonzero radial index Laguerre–Gaussian beams. *JOSA B* **34,** 1–6 (2017).

114. Gu, X., Chen, L. & Krenn, M. Phenomenology of complex structured light in turbulent air. *ArXiv,* 1906.03581v1 (2019).

115. Klug, A., Nape, I. & Forbes, A. The orbital angular momentum of a turbulent atmosphere and its impact on propagating structured light fields. *New Journal of Physics* **23,** 093012 (2021).

116. Miller, D. A. Better choices than optical angular momentum multiplexing for communications. *Proc. Natl. Acad. Sci. U.S.A.* **114,** E9755–E9756 (2017).

117. Cox, M. A. *et al.* Structured light in turbulence. *IEEE Journal of Selected Topics in Quantum Electronics* **27,** 1–21 (2020).

118. Gu, Y., Korotkova, O. & Gbur, G. Scintillation of nonuniformly polarized beams in atmospheric turbulence. *Optics letters* **34,** 2261–2263 (2009).

119. Cheng, W., Haus, J. W. & Zhan, Q. Propagation of vector vortex beams through a turbulent atmosphere. *Optics express* **17,** 17829–17836 (2009).

120. Cai, Y., Lin, Q., Eyyuboğlu, H. T. & Baykal, Y. Average irradiance and polarization properties of a radially or azimuthally polarized beam in a turbulent atmosphere. *Optics express* **16,** 7665–7673 (2008).

121. Ji-Xiong, P., Tao, W., Hui-Chuan, L. & Cheng-Liang, L. Propagation of cylindrical vector beams in a turbulent atmosphere. *Chinese Physics B* **19,** 089201 (2010).

122. Wang, T. & Pu, J. Propagation of non-uniformly polarized beams in a turbulent atmosphere. *Optics communications* **281,** 3617–3622 (2008).

123. Cox, M. A., Rosales-Guzmán, C., Lavery, M. P. J., Versfeld, D. J. & Forbes, A. On the resilience of scalar and vector vortex modes in turbulence. *Optics Express* **24,** 18105–18113 (2016).

124. Lochab, P., Senthilkumaran, P. & Khare, K. Designer vector beams maintaining a robust intensity profile on propagation through turbulence. *Physical Review A* **98,** 023831 (2018).

125. Ndagano, B. *et al.* Characterizing quantum channels with non-separable states of classical light. *Nature Physics* **13,** 397–402 (2017).

126. Zhu, Z. *et al.* Compensation-Free High-Capacity Free-Space Optical Communication Using Turbulence-Resilient Vector Beams. *arXiv preprint arXiv:1910.05406* (2019).

127. Cox, M. A., Cheng, L., Rosales-Guzmán, C. & Forbes, A. Modal diversity for robust free-space optical communications. *Physical Review Applied* **10,** 024020 (2018).

128. Tyson, R. K. Bit-error rate for free-space adaptive optics laser communications. *JOSA A* **19,** 753–758 (2002).

129. Zhao, S., Leach, J., Gong, L., Ding, J. & Zheng, B. Aberration corrections for free-space optical communications in atmosphere turbulence using orbital angular momentum states. *Optics express* **20,** 452–461 (2012).

130. Ren, Y. *et al.* Adaptive-optics-based simultaneous pre-and post-turbulence compensation of multiple orbital-angular-momentum beams in a bidirectional free-space optical link. *Optica* **1,** 376–382 (2014).

131. He, C., Wang, J., Hu, Q., Antonello, J. & Booth, M. J. *Vectorial adaptive optics: correction of polarization and phase* in *Adaptive Optics and Wavefront Control for Biological Systems VI* **11248** (2020), 1124808.

132. Li, M., Li, Y. & Han, J. Gerchberg–Saxton algorithm based phase correction in optical wireless communication. *Physical Communication* **25,** 323–327 (2017).

133. Liu, J. *et al.* Deep learning based atmospheric turbulence compensation for orbital angular momentum beam distortion and communication. *Optics express* **27,** 16671–16688 (2019).

134. Miller, D. A. Waves, modes, communications, and optics: a tutorial. *Advances in Optics and Photonics* **11,** 679–825 (2019).

135. Shatokhin, V., Bachmann, D., Sorelli, G., Treps, N. & Buchleitner, A. *Spatial eigenmodes of light in atmospheric turbulence* in *Environmental Effects on Light Propagation and Adaptive Systems III* **11532** (2020), 63–70.

136. Borcea, L., Garnier, J. & Sølna, K. Multimode communication through the turbulent atmosphere. *JOSA A* **37,** 720–730 (2020).

137. Pai, P., Bosch, J., Kühmayer, M., Rotter, S. & Mosk, A. P. Scattering invariant modes of light in complex media. *Nat. Photonics* **15,** 431–434 (2021).

138. Pai, P., Bosch, J. & Mosk, A. P. Optical transmission matrix measurement sampled on a dense hexagonal lattice. *OSA Continuum* **3,** 637–648 (2020).

139. Chuang, I. L. & Nielsen, M. A. Prescription for experimental determination of the dynamics of a quantum black box. *Journal of Modern Optics* **44,** 2455–2467 (1997).

140. Toninelli, E. *et al.* Concepts in quantum state tomography and classical implementation with intense light: a tutorial. *Advances in Optics and Photonics* **11,** 67–134 (2019).

141. Valencia, N. H., Goel, S., McCutcheon, W., Defienne, H. & Malik, M. Unscrambling entanglement through a complex medium. *Nature Physics* **16,** 1112–1116 (2020).

142. Ndagano, B. *et al.* Characterizing quantum channels with non-separable states of classical light. *Nature Physics* **13,** 397–402 (2017).

143. Ndagano, B. & Forbes, A. Characterization and mitigation of information loss in a six-state quantum-key-distribution protocol with spatial modes of light through turbulence. *Physical Review A* **98,** 062330 (2018).

144. Andrews, L. C. & Phillips, R. L. *Laser beam propagation through random media* in (2005).

145. Schmidt, J. *Numerical simulation of optical wave propagation with examples in MATLAB* in (2010).

146. Fahey, T., Islam, M., Gardi, A. & Sabatini, R. Laser Beam Atmospheric Propagation Modelling for Aerospace LIDAR Applications. *Atmosphere* **12,** 918 (2021).

147. Arrizón, V., Ruiz, U., Carrada, R. & González, L. A. Pixelated phase computer holograms for the accurate encoding of scalar complex fields. *J. Opt. Soc. Am. A* **24,** 3500 (2007).

148. Rodenburg, B. *et al.* Simulating thick atmospheric turbulence in the lab with application to orbital angular momentum communication. *New Journal of Physics* **16,** 033020 (2014).

149. Lechner, D., Zepp, A., Eichhorn, M. & Gładysz, S. Adaptable Shack-Hartmann wavefront sensor with diffractive lenslet arrays to mitigate the effects of scintillation. *Optics express* **28,** 36188–36205 (2020).

150. Barchers, J. D., Fried, D. L. & Link, D. J. Evaluation of the performance of Hartmann sensors in strong scintillation. *Applied optics* **41,** 1012–1021 (2002).

151. Bachmann, D. *et al.* Highly-transmitting modes of light in dynamic atmospheric turbulence. *arXiv preprint arXiv:2204.05675* (2022).